공 학 박 사 학 위 논 문

Effect of heat treatment on mechanical properties and edge cracking behavior of high strength 7075 aluminum alloy sheets

고강도 7075 알루미늄 합금 판재의 열처리 조건에 따른 기계적 물성 및 에지 파단 특성 연구

2021년 8월

서 울 대 학 교 대 학 원

재 료 공 학 부

최 유 미

고강도 7075 알루미늄 합금 판재의 열처리 조건에 따른 기계적 물성 및 에지 파단 특성 연구

Effect of heat treatment on mechanical properties and edge cracking behavior of high strength 7075 aluminum alloy sheets

지도 교수 이 명 규

이 논문을 공학박사학위논문으로 제출함

2021년 8월

서울대학교 대학원

재료공학부

최 유 미

최유미의 공학박사 학위논문을 인준함

2021년 8월

위 원 장 한 흥 남

부위원장 이 명 규

위 원 최 인 석

위 원 홍 승 현

위 원 이 진 우

Abstract

Effect of heat treatment on mechanical properties and edge cracking behavior of high strength 7075 aluminum alloy sheets

Yumi Choi
Department of Materials Science and Engineering
The Graduate School
Seoul National University

As the automobile industry strives to increase fuel efficiency due to environmental regulations, various techniques for forming aluminum alloy 7000 series have been investigated. In this thesis, the formability of W temper, super-saturated by solution heat treatment followed by water quenching, is examined and the results are compared with peak-aged temper (T6). Immediately after quenching, the W temper sheet shows reduced strength and larger elongation than T6 temper, and up to 80% or more of the strength of the original material is recovered during the natural aging process. Still, studies on the experimental results, plastic deformation behavior, and especially numerical analysis results of W temper are lacking.

The purpose of this thesis is to investigate the possibility of W temper forming through various experiments. Formability is evaluated using a forming limit diagram and the springback with a U-shaped draw/bending experiment, and examining the edge cracking behavior with a hole expansion experiment using conical and flat-headed punches is also conducted. The M-K model is used to predict the forming limit diagram, and non-quadratic yield function (Yield 2000), chord modulus, and anisotropic hardening (HAH)

model are used to capture springback. The thickness profiles of the flat-headed hole-expansion experiment are predicted using non-quadratic yield function and isotropic hardening.

The experiments are conducted under T6 and W temper, respectively, and the results are compared to each other. In particular, -W shows serrated flow stress in the engineering stress-strain curve, called the Portevin-Le-Chatelier (PLC) effect, and the experimental results are analyzed by considering the influence of the PLC effect on each experiment. Based on finite element analysis verified through comparison with the experimental results of T6, the same experiment and finite element analysis are conducted with -W.

By comparing the experimental results and finite element analysis results reflecting the material properties excluding the modeling of the PLC effect, the influence of the PLC effect on each experiment is investigated. Based on the comparison results, methods to reflect the characteristics of the PLC effect in finite element analysis and considerations for analyzing the results are suggested. The following PLC effect influences on each experiment are investigated:

1) Overestimation of the strain hardening coefficient in hardening curve, 2) high roughness in the surface condition, 3) short post uniform elongation caused in the ductile material, and 4) appearance of PLC bands in the hole expansion experiment showing interactions with plastic anisotropy.

In this thesis, the -W temper shows enhanced elongation, lower flow stress, larger forming limit diagram, smaller springback, and even greater stretch-flangeability than T6 temper.

Keyword : High strength aluminum, W temper forming, PLC effect, formability, springback, stretch-flangeability

Student Number : 2018-37839

Contents

List of tables

List of figures

1. Introduction

1.1 Overview

Aluminum alloys have been one of the major materials for aircraft structural components for more than 80 years, and one of the main groups of aluminum alloys is the aluminum 7xxx series, which has high strength due to precipitation hardening.[1–3]. As automotive companies have recently been under increasing pressure to enhance fuel efficiency because of environmental issues, weight reduction is one of the important issues, and aluminum alloys have received great attention as an alternative structural material to steel [4]. In a Super Light Car project, Hirsch concluded that aluminum alloys can make weight savings of up to 50% in BIW parts while maintaining safety and performance [5]. In particular, the 7000 series aluminum alloys used in aircraft structural components have drawn great attention due to their superior mechanical properties, but the aluminum T6 alloys have limited application as automotive structural materials due to their inferior formability at room temperature (RT). To improve the formability of aluminum 7000 series aluminum, elevated forming technologies such as warm forming [6–8], hot forming[9–11], multi-stage forming [12] and hot stamping process [10,11,13,14] are used. Elevated forming techniques such as warm forming, hot forming, and hot quenching forming are investigated to overcome the poor formability of 7000 series aluminum. however, pre-brushing the lubrication on the surface of the tool and the post-cleaning process for removing lubrication from the formed part affect productivity, which causes high cost [15]. Adhesion between tool and

softened aluminum has a galling effect, which occurs frequently at high temperature and reduces the surface finish quality [16].

The room temperature stamping process has been attempted in the forming of high strength aluminum alloys, wherein the sheet during stamping has a similar microstructure as the state of the supersaturated solid solution (SSSS) and the strength of the formed part can be further recovered by post-heat treatment. This process is called "W-temper (W) forming." The detailed procedure for –W forming is illustrated in Fig. 1, in the order of SHT, water quenching, cold forming, and natural and artificial aging. Microstructurally, -W temper improved the ductility and reduced the strength to less than T6 temp, as shown in Fig. 2, by dissolving the preexisting precipitates during SHT, as reported in previous papers [17,18]. In Fig. 2, the x-axis is presented as $\Delta L/L_0$, where $L_0 = 50\ mm$ is the initial length of the virtual extensometer and ΔL its extension, and correspondingly, the y-axis is described as Force/Area [N/mm^2]. Typically, these quantities are reported as engineering strain and stress, respectively. Although -W temper is a long-standing heat treatment temper that was already referred to in 1966 by the U.S. Department of Defense [19] and other papers [20], W temper is rarely investigated because of its unstable properties.

Rather than examining plastic and elastic behavior, the serrated flow curve shown in -W temper is heavily scrutinized, which is the feature of the Portevin-Le-Chatelier (PLC) effect as shown in Fig 2.

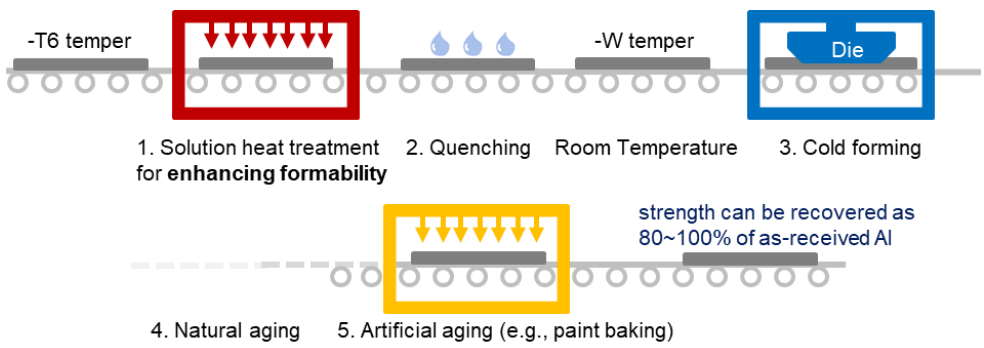

Figure 1. Schematic of W-temper forming process

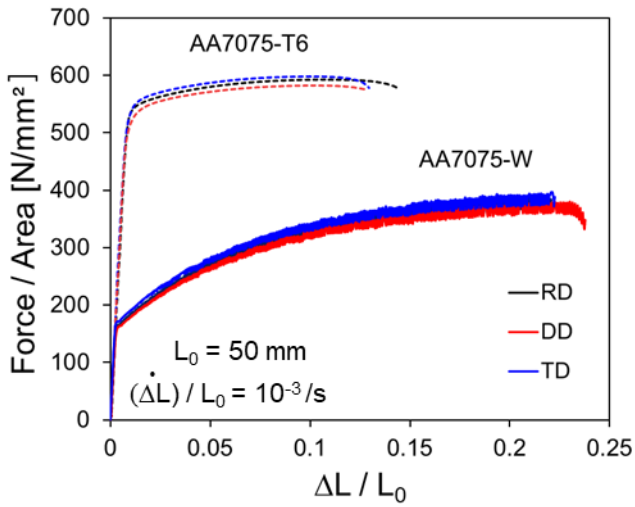

Figure 2. Force/area - $\Delta L/L_0$ curves of T6 and AA705-W

In the -W temper condition, the concentration of vacancies is increased by quenching and the diffusion rate may sufficiently increase to cause strain ageing during plastic deformation [21]. The PLC effect is published as being considerably sensitive to deformation conditions, such as stress state, specimen geometry, strain rate, temperature, etc. For example, strain rate [22–24], specimen geometry [25,26], stress state [27–29] and temperature [30,31] may result in different types of PLC bands appearing in the strain region, and transitions between band types occur and completely suppress the band shapes. Types of PLC bands are clearly defined based on the three types of serrated flow shape combined with the corresponding propagation feature of each PLC band in the stress-strain curve of a tensile experiment: type A, B, and C [22,32–34]. The W tempered aluminum 7075 used in this dissertation exhibits C type bands under 10-3/s strain rate in the uniaxial tensile experiment as shown in Fig. 3. In addition, numerous studies have been conducted to reveal the mechanism of the PLC effect, reproduce it through formulation, and verify the formulation through simulation [35–43].

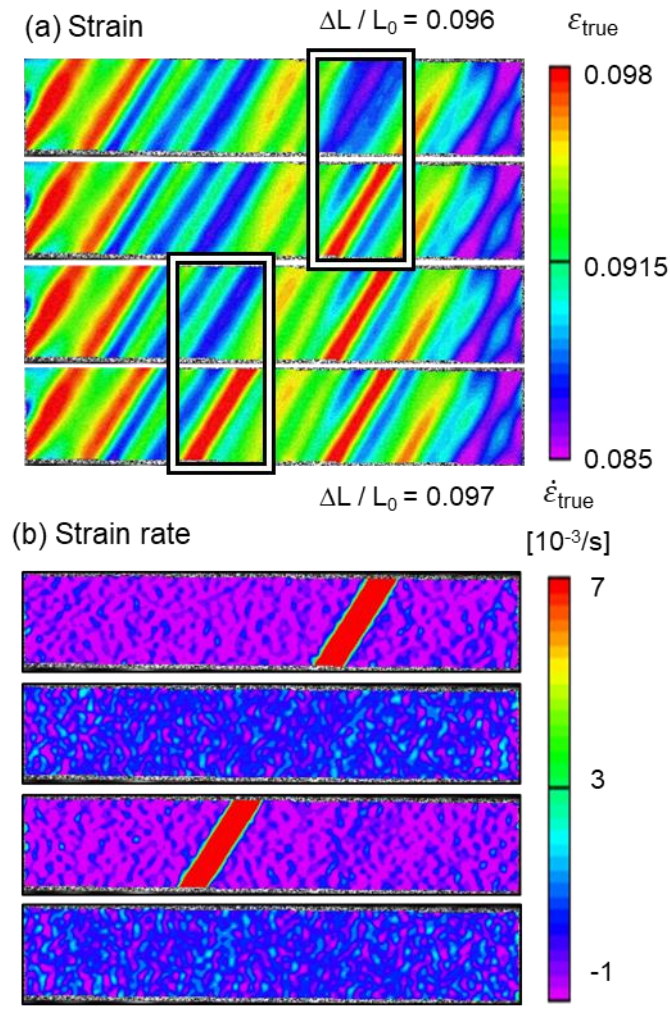

Figure 3. PLC band observed in uniaxial tension experiment of AA7075-W: (a) major principal strain distribution and (b) major strain rate distribution

However, studies on the formability of w-temper are still lacking, and in particular, since the deep drawing process of sheet material is uncommonly used in the aviation industry, investigations related to deep drawing, which is widely used in the automotive industry, are needed.

Aluminum 7075, which is used in the aviation industry, can have various advantages if w-temper forming is used in the automotive forming process. First of all, the forming process in the automobile industry is much faster than that in the aviation industry, and the sheets could sufficiently complete the forming process before precipitates are generated inside after quenching. After the part is completely formed, more than 80% of the original ultimate tensile strength could be recovered by generating Guinier-Preston (G.P.) zones at room temperature without additional treatment, which is called natural aging [7,44,45]. Furthermore, formed parts in the aviation industry are not or are rarely exposed to heat treatment, while paint baking is one of the inevitable processes in the automotive manufacturing process. The paint-baking process consists of two to five sequential steps and involves heating for about 2 hours in a temperature range of 120 to 185 ℃, with intermediate cooling between the steps. Natural aged aluminum 7075-W (similar to T4) or aluminum 7075-W achieves additional artificial aging during the paint-baking process. The downside of paint baking is the possibility of slightly reducing the ultimate tensile strength. However, the advantages are dramatically increased yield strength [46] and phase transformation from an unstable distributed G.P. zone or super-saturated solid solution to metastable eta prime or stable eta based on the aging process [14,18,47].

1.2 Theoretical background

1.2.1 Aluminum 7075

The main strengthening mechanism of aluminum 7075 is precipitation hardening. Therefore, the precipitation processes in the Al-Zn-Mg alloy system have been studied through many studies. The generally accepted aging sequence of aluminum 7075 is:

Super-saturated solid solution (SSSS) → Guinier Preston (G.P.) zones → metastable phase η' ($MgZn_2$) → equilibrium phase η ($MgZn_2$).

The shape of η and η' phases are both platelet or rod shapes [48]; however, there is a difference in coherency with the matrix. The equilibrium η phase with a hexagonal structure is incoherent with the main Al matrix, while the metastable η' phase, the main reason for the high strength, is semi-coherent with the matrix [49,50]. The G.P. zones, which is one of the main causes of precipitation for the strength of aluminum 7075-T4 temper, also form coherence with the matrix with a spherical shape [48]. Since all these precipitations have a nanoscale size, transmission electron microscopy is commonly used to capture the size of precipitation. The G.P. zones can be classified G.P. zone (I) and G.P. zone (II) by high-resolution transmission electron microscopy (HRTEM) study [14]. G.P. zone (I) was thought to be formed from solute-rich material and could be formed at room temperature, while G.P. zone (II) was believed to be formed by vacancy-rich clusters or vacancy-related clusters [49].

After solution heat treatment followed by water quenching, the matrix has a super-saturated solid solution state and has vacancy-rich clusters induced by quick quenching

[51]. During the natural aging process, G.P. zones, especially G.P. zone (I), can be generated at room temperature [52], and the volume fraction and radius of the G.P. zones similarly increase with the increase in yield stress [53]. The G.P. zones are believed to be the precursor of the metastable η' phase and equilibrium η phase at elevated temperature, which could be causing the strengthening of the material. From the G.P. zones and matrix, the metastable η ' formation is caused at the early stage of artificial aging at peak-aged temperature. The dominant mechanism of η ' formation around 120 degree is the transformation of a small G.P. zone (I) [54] and the distribution of fine η ' phase is linked to the high strength [55]. On the other hand, the η phases cause hardening in the over-aging condition and enhance corrosion resistance properties [54,56]. Since the major precipitations of aluminum 7075 are temporarily dissolved in the W temper by solid solution heat treatment, the major difference in the strength level between T6 and -W temper is also related to the microstructure.

1.2.2 PLC effect

The unstable plastic flow of material may display an irregular plastic flow with serration under certain deformation conditions, which is also referred to as repetitive yielding. It is commonly called the Portevin-Le Chatelier (PLC) effect, and sometimes called Savart-Masson. In the experiments of Savart (1837) and Masson (1841), serrated flow curves were first observed in various specimens, showing a "staircase" phenomenon. Later, Le Chatelier (1909) reported plastic oscillations in tests using mild steel at elevated temperatures, and Portevin and Le Chatelier revealed the serrated flow curve phenomenon of aluminum alloys (Duralumins) at ambient temperature [60]. The PLC effect is observed in both substitutional and interstitial alloys such as austenitic steel, mild steel, low carbon steel, copper, and aluminum [34]. At room temperature, the diffusivity of solute atoms in an aluminum sheet is commonly too low to cause noticeable strain ageing. However, the higher concentration of vacancies and super-saturated solid solution formation induced by applied SHT in the W temper condition allow the rate of diffusion to increase sufficiently to trigger an appreciable strain ageing effect [21].

There are two obvious features of the PLC effect: the localization of strain in the specimen and the shift of localized strain along the specimen as stress increases.

The types of PLC bands are phenomenologically classified based on the shape observed in the stress-strain curve. Novel investigation techniques such as laser extensometer and digital image correlation (DIC) have been applied to grasp the spatiotemporal characteristics of the PLC effect. Based on detailed investigations to understand the serration patterns with various measurement techniques, the spatiotemporal behaviors of deformation bands on the macro scale are classified as type A, B, and C as

shown Fig. 4.

The type A PLC band displays a relatively small stress drop quasi-periodically interposed in the regular plastic flow curve. Type A is observed at relatively high strain rates or low temperatures accompanying continuous propagation of the band along the tensile axis. Type B propagates within the band by discontinuously hopping in an intermittent way, showing uninterrupted oscillation. Type B has a smaller amplitude than type C and higher frequencies than type A. Also, the type B bands are shown at an intermediate strain rate level and temperature range between type A and type C. The flow curve of type C is represented as sharp stress drops repeatedly showing relatively larger amplitude with steady frequency without specific spatiotemporal correlation, which means random nucleation and disappearing rather than continuously propagating throughout the specimen gauge section. Usually, the type C band appears at lower strain rates and higher temperatures. The behaviors of the PLC effect are commonly classified into these three types based on the serration patterns in flow curves; however, five types are suggested to distinguish the specific behaviors in detail [25,61]. Types D and E of PLC bands shown in stress-strain curves are less referred to as having generic behavior than the other types. The feature of type D in stress-stress curves shows as step-like behavior with less visible work hardening. The type E serrations appear at a large strain range of the stress-strain curve showing type A and display irregular fluctuations without work hardening. The types of PLC bands are transitional based on the deformation condition, as written in the previous section. Usually, a specific band appears at a certain strain rate and temperature range, but two bands could appear simultaneously at the critical temperatures and strain rates, which are called crossover regimes [62–64].

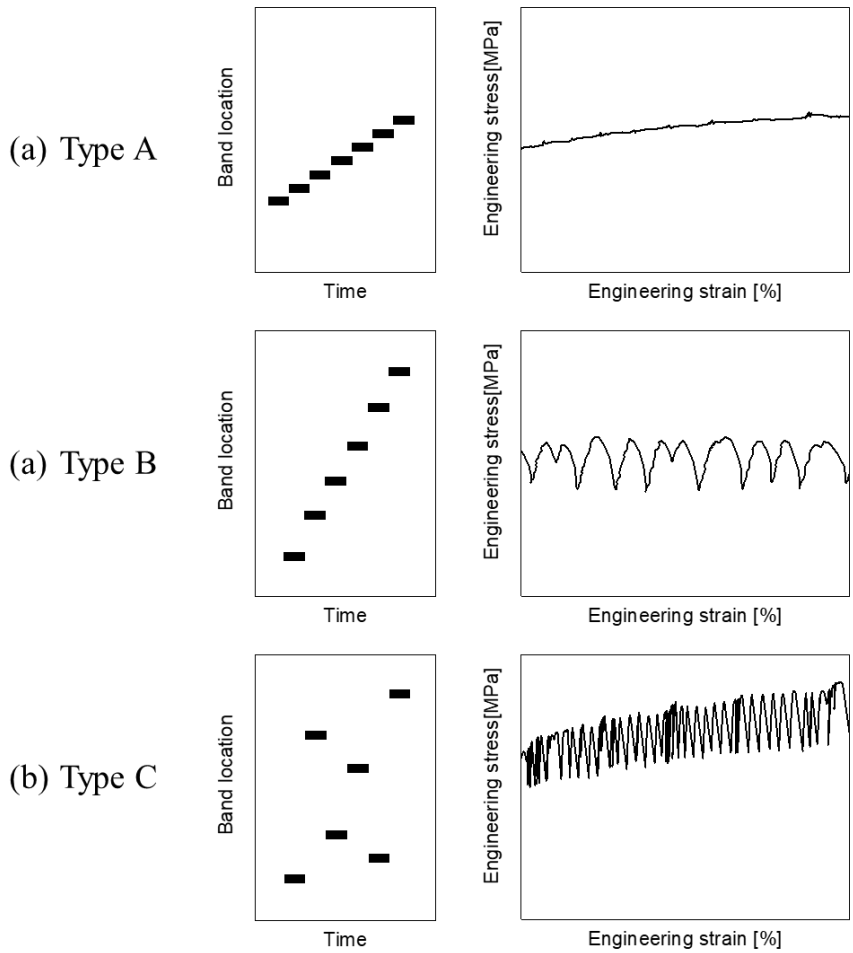

Figure 4. Schematics of spatio-temporal appearance and stress-strain curves of the PLC bands: (a) type A, (b) type B, and (c) type C

The most conventionally accepted explanation for the origin of the PLC effect is based on the dynamic strain aging (DSA) model, which is defined as an interaction of mobile dislocation with diffusing solute atoms in a pinning and breaking process [35,65,66]. The mobile dislocations carrying the plastic deformation move discontinuously in the matrix because of being temporarily arrested at several local obstacles such as solute atoms. The mobile dislocations suffer additional pinning by solute atoms diffusing towards the dislocations during waiting time, which means spent time by being arrested at the localized obstacles [67]. The ageing hardening induced by mobile solute atoms and the unpinning of glide dislocations from the arrested solute clouds dynamically and repetitively compete with each other, which is manifested as a repeated plastic serration flow curve. Since the kinetics of the PLC effect are from this competition between the diffusion of mobile solutes and unpinning of dislocation, this PLC effect is mainly sensitive to strain rate and temperature. When the glide dislocations are arrested at localized obstacles, the solute atoms are diffused toward the dislocations, which allows the glide dislocations to be subjected to additional pinning. As waiting times increase, the additional strength from diffused obstacles is also increased. Because the larger dislocation gliding velocity corresponding to the higher global strain rate allows mobile dislocations to have shorter waiting time on obstacles, negative strain rate sensitivity may appear. Recently, forest dislocations have also been considered as local obstacles to take the local strain change within bands into account [68,69], and pipe diffusion is also commonly accepted to compensate the low diffusivity of solute atoms at room temperature [70–72].

However, the precise interpretation of the PLC effect still needs further scrutiny. The interactions between dislocations from long-range stress fields are also observed (48,49) and recently the long-range interactions of dislocations have drawn attention as an

important reason for serrated plastic flow, with some papers saying that the DSA of noninteracting dislocations is independent on the rise in negative strain rate sensitivity [73,74]. Furthermore, an experimental study explained some features of the PLC effect by considering only the collective behaviors of dislocation without any solute diffusion, and supported the low correlation of solute contribution to the PLC effect. Mulford and Kocks reported that critical strain in a serrated flow and the vacancy population are independent [75]. However, Almeida [76] showed the contribution of vacancy concentration and thermally induced diffusion on the DSA. There are still difficulties with the precise theoretical explanations for the microscopic characteristics of the PLC effect to clarify all phenomena; however, the dislocation arrest model, where the diffusion of solute atoms through dislocations is arrested at forest intersections, is widely accepted.

The PLC effect needs to be distinguished from similar plastic strain localization phenomena called Lüders band[77], which represents the tensile stress of local strain softening when material starts deformation by changing from an elastic regime to a plastic regime. Even though the interactions between solute atoms and dislocation are also linked with the Lüders band, this band is material behavior caused by a multiplication of dislocations. In the first yield condition, the Lüders band is represented as drop in yield stress followed by the stress induced by the propagation of deformation bands. Lüders bands are is not repetitive phenomena since the change in material is irreversible. Generally, the unexpected stretching by Lüders bands are prevented by pre-deformation. Meanwhile, the PLC effect is a repetitive strain localization phenomenon and it occurs in various deformation conditions. The transition between Lüders band to PLC effect may occur, or even both phenomena may occur simultaneously during first yielding [78].

1.2.3 Plastic anisotropy yield model

The plastic anisotropy of material is mainly caused by crystallographic textures developed from the rolling processes. The macroscopic phenomenological anisotroipc yield model are used for characterizing the plastic anisotropy in forming analysis. For the aluminum, Anisotropic yield model using linear transformations of the stress tensor have been frequently used to analysis the sheet forming. A summary of the model is provided below, and the full derivation of the model appears in Ref. [79]. The yield function is expressed as follows:

$$\phi(\boldsymbol{\sigma}) = \left(\frac{\phi' + \phi''}{2} \right)^{1/\mathrm{m}} = \bar{\sigma} \qquad (1)$$

with

$$\phi' = \left| \mathrm{S}_1^{(1)} - \mathrm{S}_2^{(1)} \right|^{\mathrm{m}} \quad \text{and} \quad \phi'' = \left| 2\mathrm{S}_2^{(2)} + \mathrm{S}_1^{(2)} \right|^{\mathrm{m}} + \left| 2\mathrm{S}_1^{(2)} + \mathrm{S}_2^{(2)} \right|^{\mathrm{m}}, \qquad (2)$$

where $\mathrm{S}_{1,2}^{(i)}$ ($i = 1, 2$) are the principal stresses of the second-order tensor $\mathbf{S}^{(i)}$ ($i = 1, 2$) under the plane stress condition. These stresses are linearly transformed from Cauchy stress $\boldsymbol{\sigma}$.

$$\mathbf{S}^{(i)} = \mathbf{C}^{(i)} \cdot \mathbf{s} = \mathbf{C}^{(i)} \cdot \mathbf{T} \cdot \boldsymbol{\sigma} = \mathbf{L}^{(i)} \cdot \boldsymbol{\sigma} \quad \text{with } i = 1, 2; \qquad (3)$$

where $\mathbf{T}$ is a transformation tensor relating $\boldsymbol{\sigma}$ to deviatoric stress tensor $\mathbf{s}$. Also, the two other transformation tensors, $\mathbf{L}^{(1)}$ and $\mathbf{L}^{(2)}$ (or $\mathbf{C}^{(1)}$ and $\mathbf{C}^{(2)}$), are introduced to complete Yld2000-2d. The matrix forms of the two linear transformations are expressed as

follows:

$$\begin{bmatrix} S_{xx}^{(i)} \\ S_{yy}^{(i)} \\ S_{xy}^{(i)} \end{bmatrix} = \begin{bmatrix} L_{11}^{(i)} & L_{12}^{(i)} & 0 \\ L_{21}^{(i)} & L_{22}^{(i)} & 0 \\ 0 & 0 & L_{66}^{(i)} \end{bmatrix} \begin{bmatrix} \sigma_{xx} \\ \sigma_{yy} \\ \sigma_{xy} \end{bmatrix} \quad \text{with } i = 1 \text{ and } 2, \tag{4}$$

$$\begin{bmatrix} L_{11}^{(1)} \\ L_{12}^{(1)} \\ L_{21}^{(1)} \\ L_{22}^{(1)} \\ L_{66}^{(1)} \end{bmatrix} = \begin{bmatrix} 2/3 & 0 & 0 \\ -1/3 & 0 & 0 \\ 0 & -1/3 & 0 \\ 0 & 2/3 & 0 \\ 0 & 0 & 1 \end{bmatrix} \begin{bmatrix} a_1 \\ a_2 \\ a_7 \end{bmatrix}, \begin{bmatrix} L_{11}^{(2)} \\ L_{12}^{(2)} \\ L_{21}^{(2)} \\ L_{22}^{(2)} \\ L_{66}^{(2)} \end{bmatrix} = \frac{1}{9} \begin{bmatrix} -2 & 2 & 8 & -2 & 0 \\ 1 & -4 & -4 & 4 & 0 \\ 4 & -4 & -4 & 1 & 0 \\ -2 & 8 & 2 & -2 & 0 \\ 0 & 0 & 0 & 0 & 9 \end{bmatrix} \begin{bmatrix} a_3 \\ a_4 \\ a_5 \\ a_6 \\ a_8 \end{bmatrix} \tag{5}$$

The material constants (a_1–a_8) in Eq. (5) can be obtained from the uniaxial tension and balanced biaxial tension tests, from which the yield stresses and *R*-values are measured. The value 8 is suggested for the exponent *m* for aluminum alloys in Eq. (1). The detailed procedure to calculate the anisotropic coefficients is reported in [79].

1.2.4 Anisotropic hardening model

Accurate modeling for predictions of springback and formability requires advanced constitutive laws describing anisotropic hardening under non-proportional loading conditions [80,81]. Therefore, a recently developed anisotropic hardening model is employed, called the homogeneous-yield-function-based anisotropic hardening (HAH) model, which simulates the isotropic expansion and anisotropic distortion of the yield surface. The summary of the HAH model is shown below, but the detailed derivation can be referred to in Refs. [82,83]. The HAH model uses the distortional hardening concept during loading path changes. The core equation of the model is expressed as follows:

$$\Phi\left(\mathbf{s},\bar{\varepsilon}\right)=\left[\phi^{q}\left(\mathbf{s}\right)+\theta_{1}^{q}\left|\hat{\mathbf{h}}^{\mathbf{s}}:\mathbf{s}-\left\|\hat{\mathbf{h}}^{\mathbf{s}}:\mathbf{s}\right\|\right|^{q}+\theta_{2}^{q}\left|\hat{\mathbf{h}}^{\mathbf{s}}:\mathbf{s}+\left\|\hat{\mathbf{h}}^{\mathbf{s}}:\mathbf{s}\right\|\right|^{q}\right]^{\frac{1}{q}}-\bar{\sigma}_{\mathrm{iso}}\left(\bar{\varepsilon}\right)=0 \quad (6)$$

where ϕ is the yield function before distortion, $\mathbf{s}$ is the stress deviator, and $\bar{\sigma}_{\mathrm{iso}}\left(\bar{\varepsilon}\right)$ is the equivalent stress representing an isotropic hardening part. As mentioned in previous chapter, the Swift hardening law is used for both temper to model the isotropic hardening part. q is a material constant, and $\hat{\mathbf{h}}^{\mathbf{s}}$ is a normalized microstructure deviator, defined as $\hat{\mathbf{h}}^{\mathbf{s}}=\dfrac{\mathbf{h}^{\mathbf{s}}}{\sqrt{\frac{8}{3}\mathbf{h}^{\mathbf{s}}:\mathbf{h}^{\mathbf{s}}}}$. Initially, $\mathbf{h}^{\mathbf{s}}$ equals the deviatoric stress at the initiation of plastic deformation. The two functions θ_1 and θ_2 are defined using the state variables g_1 and g_2, which control the distortion of the yield surface. They are given

as

$$\theta_1 = \left[\frac{1}{g_1^q} - 1 \right]^{\frac{1}{q}}, \quad \theta_2 = \left[\frac{1}{g_2^q} - 1 \right]^{\frac{1}{q}}. \qquad (7)$$

The evolution of g_1 and g_2 depends on the sign of $\hat{\mathbf{h}}^{\mathbf{s}} : \mathbf{s}$. More information on this aspect can be found in Ref. [82].

1.2.5 Marciniak – Kuczynski model

The formabilities of the investigated materials are predicted using the Marciniak-Kucynski(M–K) FLD, which incorporates the measured material properties and corresponding constitutive models [84,85]. In the M–K FLD approach, a preexisting inhomogeneity factor is introduced by the imperfection factor, which is defined as $f_0 = t_0^b/t_0^a$, to initiate localized failure in the groove region. Fig. 5 shows a schematic of the M–K model geometry consisting of homogeneous and groove regions with thicknesses t_0^a and t_0^b, respectively. The stress and strain states in the homogeneous region are calculated by applying the elasto–plastic constitutive models. Then, the deformation state in the grooved region can be obtained by applying the force equilibrium and compatibility condition, which are solved using the Newton–Raphson (NR) method. Failure is assumed to occur when the ratio of the plastic strain rate in the homogeneous and groove zones becomes less than a critical tolerance. The principal loading direction is aligned along RD.

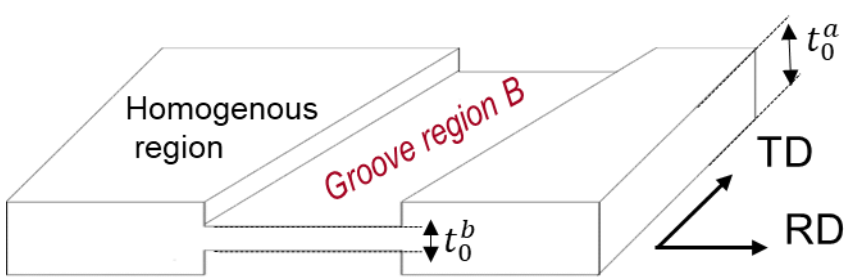

Figure 5. Schematic illustration of the M–K model

1.3 Outline of the thesis

A few papers have been published recently on the advantages of W-temper [1,79–81], but there is still a lack of research on plastic behavior or numerical analysis. Moreover, studies on PLC effects in W-temper on formability have rarely been reported, which requires investigation because the PLC effects can similarly influence results by their own properties or variously by the properties of each material.

Considering the lack of research, the purpose of this thesis is to investigate the influence of PLC effects on formability. First of all, mechanical material properties such as stress-strain curve, anisotropy, non-proportional deformation, and elastic behaviors are measured. Then, the overall formability of w-temper is examined through four kinds of experiments. Even though the w-temper still needs further development to overcome some problems such as embrittlement to adjust practically to the forming process, a study about the influences of the PLC effect on material properties could suggest further insights to investigate other material properties that exhibit PLC effects.

In Chapter 3, a forming limit diagram experiment to verify formability is discussed. Springback is employed using the U-draw bending experiment since springback is one of the critical issues in the automotive sheet metal forming process. The lower elastic modulus of aluminum generally exhibits larger springback than steel, so the springback is also examined. Chapter 4 focuses on a hole-expansion experiment using a conical punch and flat-headed punch to investigate stretch-flangeability (edge crack behavior).

Based on the implementation of experimentally characterized mechanical properties and associated constitutive law in a simulation, the simulation results for the T6 condition are verified by comparing the experimental results. Then, the experimental

results of the W-temper and the finite element analysis results, in which only the mechanical properties are implemented without theoretical modeling of the PLC effect, are compared. Through the comparison of these experimental and simulation results, the influence of the PLC effect on the experimental and approaches to consider the consequences of the PLC effect in terms of numerical modeling are analyzed. The thesis is based on the published papers by the same author [89–91].

2. Material property and characterization

2.1 Material preparation

A commercially produced peak-aged (T6 tempered) as-received aluminum alloy 7075 sheet, hereafter referred to as "T6," is investigated in this thesis. The chemical composition of the T6 sheet is listed in Table 1. This alloy features the addition of Cu and Zn to achieve higher strength in comparison with other aluminum alloy grades.

Table 1 Chemical compositios of the aluminum alloy T6 sheet (in wt.%)

Zn	Mg	Cu	Fe	Si	Mn	Ti	Cr	Al
5.1	2.1	1.2	0.5	0.4	0.3	0.2	0.18	bal.

Sheets of 1.5 mm thick AA7075, in two different tempers, are investigated: one is the as-received condition in a peak-aged temper, i.e., T6, and the other one is solid solution heat-treated (SHT) followed by water quenching, i.e., AA7075-W. Hereinafter, this forming technology and temper is called W forming and -W, respectively. Microstructurally, in the W temper, precipitations are dissolved during SHT and temporarily frozen by the water quenching until they start segregating again by natural or artificial aging. In this W forming process, several process parameters should be determined and examined first, such as SHT time, quenching method, and time between quenching and forming, since the mechanical properties are affected by the process parameters mentioned above.

For SHT time, Chen et al. (2020) and Omer et al. (2018) show that a solid solution heat treatment time between 8 and 30 minutes produced consistent results. Sensitivity tests are conducted to determine the solid solution heat treatment time, as shown in Fig. 6a, and then 15 minutes is chosen conservatively to avoid any uncertainties possibly caused during the heat treatment process.

The quenched high strength aluminum alloy shows different mechanical properties such as yield stress because of residual stress or microstructure based on the quenched conditions [84]. As shown in Fig. 6b, the quenched aluminum 7075 also shows different engineering curves, hence water quenching is used in this thesis.

For the time between quenching and forming, called holding time in this thesis, a negligible difference is observed in the flow stress curves for the time between 30 and 90 minutes, while the flow stress begins increasing after 2 hours. Therefore, the holding time between quenching and mechanical testing or forming is limited in this work to between 15 and 30 minutes to reduce the scatter due to natural aging as shown in Fig. 7, and as Huo et al. (2016) mentioned.

The Figure 8 shows the overall temperature profile of WT forming in which the material in the -W temper is prepared through SHT at 470°C for 15 minutes followed by water quenching to rapidly cool down to RT. This microstructural change in -W temper alters the mechanical properties of the -T6 temper, i.e., it reduces flow stress and enhances ductility in RT forming.

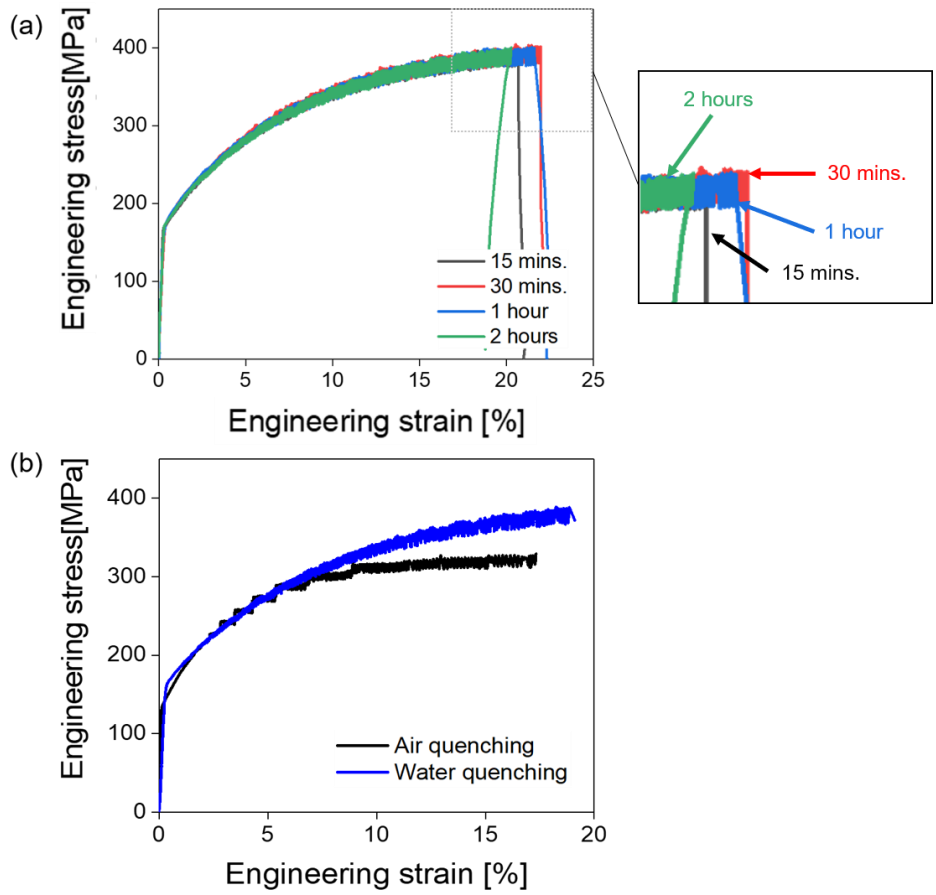

Figure 6. (a) The effect of SHT time on engineering stress-strain curve of -W temper and (b) tensile test cooling curves for quench into water at room temperature and air cooling

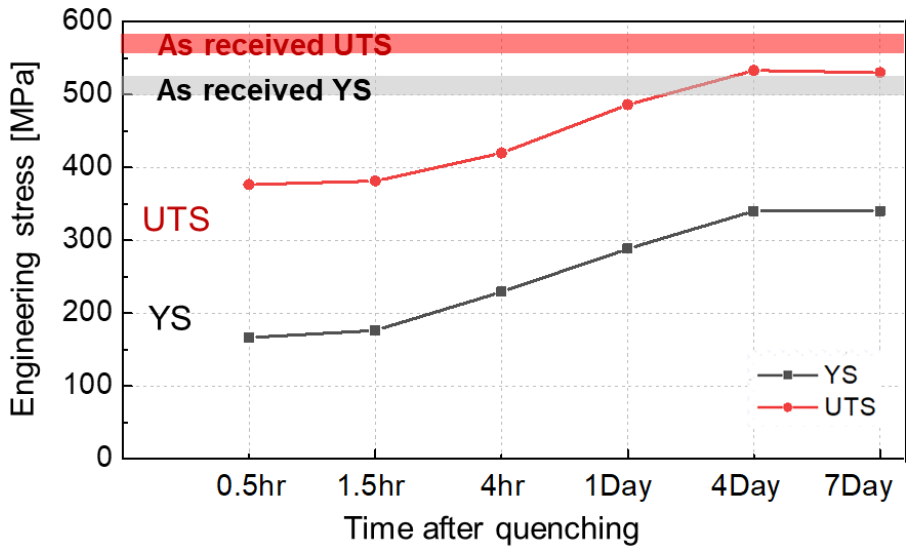

Figure 7. Evolution of yield stress and ultimate tensile stress against time after quenching

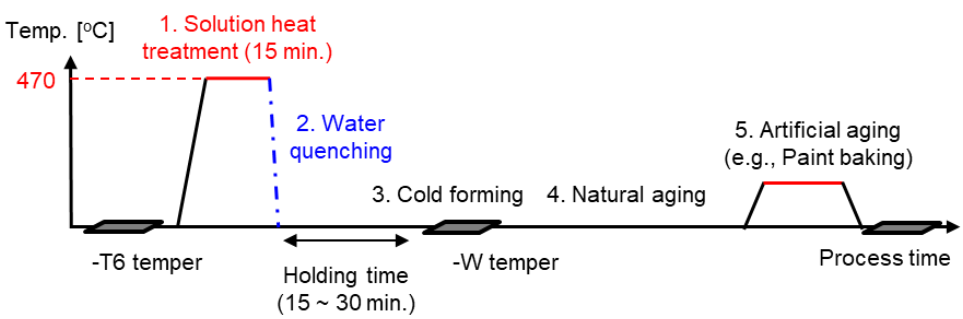

Figure 8. Temperature profile with respect to time of -W temper process

2.2 Bacis mechanical properties and anisotropy

The basic mechanical properties are measured by uniaxial tension tests. The experiments are conducted following the ASTM E8 standard in quasi-static conditions. The strains are measured by a digital image correlation (DIC) technique. Table 2 summarizes the anisotropic plastic properties of the T6 and WT sheets. The strain hardening exponent (n) is also reported by fitting true stress–strain curves along the rolling direction (RD) using the Swift hardening equation; that is, $\bar{\sigma}(\bar{\varepsilon}) = \mathrm{K}(\varepsilon_0 + \bar{\varepsilon})^{\mathrm{n}}$. Here, $\bar{\sigma}$ and $\bar{\varepsilon}$ are effective stress and strain, respectively, and ε_0, K, and n are material constants. Additionally, tensile tests with specimens aligned along 0°, 45° (diagonal direction, DD), and 90° (transverse direction, TD) from the RD are performed. Lankford coefficients (or *R*-value, defined as $\mathrm{R} = -\frac{d\varepsilon_w}{d\varepsilon_L + d\varepsilon_w}$) are also listed in the table. Here, $d\varepsilon_L$ and $d\varepsilon_w$ are plastic strain increments along the longitudinal and width directions, respectively. Figure 9(a) shows the engineering stress–strain curves along RD, DD, and TD for the T6 and W samples. As already shown in the Fig. 2, the x-axis is displayed as $\Delta L/L_0$, with the initial length of the virtual extensometer L_0, and its extension ΔL, and correspondingly, the y-axis is designated as Force/Area [N/mm^2]. Typically, these quantities are reported as engineering strain and stress, respectively. But they are not referred as such in Fig. 2 and Fig. 9(a) because the deformation in -W temper is spatially inhomogeneous, as measured by DIC and shown in Fig. 3. Regarding plastic anisotropy, no significant anisotropy in flow stress is observed in either temper, while the Lankford coefficient, or so-called R-value, shows clearer anisotropy, varying between 0.55 and 1.1 in different orientations. In R-values, local minima appear at RD and TD lower than 1

(plastic isotropy in strain) and with a local maximum at 45°. This will be further discussed, along with the material modeling that it informs. A severe serrated flow stress pattern is noted only for the WT sheets; however, the similar inverse pole figures in Fig. 9(c) confirm similar anisotropy between the T6 and W sheets. The average grain size of T6 and W measured by SEM (SU-70) with EBSD also shows similar results at 19.3 μm and 20.8 $\mu m,$ respectively. For the -W temper, a hydraulic bulge machine is used to evaluate equi-biaxial data and a detailed experimental method following Lee et al. (2013) is identically implemented.

The measured equi-biaxial flow stresses and ratio of plastic strain increments along RD and TD ($r_b = \frac{d\varepsilon_{TD}}{d\varepsilon_{RD}}$) in an equi-biaxial state are as shown in Figs. 10 (a) and (b), respectively. The measured biaxial yield stress normalized by uniaxial yield stress in RD is 0.95, and the rb is 1.01. Again, negligible anisotropy between the uniaxial and biaxial tests is measured for the investigated materials under the W condition.

Table 2 Anisotropic properties of the T6 (T6) and 7075-W(W) alloy sheets

Materials	Orientation	Yield stress [MPa]	UTS [MPa]	UEL* [%]	TEL** [%]	n***	R-value	R_n#	ΔR##
	RD	532	592	18.3	14.7	0.122	0.55		
T6	DD	508	582				1.08	0.857	-0.23
	TD	530	598				0.70		
	RD	166	376	10.4	18.8	0.362	0.58		
W	DD	163	370				1.00	0.816	-0.19
	TD	172	383				0.67		

* Uniform elongation, ** Total elongation at fracture, *** $\bar{\sigma}(\bar{\varepsilon}) = K(\varepsilon_0 + \bar{\varepsilon})^n$

$R_n = (R_0 + 2R_{45} + R_{90})/4$, ## $\Delta R = (R_0 - 2R_{45} + R_{90})/2$

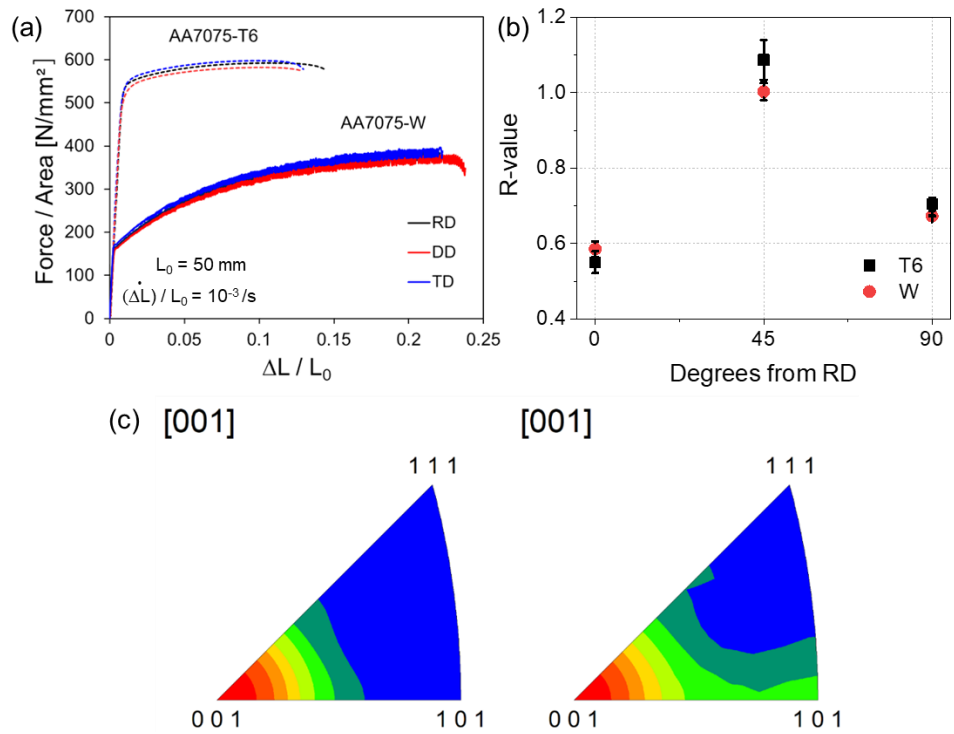

Figure 9. Anisotropic properties of the T6 and 7075-W sheets. (a) Engineering stress–strain curves, (b) R-values in three different directions, and (c) normal direction inverse pole figures of T6 (left) and -W (right)

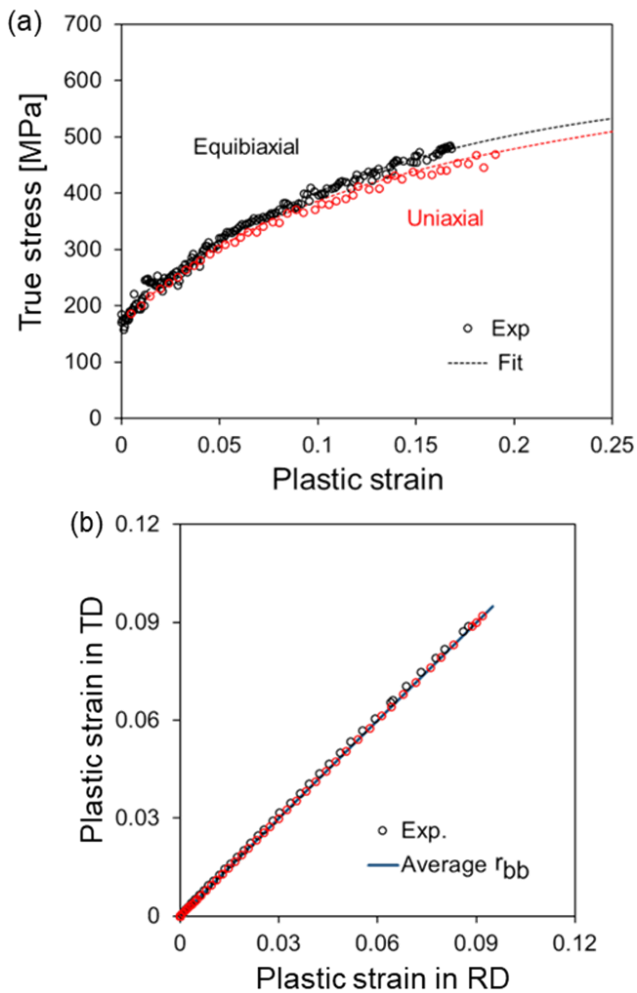

Figure 10. (a) True stress-strain curves of AA7075-W under uniaxial tension in the RD and equi-biaxial tension experiments and (b) plastic strain ratio of TD to RD (r_{bb}) in equi-biaxial tension.

2.3 Compression tesnsion test

A compression-tension test equipped with an anti-buckling plate [87] is conducted to identify anisotropic hardening, including the Bauschinger effect. Figures 11 (a) and (b) show the test specimen geometry and Fig. 11(c) shows measured stress–strain curves with 3 and 6% pre-strains under the compression–tension loading condition. To highlight the Bauschinger effect in the stress–strain curves, the flow stresses, which are assumed to follow the isotropic hardening law, are also plotted in the figure. Preliminary calibration of the compression–tension flow curves is done by compensating the friction and biaxial loading effects [87]. As shown in Fig. 11(c), both T6 and 7075-W show significant Bauschinger effects after load reversal. A small gap in flow stresses between the monotonic and reversed loadings (often denoted as “permanent softening”) is observed for the -W sheet, but is almost negligible for the T6 sheet. The experimental data justify the necessity of using the anisotropic hardening model for the springback simulation.

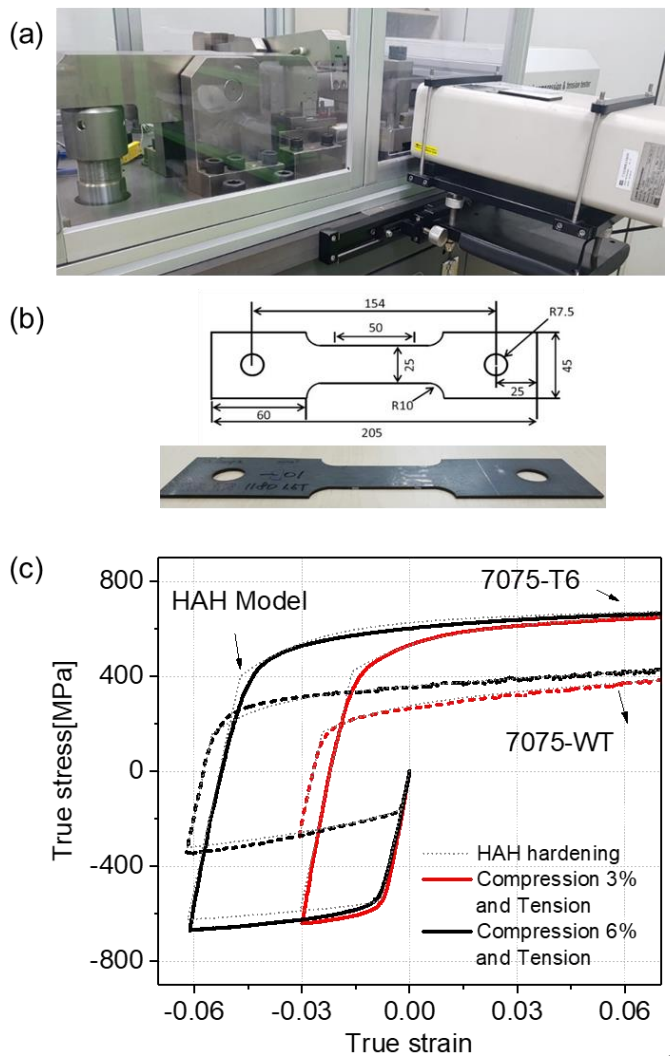

Figure 11. (a) Compression-tension of sheet testing machine, (b) specimen geometry (unit: mm), and (c) flow curves of compression–tension tests for the T6 and -W sheets.

2.4 Loading-unloading test

The main advantage of W forming is enhanced formability at room temperature, which potentially enables conventional cold stamping. Then, in contrast to hot forming, which significantly lowers flow stress, springback after cold stamping might be a critical issue. For the springback simulation, the Bauschinger effect (i.e., lowered yield stress after load reversal [88,89]) in the cyclic loading and the degradation of the apparent elastic modulus are reported to be factors that affect the accuracy of springback prediction [87,89,90]. Therefore, flow stresses under compression-tension loading and the apparent elastic constant, defined as the "chord modulus" in the loading–unloading tests, will be measured for the T6 and 7075-W sheets.

Fig. 12 shows the stress–strain curves under loading–unloading–reloading with different pre-strains. Fig. 12 shows the hysteretic loops, which have been observed for other metals as well, during the unloading and reloading cycles for both materials [90,91].

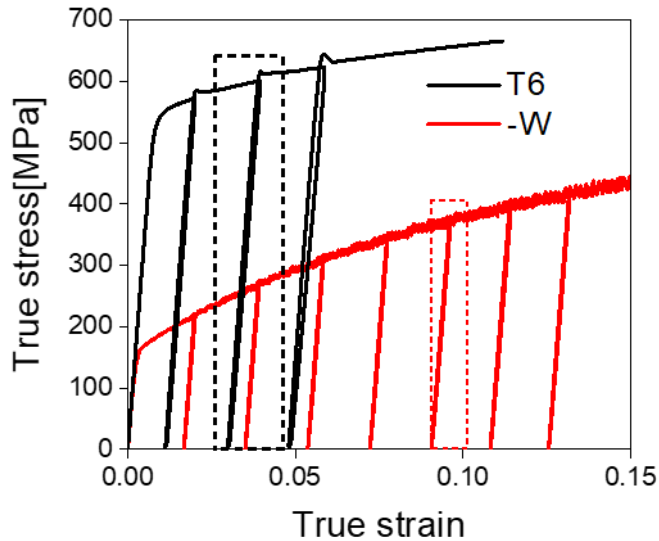

Figure 12. Stress–strain curves of loading–unloading–reloading for the T6 and 7075-W sheets

3. Formability and springback

3.1 Introduction

Several researches are investigated about the feasibility of -W forming process to industrial applications for high strength aluminum alloys. Mendiguren et al. (2016) investigated formability of T6 to form a channel shape of automotive part using -W forming and hot stamping processes. The -W forming showed a comparable result to the hot forming process, and the part can be formed without cracks. Lee et al. (2019) evaluated formability of AA7075 in -W temper by Nakajima test and formed a center floor tunnel, an automotive component, successfully. Schuster et al. (2019) analyzed springback and hardness of a U-channel drawn part using -W forming and hot stamping of 7000 series aluminum alloy. Kumar et al. (2017) reported -W forming showed the greatest formability improvement for 7000 series aluminum alloy compared to other heat assisted forming processes. Still the investigations relatied to constitutive modeling and simulations are rarely reported [103,104].

As a reliable indicator for formability, the strain-based forming limit dagram is conducted for evlauating the formability, the Marciniak–Kuczynski (M–K) forming limit diagram (FLD) approach is used to predict the forming limit curve [105–107].
Note that the analysis on the springback has been commonly disregarded in other elevevated formings due to its negligible amount [108], but springback will be more critical for W forming due to the nature of the room temperature process [109]. For evaluating the springback in the W forming, the U-draw bending test is employed and investigated.

For this purpose, based on the tests for the basic elastic–plasticity properties, mechanical tests under non-proportional loading paths and repeated loading–unloading experiments are conducted. Specifically, anisotropy in yield stress and anisotropic hardening models are employed because they are essential to accurately model the formability and springback in room temperature forming. The non-quadratic anisotropic yield function [79,110] and distortional yield surface-based anisotropic hardening model [82,83,111] are employed to simulate the effect of loading path changes.

The objective of this chapter is to understand the formability and springback of WT high strength aluminum alloy, and to implement them into the FE simulations using properly modeled constitutive equations. [86,112,113].

3.2 Formability of W-temper

3.2.1 Forming limit diagram (FLD) experiment and results

Figs. 13 (a) and (b) show the schematic set-up for the limit dome height (LDH) formability test and specimens for six different deformation paths, respectively. Note that samples 5 and 6 in Fig. 13 (b) have the same geometry but different lubrication conditions. The LDH tests are performed in a universal testing machine equipped with a hemispherical punch (radius of 25 mm), and the blank holding force is 134 kN. The punch velocity is 0.5 mm/min. In this study, the circular grid analysis (CGA) method is used for determining the failed points in the FLD [114], which is reported to be consistent enough to evaluate the surface strains[115–117]. According to the reference[116], the results obtained using the sophisticated DIC technique and CGA methods are comparable. To control the friction in the LDH tests, the blank and punch interface is lubricated using mineral oil and a thin polyethylene sheet. This lubricated condition aided to obtain the failure strain close to the equi-biaxial condition. Figs. 14 (a) and (b) show the measured FLDs of the T6 and 7075-W sheets, respectively. It is observed that the formability of the W sheet significantly improved in the whole strain paths compared to that of the T6 samples. The forming limit values in the plane strain condition, FLD_0, for T6 and 7075-W are 0.091 and 0.154, respectively. That is, formability improved by over 40% with WT. Fig. 14 (c) presents the dome heights at the onset of failure and Fig. 14(d) shows that the formability of the WT sheet improved significantly compared to that of the T6 temper sheet. Particularly, the difference in the formability is more pronounced for the sample with uniaxial condition, or sample 1 in

Fig. 13 (b). The experimental evidence with the formability test results also guarantees the potential application of the WT forming of high strength aluminum alloys at room temperature owing to the improved sheet formability.

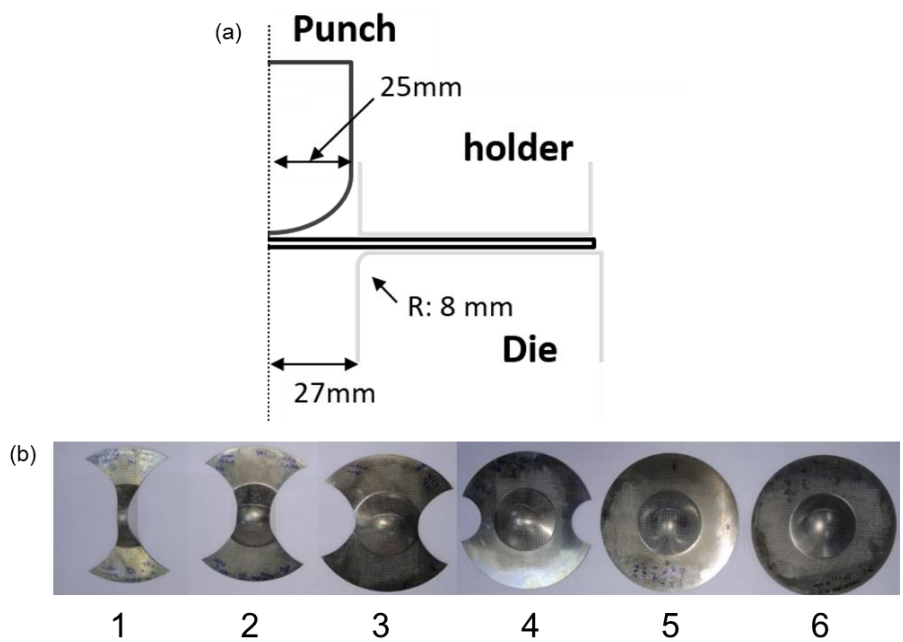

Figure 13. (a) Tool dimensions for the forming limit test, (b) specimens for different loading paths

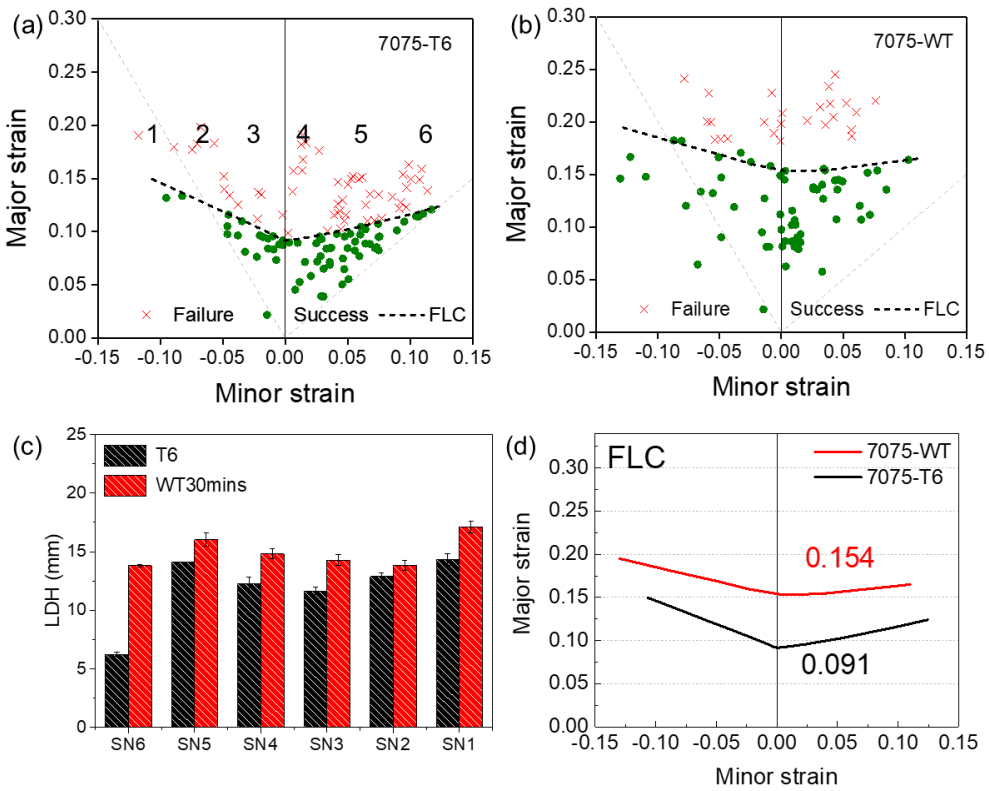

Figure 14. Measured FLD for the (a)T6 and (d) W temper, (c) limit dome heights (LDHs) between the T6 and W sheets, and (d) comparison of the FLC curve between T6 and W

3.2.2 Forming limit diagram prediction

3.2.2.1 Anisotropic plastic yield model

The initial anisotropic properties of the T6 and W sheets are modeled using the non-quadratic anisotropic yield function Yld2000-2d, which will be also used in anisotropic hardening model later. Fig. 15(a) shows the Yld2000-2d loci for the T6 and W sheets using the yield function parameters listed in Table 3. For comparison, the Von-Mises isotropic yield function is also plotted in the figure. The Yld2000-2d criteria for both materials have much sharper corners in the biaxial stress region than those in the Von-Mises yield model. Figures 15(b) and 15(c) presents the results of T6 and W, respectively, about the *R*-value and yield stress variations with respect to the material orientation, and very similar trends in anisotropy are noted. The Swift hardening law, $\overline{\sigma}_{iso}\left(\overline{\varepsilon}\right) = K(\varepsilon_0 + \overline{\varepsilon})^n$, is used for both the T6 and W sheets to model the isotropic hardening part.

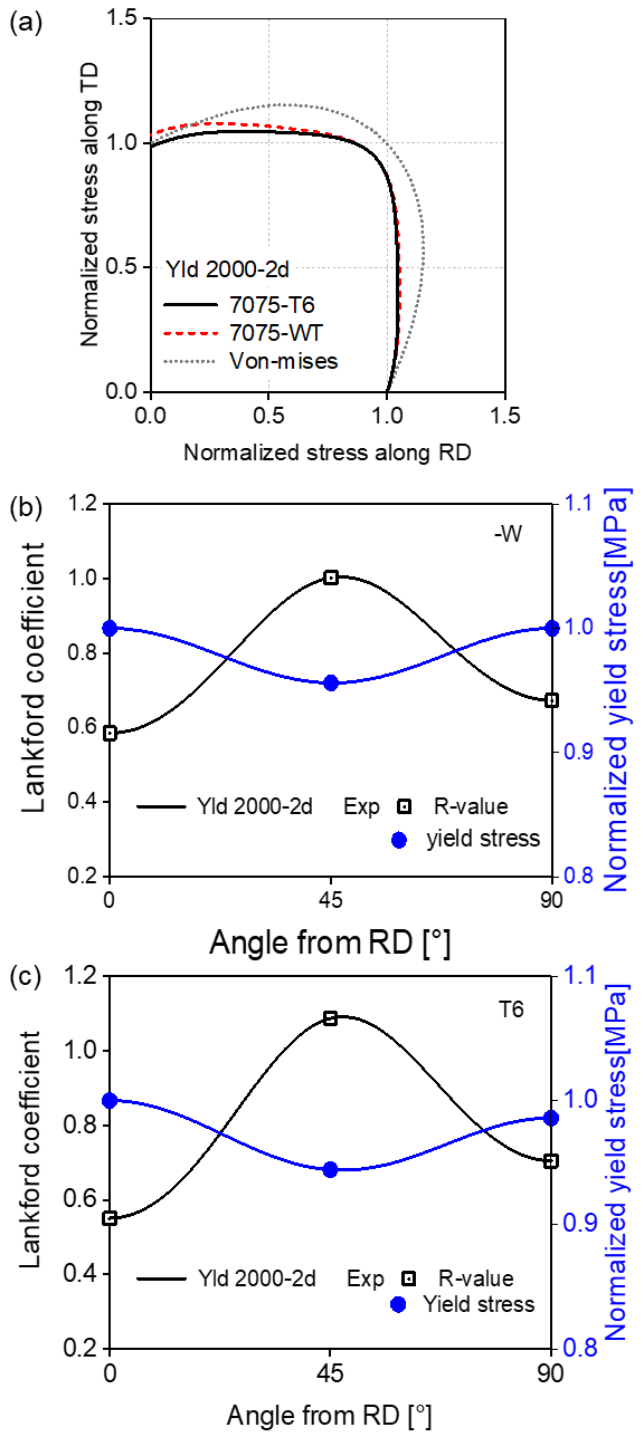

Figure 15. (a) Comparison of yield surfaces, and variations of *R*-value and yield stress along material orientation about (b) T6 and (c) 7075-W sheets

Table 3 Model parameters for isotropic hardneing and yield function

Material	Yield 2000 yield function Parameters							
	a_1	a_2	a_3	a_4	a_5	a_6	a_7	a_8
T6	0.899	1.042	1.006	1.025	1.026	0.991	1.059	1.100
-W	0.983	0.939	1.148	1.023	1.036	1.065	1.025	0.974
Material	Swift model parameter							
	K [MPa]		ε_0	n				
T6	853.1		0.02602	0.122				
-W	863.6		0.0104	0.362				

3.2.2.2 Formability prediction

The Yld2000-2d yield function and Swift hardening law are utilized for the M–K FLD calculations. Only isotropic hardening is used for the formability evaluation because the deformation paths are proportional. The hardening parameters used for the FLD calculation are mentioned in Table 3. The same imperfection factor f_0 (= 0.998) is applied to the T6 and WT sheets to investigate the effect of the material on formability prediction. Figs. 16(a) and (b) show the calculated M–K FLDs for the T6 and WT sheets, respectively. As shown in Fig. 16(a), the forming limit strains from the plane strain (namely, FLD_0) to the uniaxial tension states (or the negative minor strain range) could be better predicted than those in the biaxial region. However, for the 7075-WT sheet, the calculated M–K FLD curve significantly overestimated the measured FLD over all deformation paths even though the anisotropy of the sheet is considered in the calculation. A more thorough discussion on the discrepancy between the calculated and measured FLDs is provided in chapter 3.3.3.

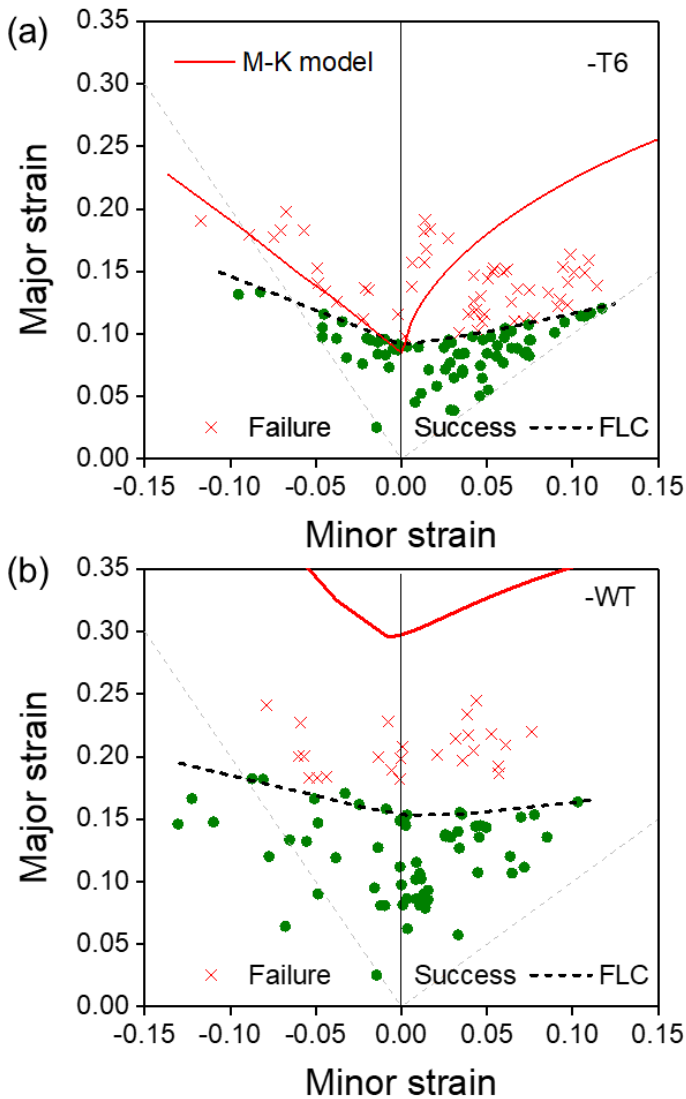

Figure 16. Comparison of FLDs using the M–K theory for the (a) T6 and (b) 7075-W sheets.

3.3.3 Discussion

The calculated FLDs based on the Yld2000-2d and isotropic Swift hardening law did not result in satisfactory predictions. The predicted forming limits are much higher than those of the experiments in the whole deformation paths for the 7075-W sheet and in the biaxial strain paths for the T6 sheet. Insufficient data on plastic deformation could be the cause for the discrepancy between the experiments and the predictions. For Yld2000-2d, most parameters are identified from the mechanical experiments, but the suggested value of 8 is used for exponent m for the FCC polycrystals. Therefore, the FLDs are recalculated by varying the yield function exponent m, which determines the sharpness of the locus in the biaxial stress region. Fig. 17(a) shows the M–K FLDs with different values of m, and these results show improved agreement with the experiment results as the value increases. Fig. 17(b) shows the shapes of the yield functions with different exponents, and once again confirms the sharper corners in the biaxial region as the exponent increases. Based on the above analysis, it is confirmed that the formability of the T6 sheet can be better predicted when using Yld2000-2d with an exponent of over 10 (i.e., $m > 10$). It is noticed that the forming limits in the negative minor strain region are not much influenced by the yield function exponent m.

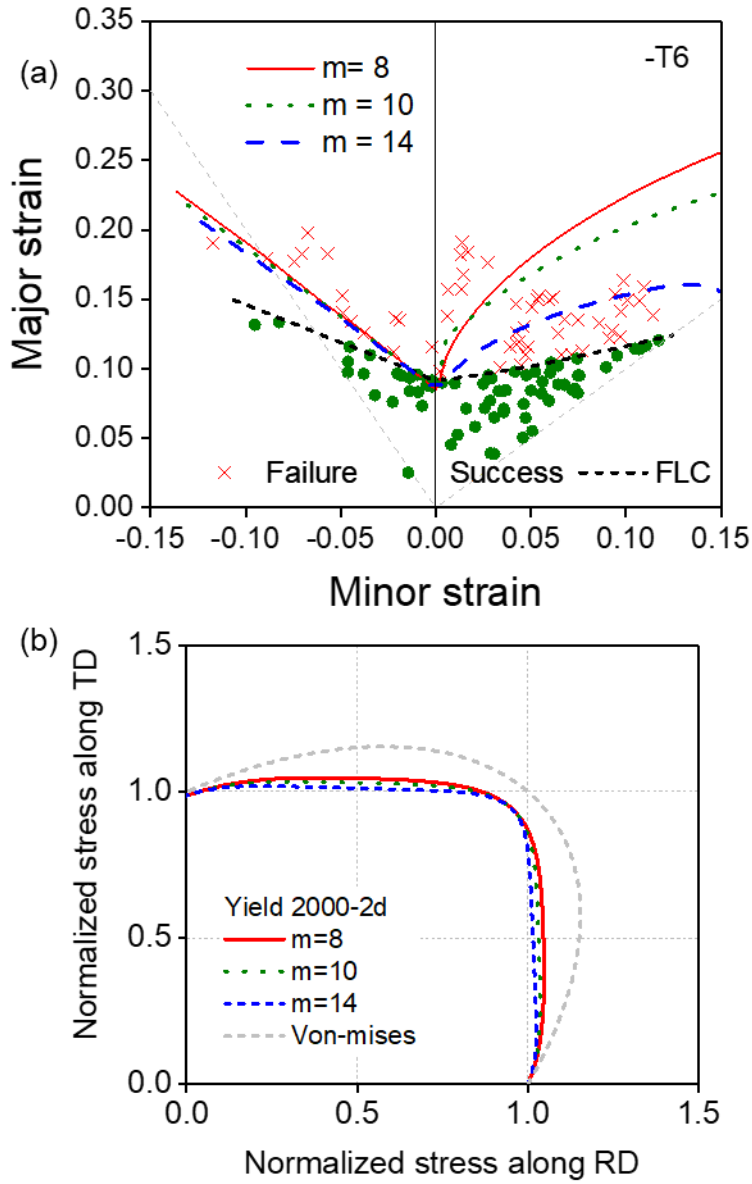

Figure 17. (a) Calculated FLDs for different values of *m* using Yld2000-2d for the T6 sheet, and (b) the corresponding yield surface shapes.

For the 7075-W sheet, the calculated forming limits extremely overestimated the experimental values in the whole deformation modes. In particular, the forming limit in the plane strain mode (FLD_0) deviates too much from the experimental value. It is known that FLD_0 is closely associated with the strain hardening exponent (or n value) of the Swift hardening law. Therefore, a change in the yield function exponent m alone did not improve the overall quality of the forming limit curve. In the experiment, the WT sheet is unique, given the severe serrations in the uniaxial tension stress–strain curve, as already shown in Fig. 2.

Therefore, a more detailed investigation is conducted with the uniaxial tensile curve. The results showed clear Portevin–Le Chatelier (PLC) band propagation during the test, as already seen in Fig. 3. This phenomenon is associated with the dynamic strain aging (DSA) or interactions between solute and dislocations. The serrated flow is known to reduce ductility by triggering an early source of very localized necking in uniaxial tension [118,119]. To check the effect of the DSA on the flow stress curve, the strain hardening exponent n is evaluated using the classical Consìdere condition, which explains the limit of uniform elongation in the uniaxial tension test. The calculated strain hardening exponent n fitting for the Swift hardening law showed a value of 0.36, which is much larger than the measured uniform elongation of 0.22 for the 7075-W sheet. Note that the same analysis led to similar values of the fitted n value and measured uniform elongation for the T6 sheet, which does not present the serrated flow stress curve. Therefore, two different cases are further analyzed. The first case used the Swift hardening law identified from the best fitting parameters, and is denoted as Fitting 1. The other case involved the fitting by constraining the strain hardening exponent n as the measured uniform elongation, and is denoted as Fitting 2. The two sets of parameters

for Fittings 1 and 2 are listed in Table 4. The Swift hardening curves calculated by the two different fitting schemes are shown in Fig. 18(b), and their corresponding FLDs are presented in Fig. 18(c). Note that the fitted flow stress for Fitting 2 marginally overestimates the experimental curve for the strain range of less than 10%, but the overall fitting quality is as good as the best fit. Figure 18(c) shows that the Swift hardening law calibrated using Fitting 2 shows much better agreement with the measured FLD for the 7075-WT sheet.

Table 4 Swift hardening parameters of the 7075-WT sheet for two fitting schemes

	K[MPa]	ε_0	n
Fitting 1 (Best fitting)	863.6	0.01044	0.367
Fitting 2 (with constrained n)	644.3	0.000832	0.220*

* This value corresponds to the uniform elongation and used as a constraint in the fitting of the Swift hardening law.

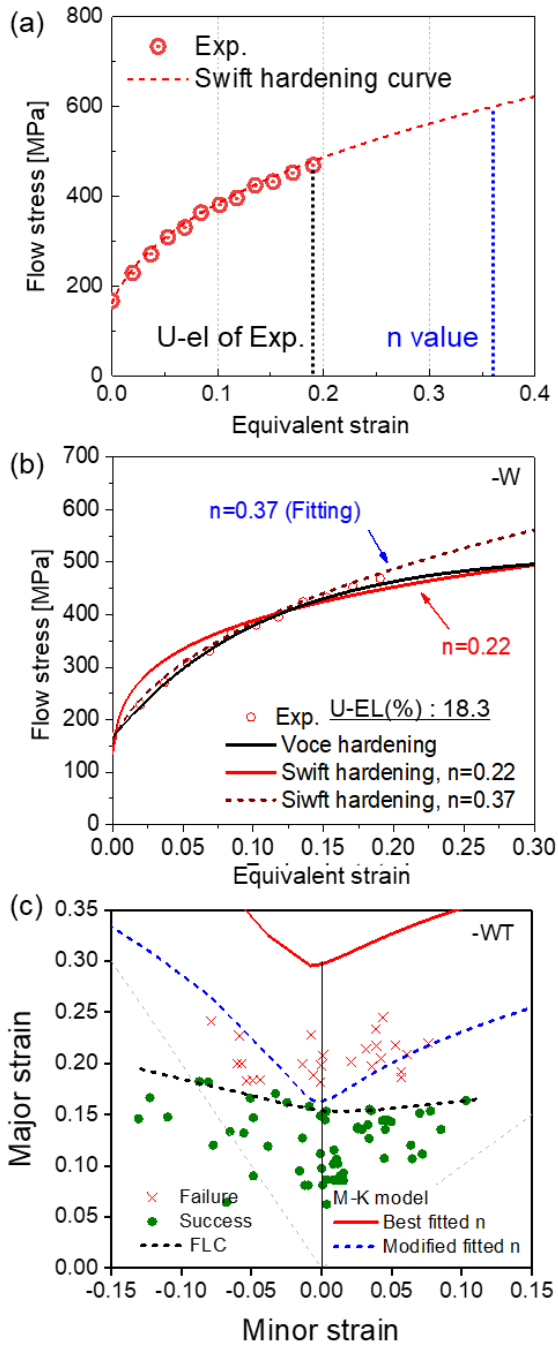

Figure 18. (a) The strain hardening curve with pointing the uniform elongation and hardening ratio, (b) two different fitting schemes with the Swift hardening law and their comparison with the experimental flow curve, and (c) the predicted FLDs with the two fitting schemes.

In the FLD calculations by the M–K model, the major strain in the plane strain mode is (theoretically) nearly similar to the n value of the Swift hardening law, which corresponds to the limit of uniform elongation by the Consìdere condition. Therefore, the calculated M–K FLD with Fitting 1 over-predicted the experimental FLD because it is based on the Swift hardening law fitted to the stress–strain curve. However, in the case of the sheet with serrated flow behavior (or DSA), the serration might lead to early initiation of diffuse necking, thereby decreasing ductility [118,119]. The improved prediction of the M–K FLD for the 7075-WT sheet by the Swift hardening parameters of Fitting 2 can be explained by considering the effect of the serrated flow behavior. In order to quantify the effect of this behavior on the uniform elongation and strain hardening exponent n, a new parameter (n_{ratio}) is defined in Eq. (8).

$$n_{ratio} = \frac{UEL_{Considere}}{UEL_{\text{exp}}} \tag{8}$$

The parameter n_{ratio} is a ratio of the uniform elongation determined from the Consìdere condition ($UEL_{Considere}$) to the measured uniform elongation corresponding to the ultimate tensile strength in the uniaxial tension curve (UEL_{exp}). The effect of serrated flow behavior on n_{ratio} is investigated by collecting material data from the open literature regarding the presence and absence of serrated flow stress behaviors in the uniaxial tension tests. The material group without serrated flow includes TRIP1180, DP490, aluminum alloy 6061-T6, and T6. The first two materials are advanced high strength steels represented by multi-phases and high tensile strength, while the aluminum alloys received peak aged heat treatment. The other material group with

serrated flow behavior includes aluminum alloys 5052-H32, 6061-W, 7075-W, and 7075-W-H4. All the materials in the second group are aluminum alloys with different chemical compositions and heat treatment conditions. “H4” denotes the holding time of 4 h after the quenching in W process. Fig. 19 provides the three values of $UEL_{Considere}$, $UEL_{\exp}$, and n_{ratio} for all the investigated materials. The figure clearly shows that the serrated flow behavior represented by the PLC band formation and propagation can be highly correlated to higher n_{ratio} values than those of materials without serrated flow behavior. Therefore, the discrepancy in the FLD calculation based on the M–K approach might due to the over-estimated strain hardening exponent compared to the experimentally measured uniform elongation. This overestimation might be caused by the highly localized and inhomogeneous deformation patterns in the PLC bands, which cannot be modeled in the simple Swift hardening law (especially when it is identified by best fitting to the stress–strain curve). A more physically based hardening model that considers the microstructure effect during the DSA should be incorporated in the calculation of the FLD.

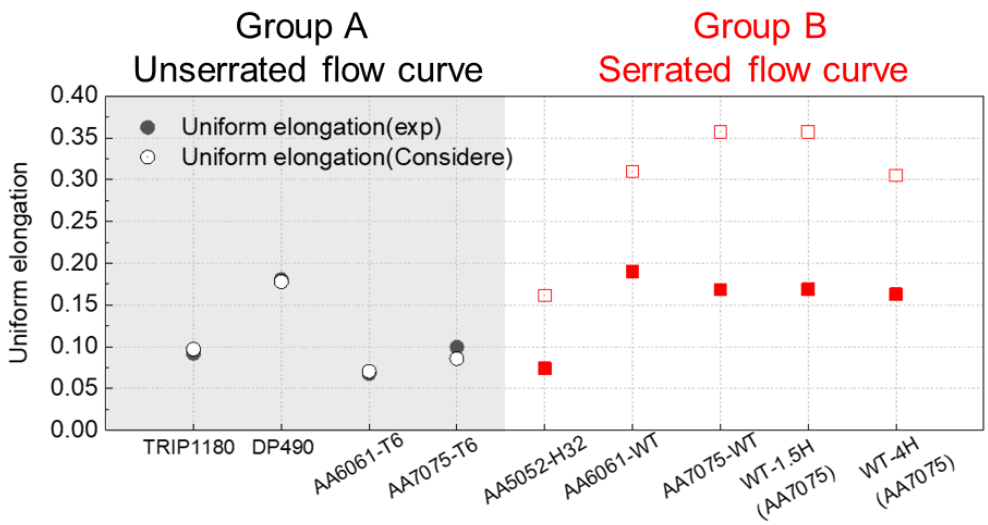

Figure 19. Collected data of uniform elongation determined from the Consìdere condition ($UEL_{Considere}$), uniform elongation corresponding to the ultimate tensile strength in the uniaxial tension curve ($UEL_{\exp}$), and their ratio (n_{ratio}).

3.3. Springback

3.3.1 Experiment and results

The U-draw bending springback proposed as a benchmark problem in Numisheet 2011 is conducted. Fig. 20(a) shows the tool set-up and specimen geometry for the U-draw bending test. The blank holding force is 5.8 kN, and the stroke is 40 mm. After each test, the profile of the springback is quantitatively analyzed using three springback parameters (θ_1, θ_2, and ρ indicated in Fig. 20(b)). θ_1, θ_2 represent the angle change, and $\rho$is the radius of curvature. The specimens after springback, the detailed comparisons of the springback profiles, and the results of measured three parameters are provided in Figs. 21(a), (b), and (c), respectively. Notably, both the T6 and W sheets have considerable springback, but the magnitude of the springback of 7075-W is much less than that of T6. This is because the strength of the 7075-WT sheet is loared by the heat treatment while the elastic properties of both materials are similar. Fig. 21(c) also shows that while two parameters (θ_1 and θ_2) are similar for both materials, a noticeable difference is observed in the sidewall curl ρ. The experimental result indicates that compared to the room temperature forming for the T6 sheet, WT forming is also beneficial in terms of springback.

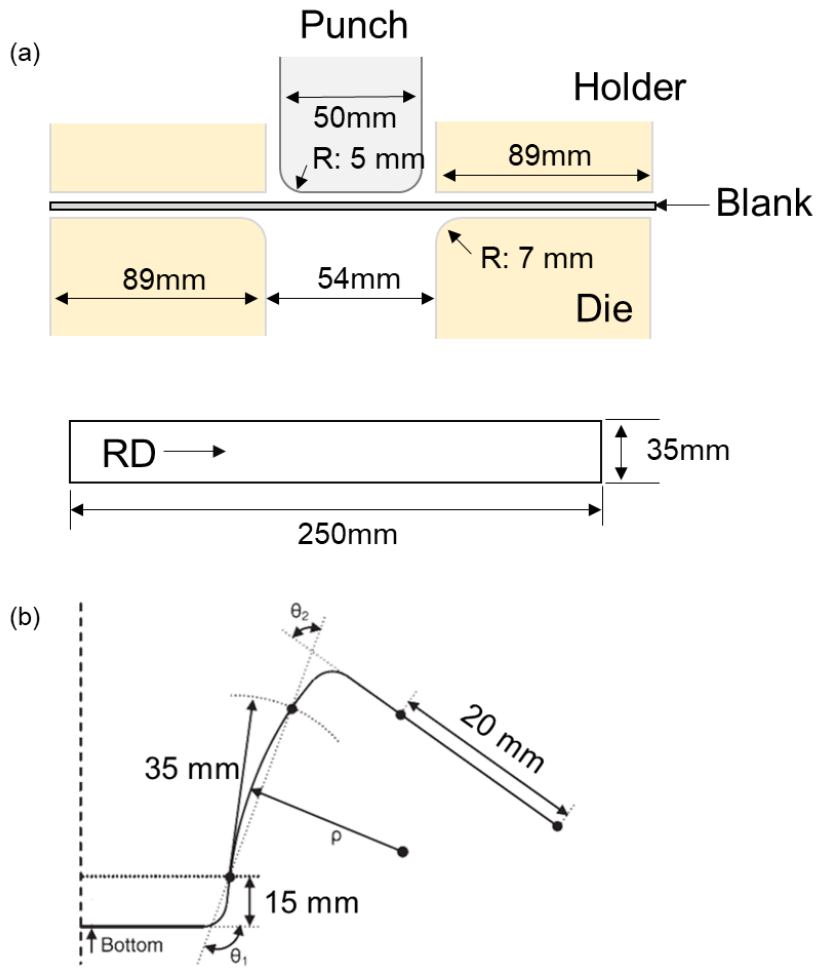

Figure 20. (a) Dimensions of the tools specimen geometry, and (b) springback parameters for the U-draw bending tests.

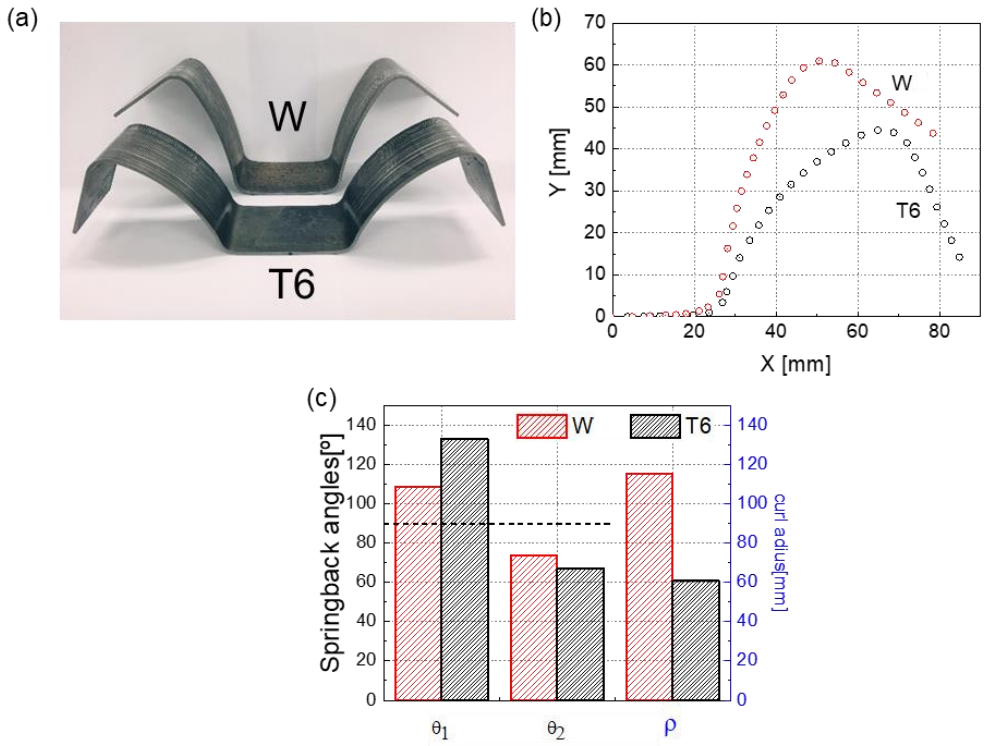

Figure 21. (a) The specimen after springback, (b) comparison of springback profiles, and (c) springback parameters of the T6 and W sheets.

3.3.2 Springback prediction

For accurate modeling and prediction of springback, the anisotropic hardening model called the homogeneous-yield -funcation-based anisotropic hardening (HAH) is employed. Figs. 22(a) and (b) show the calculated flow stress curves under the compression–tension tests for the T6 and W sheets using the HAH model. The model parameters, which are identified using the least squares method, appear in Table 5. It is noted that the HAH model could reproduce the highly nonlinear nature of anisotropic hardening behavior, including the strong Bauschinger effect. More pronounced permanent softening (in comparison with the monotonic flow stress) is well described for the 7075-WT sheet (Fig. 11(c)). This is also evident from the fitted material parameter (k_4) in Table 5, which controls the amount of permanent softening. Note that the smaller the value of k_4, the larger the permanent softening. For comparison purposes, the calculated stress–strain curves by the isotropic hardening are also plotted in Fig. 22. They obviously deviate from the measured stress–strain curves in the reversed loading mode. Additionally, the anisotropic yield function and Swift hardening law written in section 3.2.2.1 are used in springback prediction.

Table 5 Model parameters for HAH model.

Material	HAH Parameters						
	q	k	k_1	k_2	k_3	k_4	k_5
T6	2	30	53.5	587	0.753	0.804	1.40
-W	2	30	125	45.5	0.641	0.659	5.23

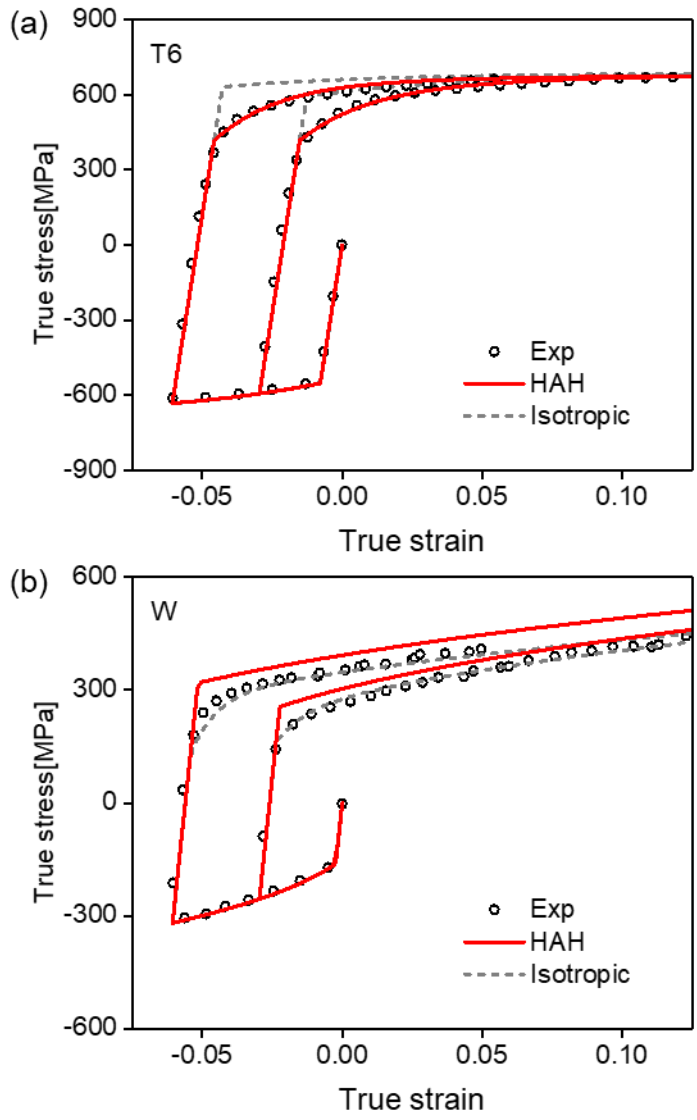

Figure 22. Calculated flow stress curves for compression–tension loadings using the isotropic and distortional anisotropic hardening (HAH) models. (a) T6 and (b) 7075-W sheets

3.3.2.1 Elastic model

The chord modulus, defined as the slope connecting two stress points before and after unloading, is calculated. As shown in Figs. 23(a) and (b), the measured chord modulus could be fitted to the following exponential equation as a function of pre-strain as below:

$$\mathrm{E}(\bar{\varepsilon}) = E_s + (E_0 - E_s)\exp(-\xi\bar{\varepsilon}) \quad (9)$$

Here, E_s, E_0, and ξ are material-specific parameters, which are listed in Table 6. It is found that the chord modulus decreased by nearly 10% of Young's modulus after plastic straining. The stress–strain curves under loading path changes and decreased elastic constants with respect to the plastic strain are used as inputs for the anisotropic hardening models for the springback prediction

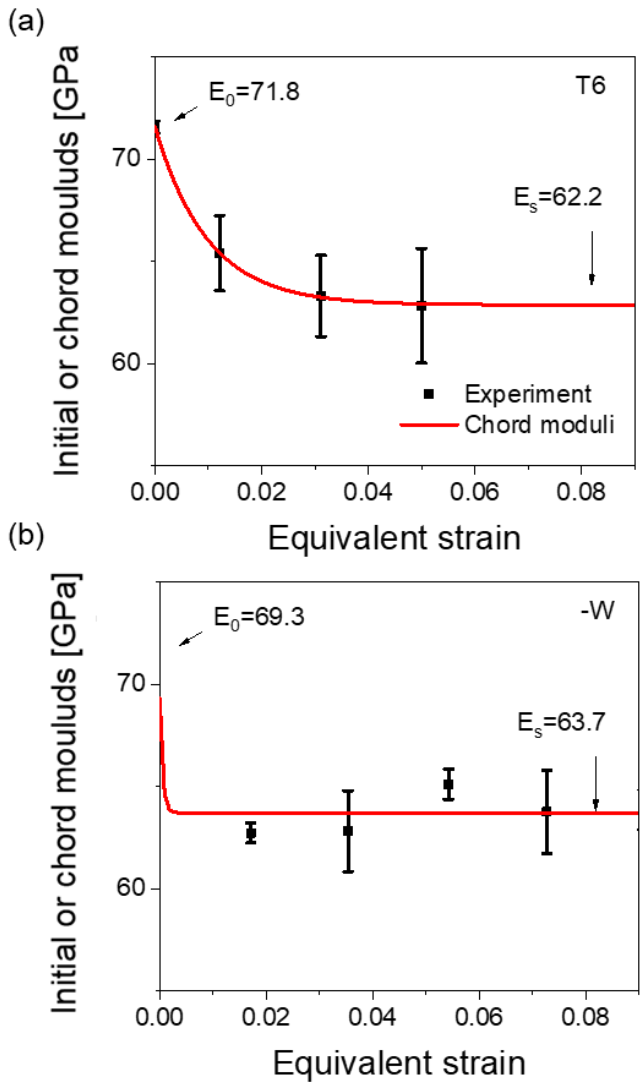

Figure 23. (a) chord moduli of the T6 sheet, and (b) chord moduli of the 7075-W sheet.

Table 6 Elastic properties of the T6 and 7075-W sheets

	T6	7075-WT
E_0 [GPa]	71.8	69.3
E_s [GPa]	63.2	63.7
ξ	111.4	2000

3.3.2.2 The U-draw bending springback simulations

The U-draw bending springback simulations are conducted using the FE software ABAQUS with a user-defined material subroutine [120]. Two different sets of constitutive models are considered in this study. Group 1 consisted of the isotropic yield function, isotropic hardening, and a constant Young's modulus. This set of material models represents the most commonly used set in industrial practice, and is available in most commercial software. On the other hand, Group 2 includes the non-quadratic anisotropic yield function Yld2000-2d, distortional HAH anisotropic hardening law, and Chord modulus approach. This set represents the group of advanced constitutive models for the sheet metal-forming simulations but is not available in commercial FE software. Figs. 24(a) and (b) show the FE model for the U-draw bending springback simulation and mesh for the blank sheet, respectively. The analytical rigid body element and 4-node shell element with reduced integration (S4R) are utilized for the tools and blank sheet, respectively. Only a quarter of the blank sheet is used owing to the symmetries in the material model and sheet geometry. The element sizes of the blank sheet ranged from 0.8 mm to 1.5 mm. Figs. 25(a) and (b) show the springback profiles and parameters predicted by the two sets of constitutive models for the T6 and W sheets, respectively. Interestingly, the predicted springback profiles are in very good agreement with the experiment results even for the conventional basic constitutive models (Group 1). The three springback parameters quantified from the predicted springback profiles also agreed well with the experiment results. Section 4 provides more detailed analyses to explain why the basic set of constitutive models (Group 1) performed equivalently

well for the springback prediction in comparison with the more advanced set of anisotropic constitutive models (Group 2) as well as its disadvantages.

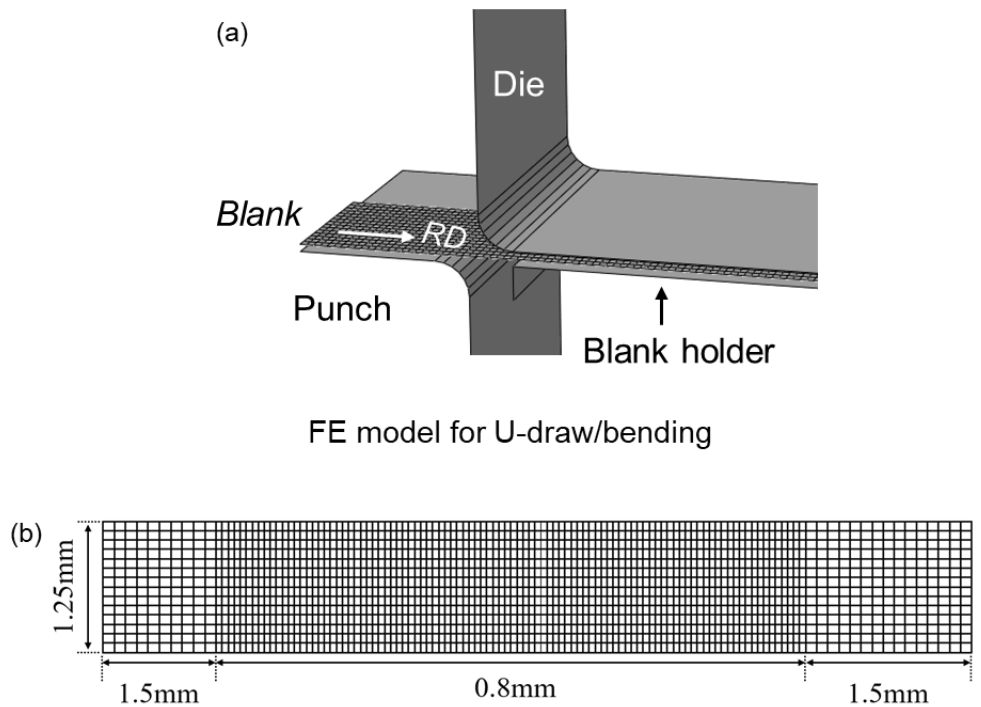

Figure 24. (a) FE model for the U-draw bending tests, and (b) its blank meshes.

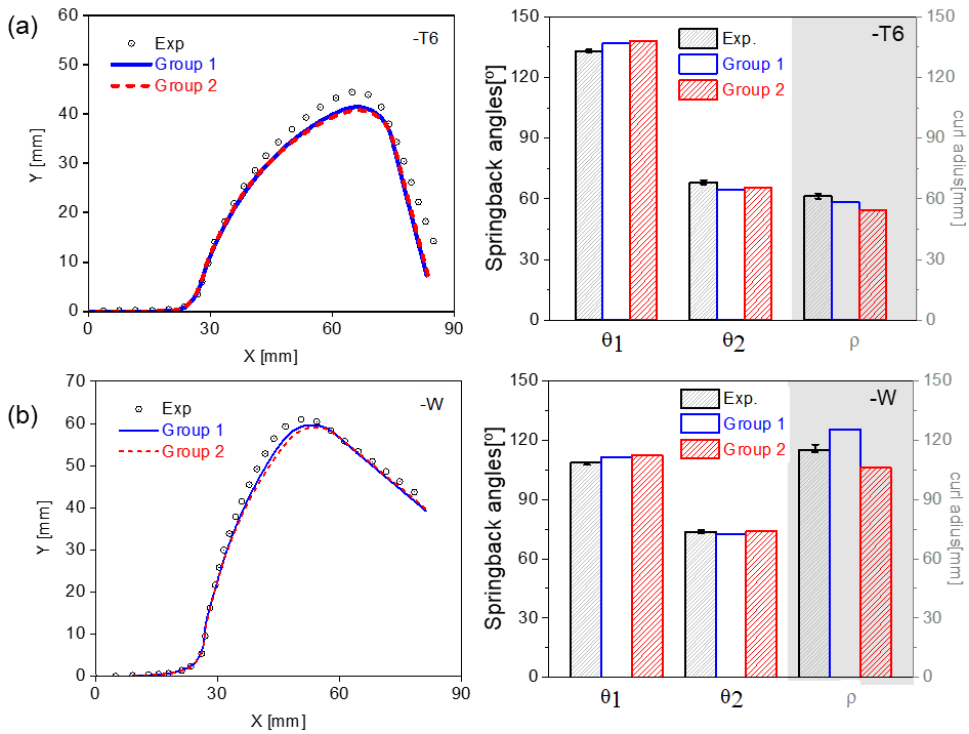

Figure 25. Comparison of the U-draw bending springback profiles and their parameters, predicted with Group 1 and Group 2 for the (a) T6 and (b) 7075-W sheets.

3.3.3 Discussion

The results of both constitutive models representing isotropic and anisotropic hardening provided very similar predictions. This is an unexpected result because it has been commonly reported that the springback of sheet metals can be better predicted when the Bauschinger effect and the nonlinear elastic behavior during unloading are considered. However, in the present result, the isotropic hardening with constant elastic modulus (Group 1) led to almost the same springback profiles as the advanced anisotropic hardening model (Group 2) as per Figs. 25(a) and (b). The possible explanation is as follows. The isotropic hardening model overestimates experimentally measured flow stress due to its proportional expansion of the yield surface, which cannot predict the loared yield stress and significant transient response due to the Bauschinger effect. This larger flow stress in the loading and reverse loading processes should overpredict the springback. However, this overestimation is accidentally compensated for by the constant elastic modulus, which lowers springback.

Although the predicted springback by the isotropic hardening model is as good as that of the anisotropic hardening model, lack of knowledge about the (actual) flow stress characteristic under the loading path change leads to a higher forming load than in the case with the anisotropic hardening model. This is clearly seen in Fig. 26(a) for the T6 sheet. Note that the friction coefficient is determined from the best fitting of the punch force–displacement curve to the simulated one in Group 2. The friction coefficient used for the simulations is 0.17 as determined from best fitting of punch load-displacement curve, which is reasonable considering that the forming condition is non-lubricated. The same simulations are conducted for the 7075-W sheet using the two sets of constitutive

models, and the friction coefficient is the same as that for the T6 sheet, as shown in Fig. 26(b). Group 1 predicted higher punch force than Group 2, as expected. However, both cases underestimated the measured punch force, and the result from Group 1 is even closer to the experimentally measured punch force. The underestimated punch force might possibly be attributed to different friction conditions between the T6 and WT sheets. In fact, it is reported that larger surface roughness results from the serrated flow or DSA effect during deformation of WT sheets [119].

To investigate this presumption, the surface roughness of the T6 and W sheets is measured using the surface roughness measuring system SV-C4500H4 (Mitutoyo). Figure 27(a) shows the measured roughness of the T6 and W sheets. It is notable that the surface roughness after the WT heat treatment increased considerably. The average values of the surface roughness for the T6 and W sheets are 0.19 and 0.235 μm, respectively, which indicates an increase of 23%. Since a rougher surface is known to increase friction between the sheet and tools, the higher roughness of the WT sheet may result in a larger friction coefficient than that of the T6 sheet. Although accurate frictional behavior can hardly be identified due to the complexities associated with the surface roughness, contact pressure, and sliding condition [121], a simple first-order approximation is used for the friction coefficient of the 7075-W sheet by multiplying the ratio of the surface roughness to the friction coefficient of T6. This is because the estimated friction coefficient of 7075-W resulted in good correlations with both springback and punch force. In fact, the linear relationship between the surface roughness and friction coefficient is also reported in other studies [122,123]. The recalibrated friction coefficient of the 7075-W sheet from the surface roughness analysis is 0.21, which is used for the simulations of U-draw bending springback. Figures 27(b)

and (c) show the new springback profiles and punch force versus displacement curves, respectively, using the calibrated friction coefficient of the 7075-W sheet. It is seen that the results of Group 2 with the anisotropic hardening model are in good agreement with the experimentally measured punch force–displacement curve. Interestingly, the springback profiles are less sensitive to the friction coefficient than the punch force, and almost similar predictive quality is obtained with recalibrated friction coefficient.

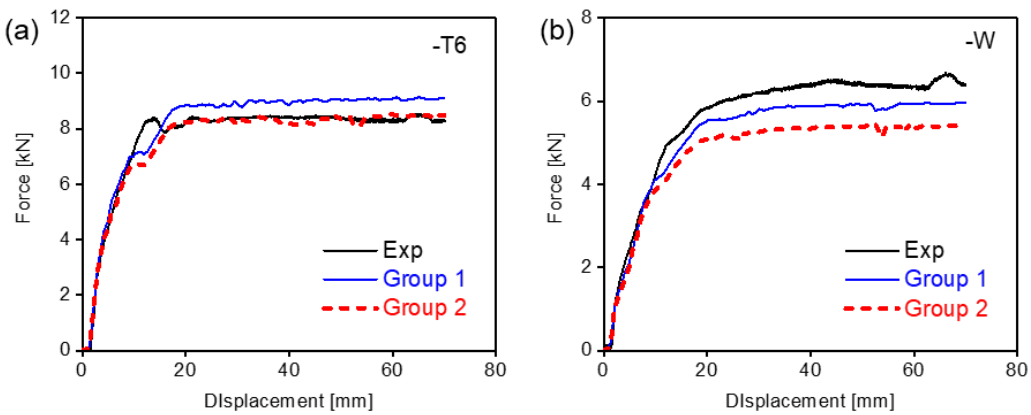

Figure 26. Punch displacement–force curves predicted by different hardening models for the (a) T6 and (b) 7075-W sheets.

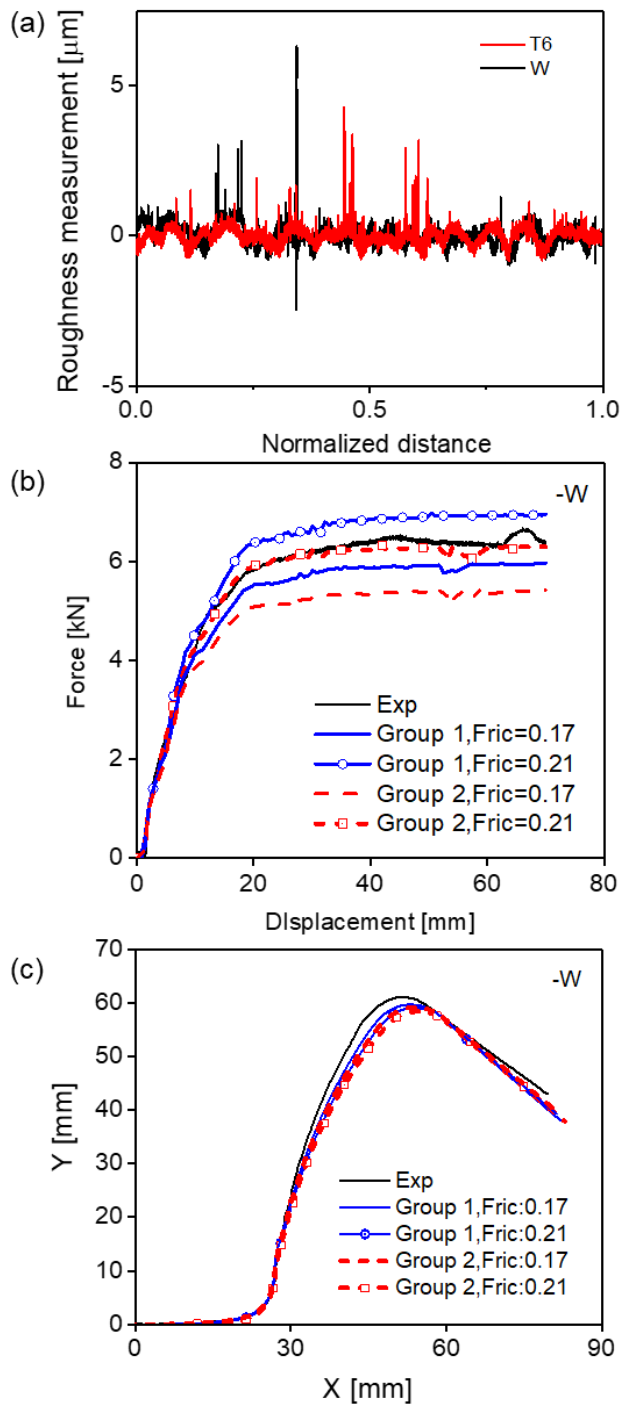

Figure 27. (a) Measured average surface roughness of the T6 and W sheets, (b) U-draw bending springback, and (c) punch force–displacement curves for different friction coefficients of the 7075-W sheet.

3.4 Remarks

This chapter presents the results of experimental and numerical studies on the mechanical properties of W 7075 aluminum alloy (7075-W) sheets in comparison with as-received peak aged 7075 aluminum alloy (T6) sheets and their constitutive descriptions. In particular, anisotropic plasticity in terms of yield function and hardening law under loading path changes is highlighted in the numerical modeling of formability and springback for potential application to the cold forming process with the W high strength aluminum alloy sheets. The M–K formability and U-draw bending springback tests are numerically simulated based on the identified mechanical properties, and they are then comparatively analyzed with the T6 sheet. The combined results of the experimental and numerical analyses led to the following conclusions:

- The 7075-W sheet showed minor anisotropy in strength, while the anisotropy in plastic deformation (or *R*-value) is much higher. Also, the anisotropy of the 7075-WT sheet is very similar to that of the as-received T6 sheet (before heat treatment). In other words, the SHT followed by water quenching did not change the texture of the investigated aluminum alloy sheets.
- The investigated 7075-W and T6 sheets showed considerable anisotropic hardening under loading path changes. The hardening is measured by continuous compression–tension tests. The anisotropic hardening showed a large Bauschinger effect and transient hardening behavior. The permanent softening between the monotonic and reversed flow stresses is only marginally observed in the 7075-W

sheet. Moreover, the loading–unloading test revealed a reduction of approximately 10% in the apparent elastic constant compared to the initial Young's modulus.

- The initial sheet anisotropy of the 7075-W sheet is well modeled by the plane stress non-quadratic anisotropic yield function Yld2000-2d, and its anisotropic hardening behavior is suitably modeled by the distortion-based HAH model.
- The M–K FLD model calculated from Yld2000-2d and the Swift hardening law along with standard material parameters showed considerable discrepancy from the measured FLDs. In particular, the predicted FLD for the 7075-W sheet significantly overestimated the formability in the whole deformation paths, while the over-prediction of the FLD for the T6 sheet is noted only for the biaxial deformation paths. The discrepancy between the calculated FLD and experiment results is analyzed in terms of the yield function exponent and the strain hardening exponent of the Swift hardening law. The larger exponent value in Yld2000-2d could better predict the formability of the T6 sheet. For the 7075-W sheet, the overestimation of ductility (or the strain hardening exponent) by the best fitted Swift hardening model might be attributed to the serrated flow behavior and PLC band propagation due to the dynamic strain aging. The re-calibrated Swift hardening law that considered the measured uniform elongation (or strain hardening exponent) as an additional constraint for fitting provided better agreement with the experiment results of formability.
- The springback profiles are well predicted by the distortion-based HAH model and the chord modulus approach for both sheets. Interestingly, the classical isotropic hardening with a constant elastic modulus also predicted the springback profiles well. This coincidence between the predicted springback from the conventional

isotropic and advanced anisotropic hardening models could be discussed in terms of the difference in the flow strength at load reversal and the treatment of elastic modulus degradation during unloading.

- However, the classical isotropic hardening model over-predicted the punch force–displacement curve due to its overestimation of flow strength after the loading path change, while the anisotropic hardening model predicted it well owing to its capability to consider the Bauschinger effect under load reversal. Finally, the underestimated punch force for the 7075-W sheet could be explained by the roughened surface quality after WT heat treatment, which virtually increases the friction coefficient.

The present chapter also reported the improved formability and loared springback with the 7075-W sheet in comparison with the T6 sheet. Therefore, the W process can be potentially utilized for manufacturing high strength aluminum sheets at room temperature as an alternative to the warm and hot forming processes.

4. Stretch-flangeability

4.1 Introduction

The edge cracking behavior of a hole edge is described through stretch-flangeability, also called hole expandability. The stretch-flangeability of sheet metal is one of the crucial formability parameters in sheet metal forming using deep drawing processes, and it is generally expressed as the hole expansion ratio defined as:

$$Hole\ \ expansion\ \ ratio, HER\ \ (\lambda)\ \ [\%] = (d_f - d_i)/d_i \quad (10)$$

where d_f and d_i are the diameters after and before the experiment with the central hole, respectively. A related study has existed since 1948 [124], and for mild steel, stretch-flangeability is not an issue. Numerous studies on HER have been conducted extensively since 2010 [125], as some AHSS steels have greatly limited use due to their low hole extensibility. Yamada [126] showed that the stress state at the hole edge is uniaxial, and in many other studies, it has been reported that the stress state at the center hole edge in the hole expansion experiment is in a nearly uniaxial tensile stress state [127–129]. However, the researchers [127,130–133] also noted that the mechanical properties obtained from only uniaxial tensile experiments are not sufficient to predict HER. The stress gradient that exists along the radial direction from the edge of the hole within the specimen of the HE experiment is the main reason that produces a different material behavior between the HE experiment and the uniaxial tensile experiment. Paul (2020) stated the principal reasons come from the different conditions of the two experiments: 1) stress gradient, 2) numbers and location of “necking,” 3) free edge condition, and 4) deformation history in the specimen.

Even though numerous studies have tried to correlate HER with various mechanical properties obtained from a uniaxial tensile experiment, the relationship between HER and material parameters still needs to be further investigated to clarify it. Furthermore, many papers reported the close relationship between PUEL and HER, which means that the hole-expandability of w-temper could be poor. Therefore, instead of predicting the results based on uniaxial tensile experimental data, hole expansion should be investigated for verifying the overall formability. The effect of the hole fabrication method on HER is first investigated using a conical punch.

Punch geometry and hole preparation methods have a significant impact on HER results, so their effects are also considered in HE experiments. Because different punch geometries exhibit different HER values due to dissimilar deformation paths [125,127,134], both conical and flat head punches are employed to evaluate stretch-flangeability. For a conical punch, where the punch and hole edges are in direct contact, the effect of the hole preparation method is also investigated with two different hole preparation conditions. Although not standardized methods, HE experiments, also called flat-bottom or flat-head punches, are also performed, as the experiments can be investigated using digital image correlation techniques to capture the in-plane expansion of the hole and material behavior during experiments. The mechanical behavior captured during the experiment is compared with the predicted results of the finite element simulation to investigate the influence of the PLC effect on the flat-headed HE experiment.

4.2. Hole-expansion using conical punch

4.2.1 Introduction

Prediction of forming limit has been performed using a forming limit diagram (FLD); however, edge fracture, also called edge cracking, of some material is hardly predicted accurately just by the FLD results in a finite element method during the stretch-flanging process [135,136]. Therefore, in addition to evaluating formability with the FLD, the stretch-flangeability of aluminum -W temper should be investigated. Although the hole tension test [137] evaluated the stretch-flangeability as well, however, the HE experiment has been commonly accepted for verifying HER in sheet metal forming. The HER value is highly dependent on several factores: mechanical property, microstructure, punch geometry, fabrication method of the hole edge [125].

Many studies have tried to figure out the correlation of HER and various mechanical properties evaluated from a uniaxial tensile experiment such as yield stress (YS) [128,131], the ratio between YS and UTS [128,138] , UTS [128,131,138], strain hardening component [139], strain rate sensitivity (m) [126,133,140], total elongation [131,141], reduction of area (ROA) [127,142], post uniform elongation (PUEL) [141,143,144], normal anisotropy [134,140] and so on. Paul (2014) and P Larour et al. (2020) gathered tremendous data from published papers and previous experiments to analyze the relation between parameters and HER values in detail. Paul (2014) reported normal anisotropy, PUEL, strain rate sensitivity, and fracture toughness as dominant factors on determining the HER, while Larour et al. (2020) selected dominant factors as the main r-value to n-value ratio and conventional tensile test mechanical properties

in the middle or at the minimum thickness location of the fractured specimen. The correlation between HER and material parameters needs additional investigation to make the relationship clear.

As mentioned in previous section, because many papers still report the close relationship between PUEL and HER, the hole-expandability of w-temper, which shows extremely short PUEL, needs to be investigated. The W-temper represents enhanced uniform elongation than the T6 condition, but w-temper also shows extremely short post uniform elongation of less than 1% in the engineering stress-strain curve, which is even less than a quarter of PUEL in T6.

Another factor, the influences on the HER value by the hole preparation method, have been studied in various papers. Kerelova [145] investigated the HER values of two AHSS using three different hole fabrication methods and the result was that defects and damage generated to the hole edges during the preparation procedure have a negative effect on HER. [146,147] also noted that the lowest HER results with hole fabrication as shearing than other methods due to burrs, surface roughness at hole edge, and nucleated voids in SAZ. Furthermore, accumulated damage [148] and inevitable micro-cracks [144,145,148] from the shearing process at the hole edge were also reported as generating a detrimental effect on HER.

Considering the effect of hole fabrication, in this section, a conical HE experiment with two different hole preparation procedures was performed to study the influence of hole preparation on the edge cracking behavior of aluminum alloy 7075-T6 and AA7075-W temper, with hole punching as the standard method and wire cutting. In the shearing process, shear drop and shear surface depend on clearance [147,149,150];

therefore, the constant clearance used in this conical HE experiment is 15 %. The clearance ratio (c) is defined as:

$$\textit{Clearance ratio, } c\ [\%] = \frac{(d_D - d_P)}{2t} \times 100 \quad (1)$$

where d_D, d_P and t are the diameter of the die and punch, and thickness of the sheet, respectively.

For the microstructural approach, the conical HE experimental results of T6 and -W are scrutinized from macro to microscale and standard light optical microscopy (LOM), scanning electron microscopy (SEM) with electron backscattered diffraction (EBSD), confocal laser scanning microscopy (CLSM) are employed to analyze the effect of fabrication of the hole edge.

4.2.2 Experimental procedure and results

The material is aluminum alloy T6, using solid solution heat treatment W temper. Because of experimental constraints, 7075-T6 1.0t was used only in the conical HE experiment chapter. Chemical composition and basic mechanical properties are shown in Appendix 2 for comparison with T6 used in the previous chapter. As well as the overall basic mechanical properties overlap, Hyun et al. (2002) showed that the HER value is around 35%, with a difference of 5% depending on the thickness change even with 1 mm and 2 mm thickness in the HE experiment. Here, only microstructure investigation is mainly performed to reduce possible differences in thickness and chemical composition disparity.

Following the standard ISO 16630:2009, HE experiments are conducted using a conical punch with a cone angle of 60 °and a hydraulic sheet metal testing machine to expand a central hole with a diameter of 10 mm. The inner and outer diameters of the hole are measured to obtain the average diameter. Fig. 28 shows a schematic diagram of the tool geometry, specimen, and measurement of hole diameter. A constant punch speed of 2.8 mm/s is used in the experiment and blanking holding force is constantly controlled at 30kN during the experiment. Because sufficient force prevents draw-in of the specimen, the draw-bead is not employed.

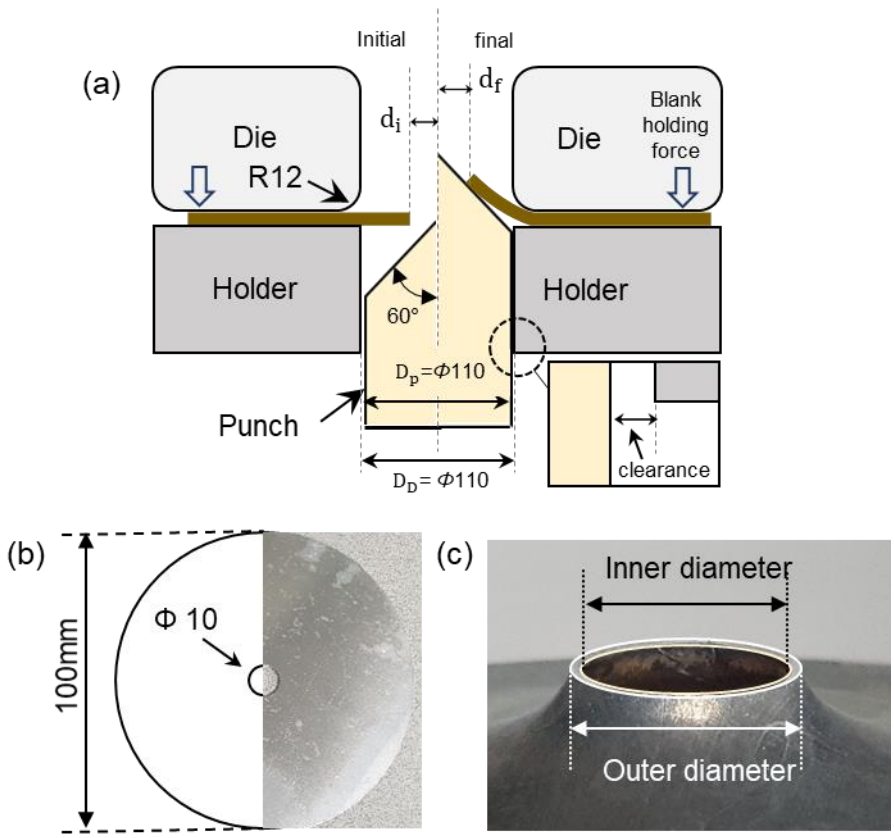

Figure 28. Schematic diagram of conical HE experiment: (a) tool geometry, (b) specimen, and (c) measurement of hole diameter

The initial central hole of specimens is prepared using two methods: punching (shearing) and wire EDM cutting. The specimen is cut along the rolling direction into a square of 100 x 100 mm^2. Experiments are carefully conducted to maintain consistent contact surfaces of punches and samples in both the HE experiments and the hole preparation process by shearing. The experiment is stopped when the reaction force measured from the punch is dramatically decreased by generating cracks at the edge of the expanding hole. The diameters of the outer and inner radius of the hole are measured by Vernier calipers in at least four different locations. The final hole diameter d_f evaluated after fracture is determined by averaging the outer and inner results, and the measured values are shown in Table 7.

HER is calculated as shown in the previous equation (10). In this paper, the specimens prepared with holes through the shearing process and the wire EDM cutting process are called punched specimen and wire-cut specimen, respectively. Similarly, the evaluated HER values in the HE experiment using a punched specimen and wire cut specimen are also called punching HER and wire HER, respectively. The punch force-displacement curve, the conical HER experimental results, and measured fractured hole diameters of both tempers and methods are represented in Fig. 29.

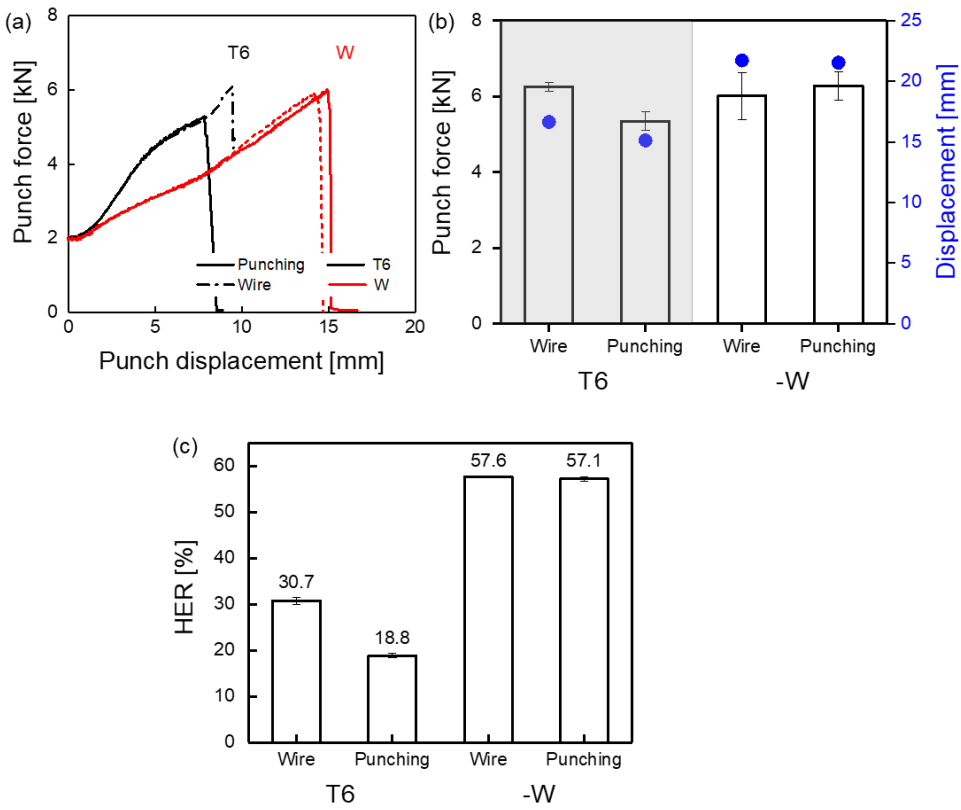

Figure 29. Comparison of the conical HE experimental results of the two tempers corresponding to the initial hole fabrication methods: (a) punch force-displacement curves, (b) the results of punch forces and displacements, and (c) the HER values

Table 7 The measured final hole diameters of the fractured hole in T6 and -W

Temper	Hole fabrication method	Avg. diameter
T6	Wire	13.1 mm
	Punch	12.0 mm
W	Wire	15.8 mm
	Punch	15.7 mm

The -W temper shows higher HER values for both hole preparation methods, even though the -W temper has shorter post uniform elongation than T6. These results will be discussed in detail in the next section considering other material properties of tempers. About the T6 condition, the wire represents 1.63 times higher HER values than the ones for punching, which are 30.7 % and 18.8 %, respectively. The HER results of -W showing similar HER results in wire and punching are dissimilar from T6 and other previous papers. Because the similarity in plastic anisotropy between the two heat treatment conditions should show similar results in plastic deformation, this interesting result will be discussed in the chapter again.

Figure 30 shows the fractured specimens of both tempers and methods, with solid arrows showing the location of the major cracks. Additionally, the crack locations in other experimental results are in Table 8. The main cracks in the fractured specimen of the hole prepared using wire EDM are located near RD or TD, while the fractured specimen of the hole prepared using punching has several cracks in varius locations such as RD, DD, and TD. In the results of -W temper, the cracks are at RD and TD for fractured specimens in both hole preparation methods.

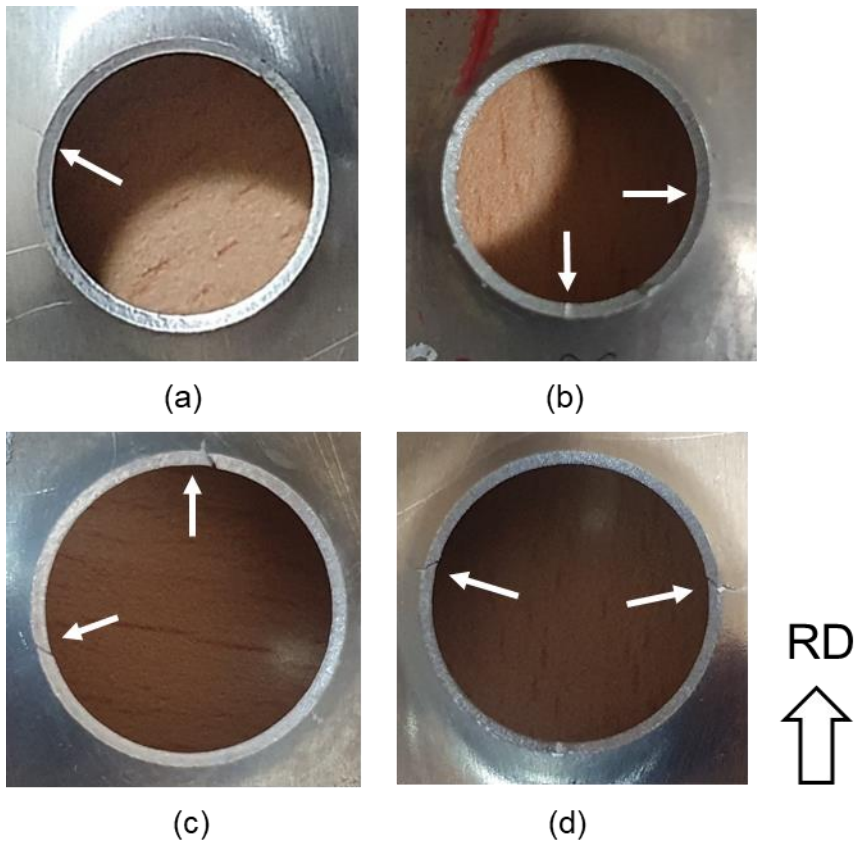

Figure 30. The appearance of cracks at the hole edge in fractured specimens for both tempers and methods: (a) punched specimen of T6, (b) wire cut specimen of T6, (c) punched specimen of –W, (d) wire cut specimen of -W

Table 8. Crack locations in other experimental results

Temper	Hole fabrication method	Specimen			
		# 1	# 2	# 3	# 4
T6	Punch	TD	DD	DD	RD, TD
	Wire	TD	TD	RD, TD	RD, TD
W	Punch	RD,TD	RD	RD,RD,TD	RD
	Wire	RD, TD	RD, TD	TD	

4.2.3 Discussion

4.2.3.1 The HER values of T6 condition

The wire HER showed a HER value increased by more than 60% compared to the punching HER, which is a consistent tendency with the results of other papers. The main reason for different HER values is the deformation histories in the specimen during hole preparation [125,127,133,145,151]. From the macroscopic investigation, the tested specimen with a hole prepared by wire has two main locations showing cracks near RD and TD, since the R-value, which partially governs plastic deformation, shows a lower value near RD and TD than DD, as shown previously in Fig. 9. However, the tested specimen of the hole prepared by punching shows several cracks at multiple locations without any dominant orientation. This discrepancy in the crack direction indicates that the plastic deformation near the hole edge and the residual stresses induced by the shearing process are involved in the final deformation behavior along with the anisotropic effect.

To identify the damage induced by the hole fabrication procedure, specimens of the two fabrication methods are investigated before the HE experiment with light optical microscopy (OM) and SEM (SU-70). All cross sections analyzed through OM and SEM are from the rolling direction for consistency. OM images and SEM images of a cross-section area are shown in Fig. 31. A comparison of surface qualities in the cross-sectional area obviously shows that the damage and hole surface at the hole edge induced by punching fabrication is clearly identified.

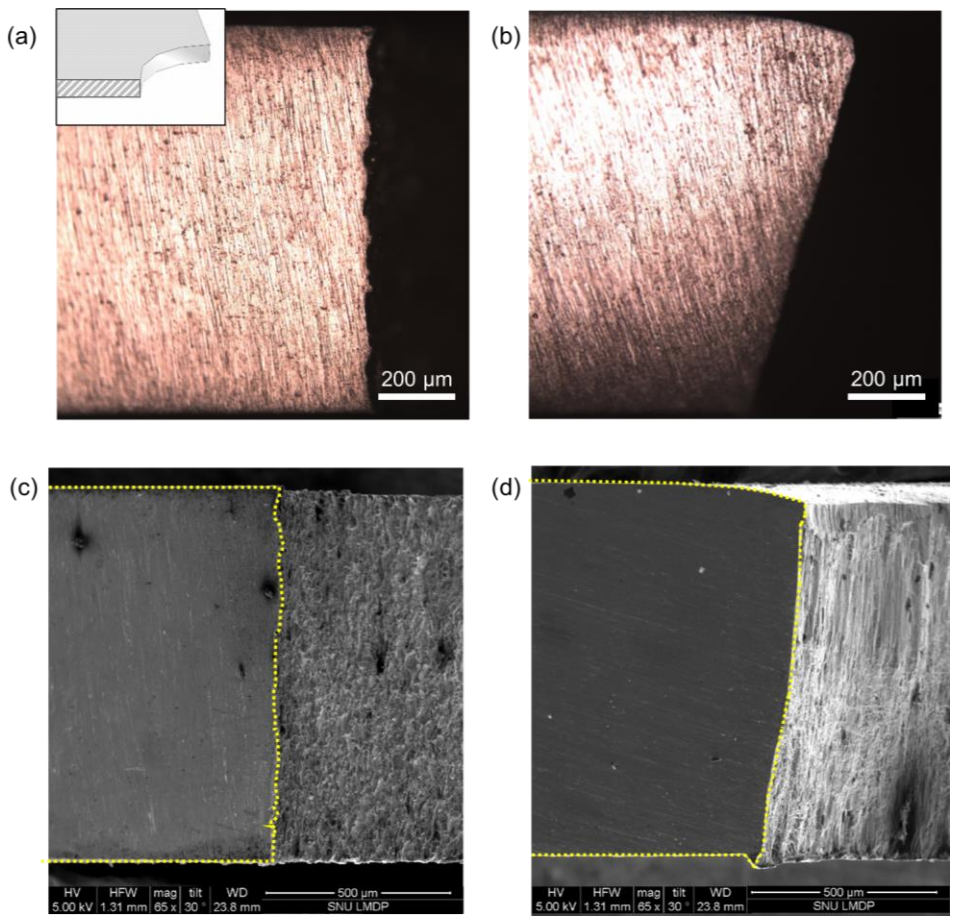

Figure 31. OM and SEM micrographs of cross-section area showing differences in surface quality. OM images in the (a) wire-cut specimen, (b) punched specimen, SEM images in the (c) wire-cut specimen, and (d) punched specimen

The wire cut specimens shows minor deviations in the surface cross-sectional view of the edge within the thickness, while the cross-sectional area of the sheared hole shows a distinct surface change within the thickness, indicating severe plastic deformation because the perimeter of the hole is forced to fail through the shearing process. The cross-sectional view of an edge in a sheared hole is characterized by four regions: roll-over, sheared zone, fractured zone, and burr. The roll-over is formed as the blade contacts the sheet and the surface bends. The shear deformation occurs by the blade piercing the sheet in a vertical direction through the blade, forming a sheared face. As stress is accumulated, cracks are initiated and propagate through the remaining thickness of the sheet by falling apart in the lower part, forming a fracture area. Burrs often appear as a protrusion of metal at the edge. The ratios of each region are measured based on the SEM images and shown in Fig. 32 and Table 9.

Table 9. The averaged ratios of each region measured from SEM images

Zone	Normalized ratio
Roll-over	0.06
Sheared zone	0.07
Fractured zone	0.87
Burr	Apprearance

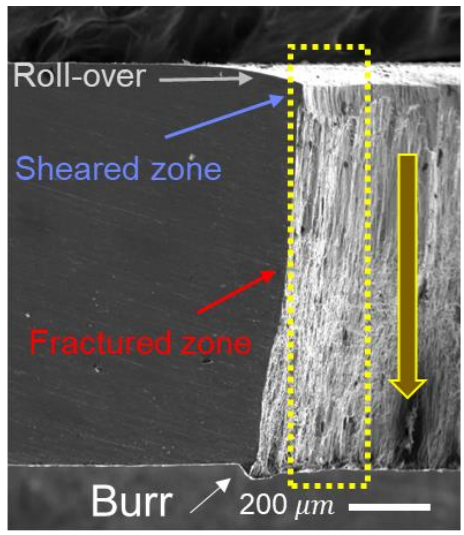

(a)

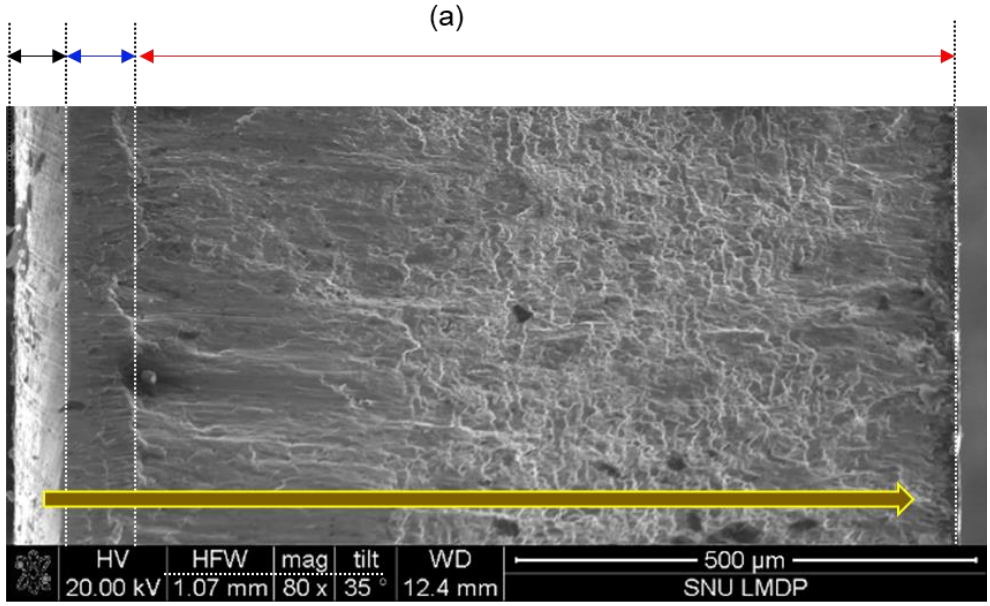

(b)

Figure 32. SEM micrograph of the surface of the hole edge showing (a) representations of the four deformation regions and (b) determined proportions.

The accumulated deformation induced by the shearing process behind the hole edge is measured proximately through the microhardness distribution along the radial direction since the microhardness is also an indicator of work hardening.

Vickers hardness measurement is used for evaluating microhardness with 0.1 Hv and two parallel rows are measured at 0.1 mm intervals in at least three specimens for each condition. The microhardness profiles obtained for both edge conditions are plotted in Fig. 33, and the graph shows negligible microhardness differences even near the hole edge between the specimens from the two hole preparation methods. The reason for the similar microhardness distribution of the two conditions is considered to be the low hardening ratio of the material. As shown in Appendix 1, the yield stress and ultimate tensile stress are 504 MPa and 581 MPa, respectively, meaning that the ratio of the two mechanical properties is only 1.15. The microhardness measurement might be unsuitable since the stress difference is only 77 MPa among 581 MPa, which is only 24 microhardness differences using the translation table of strength to hardness (ISO 18265).

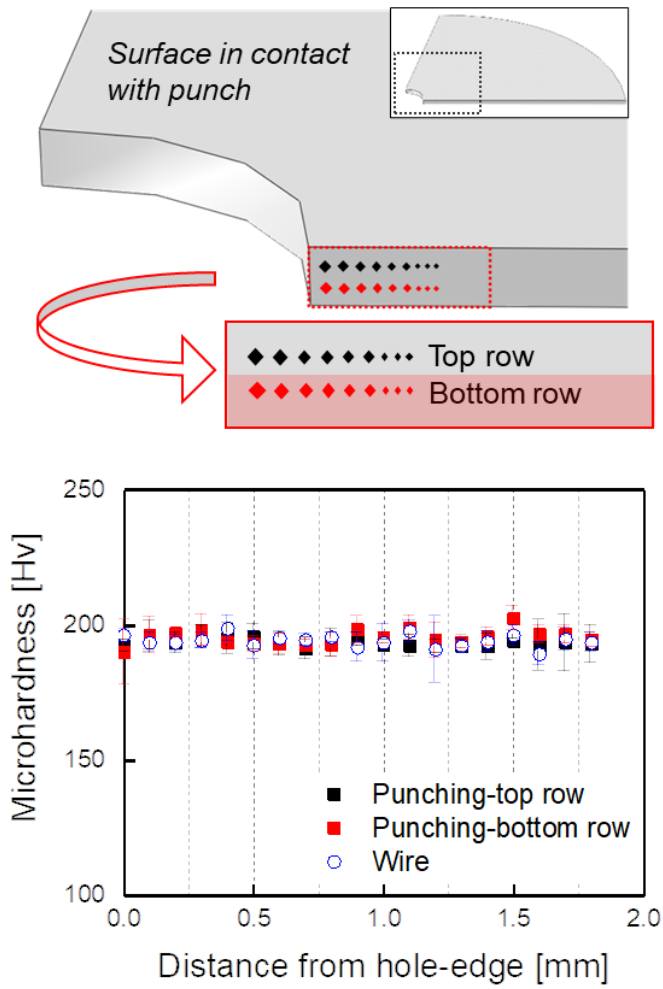

Figure 33. Microhardness profiles of the punched specimen against distance from the hole edge in the rolling direction

However, the accumulated deformation at the hole edge by punching procedure is visible in previously measured cross-sectional images. For verifying the deformation behind the hole edge, a kernel average misorientation (KAM) map is measured by EBSD with SEM, which measures local misorientation and then indicates the amount of distortion. The measured area is 120 μm x 180 μm with 0.45 step size, and the measured KAM map in Fig. 34 shows higher distortion near the hole edge but a sharp decrease along the radial direction.

This shear affected zone behind the hole edge exists within a very limited region near the edge of around 200 μm in the measured specimen, which is too small to capture via Vickers hardness measurement. Fig 35 shows the KAM map of the punched hole and wire-cut hole, which clearly shows the accumulated damage caused by plastic deformation by the shearing process, which has a consistent tendency with the SEM image of the cross-sectional area and other papers [127,147,150]. Pathak et al. (2016) stated the shear affected zone induces micro-void nucleation and causes cracks to initiate, thereby reducing the HER values. Therefore, it is concluded that the measured cross-sectional view of the edge and the measured KAM map within the thickness along the radial direction show that the HER value of hole fabrication by punching is lower than that of the wire-cut one due to the deformation and damage at the vicinity of the hole edge by the punching process.

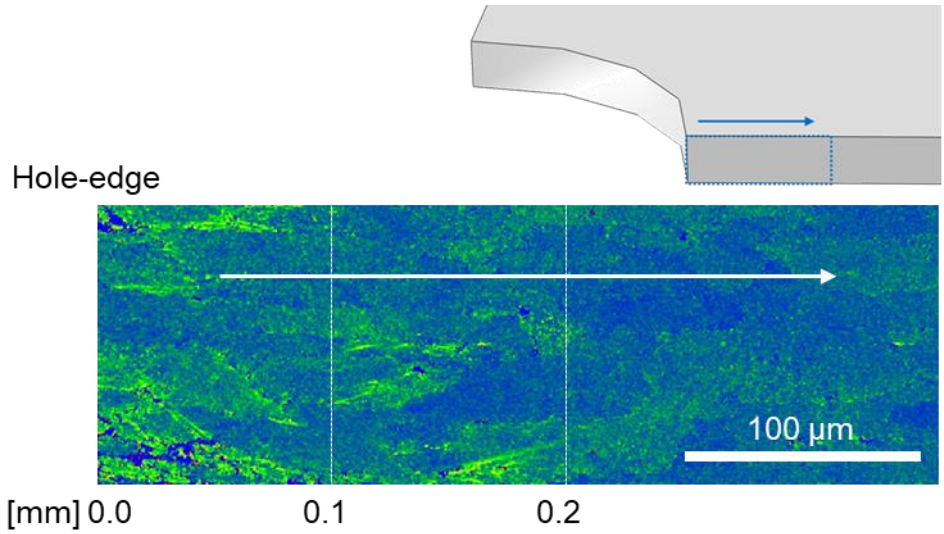

Figure 34. KAM map within thickness of punched specimen (120 μm x 180 μm)

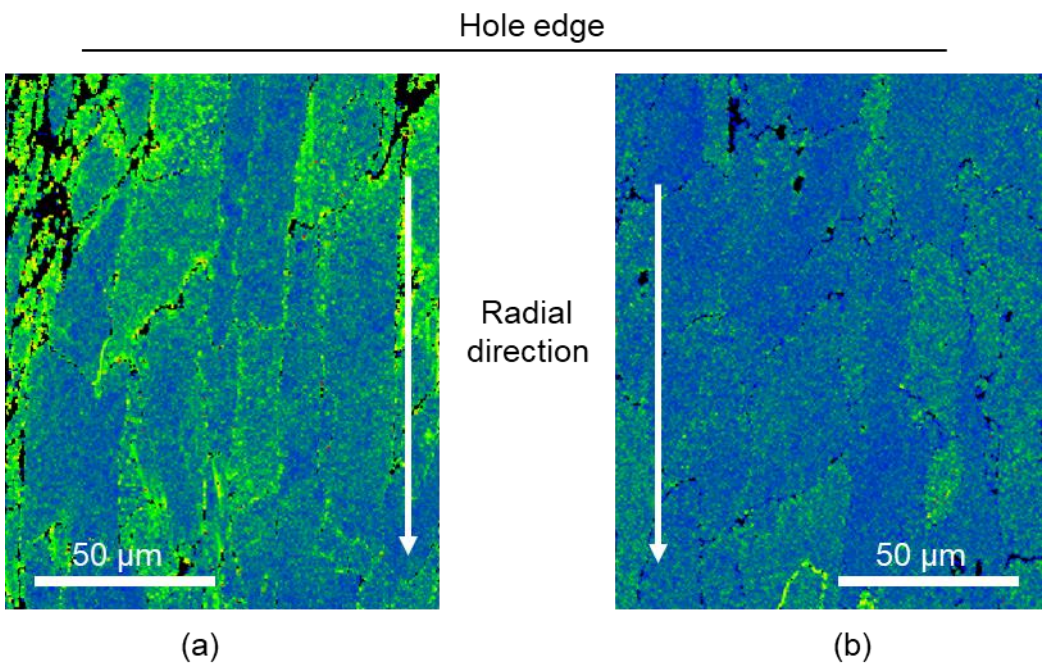

Figure 35. KAM map within thickness of (a) punched specimen and (b) wire-cut specimen (120 μm x 150 μm)

4.2.3.2 The HER values of -W condition

The HER values of both conditions in -W temper exhibit similar results, as shown in Fig. 29, and this trend is inconsistent with the HER results of T6 condition and other previously published papers, as it is generally accepted that the lowest HER value appears in the punched specimen due to the accumulated deformation near the hole edge [127,152,153]. As shown in Fig. 36, the edge part surfaces of fractured specimens in both hole fabrication methods captured by confocal laser scanning microscopy (CLSM) also show similar results.

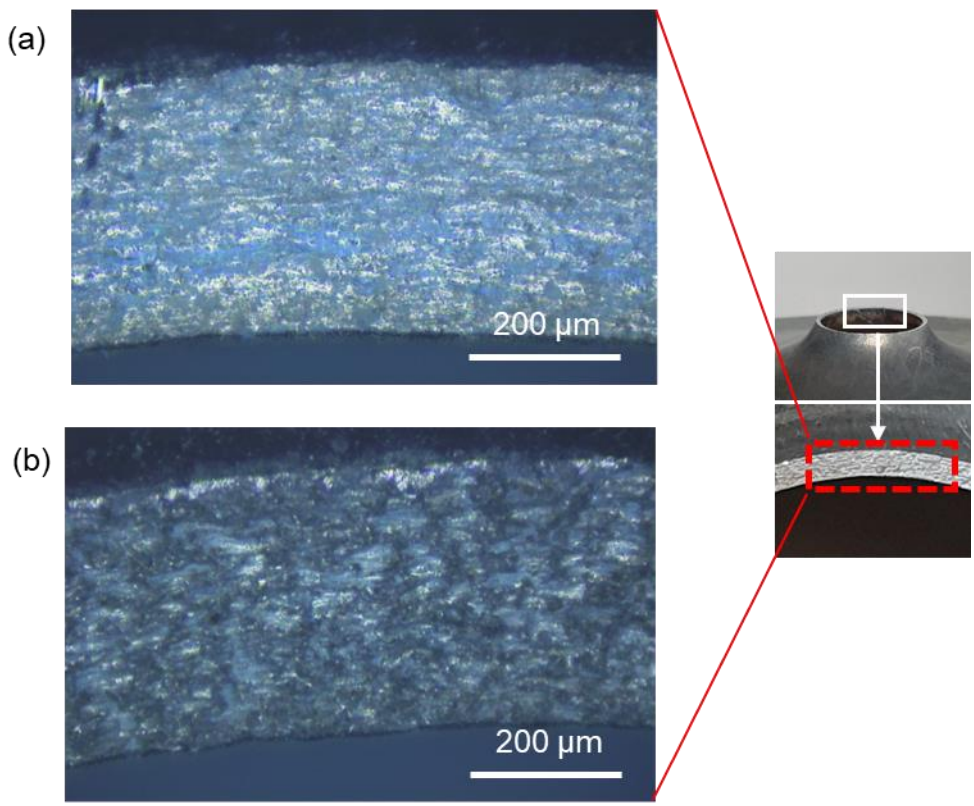

Figure 36. CLSM micrograph of edge part surfaces in fractured specimens of (a) punched specimen and (b) wire-cut specimen after completion of HE experiment.

The major difference between T6 and -W temper is that in the case of -W temper, the part of precipitates is dissolved by SHT. Considering that the recrystallization temperature of aluminum is below 470 ℃, the most promising explanation is that SHT alleviated the deformation caused by the shearing process. Two approaches are employed to validate this: 1) conducting a HE experiment with the process modified and 2) measuring the microstructure of the hole edge.

To determine the effect of SHT on HER values, a newly modified process is performed, consisting of the same process, but in a different order. The original HE experiment sequence using a punched specimen consisted of three steps of a shearing process -SHT-HE experiment, but the newly modified process sequence is arranged as SHT-shearing process-HE experiment, as shown in Fig. 37, and is called W-SPH after the first letter of each step. For convenience, HER values according to the modified process are called W-SPH HER in this paper, and the specimen prepared in the new sequence is called W-SPH specimen. What the original process and the modified process have in common is that when doing HE experiments, the sheet is under the -W temper. There are two differences between the two processes: the sequence of the SHT and punching process, and the tempering state of the sheet when performing the shearing process. In this experiment, the holding time between the quenching and forming process is maintained at 15-30 min to maintain the same -W properties when performing HE experiments.

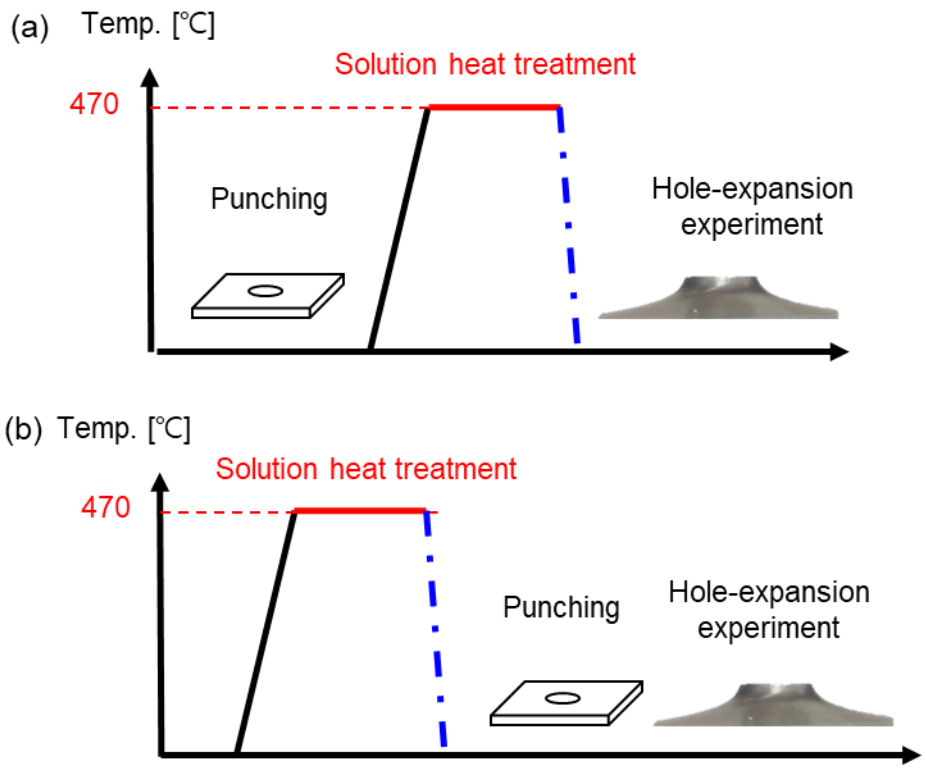

Figure 37. The HE experiment sequence of three steps using a punched specimen: (a) The original process, which is the sequence of the shearing process-SHT-HE experiment, and (b) the newly modified sequence with the SHT-shearing process-HE experiment

The HER value of W-SPH drops from 57%, which is the punching HER value of -W, to 42%, as shown in Fig. 38(d). The CLSM micrographs of the hole edge surfaces after the HE experiment for all three conditions in -W, are shown in Figs. 38(a)-(c) again. Fig. 38(c) evidently shows the sheared zone in the W-SPH condition specimen, which is unclear in the punching specimen.

To investigate the effects of SHT on a punched specimen microstructurally, the KAM map of the solid solution heat treated punched specimen is also evaluated through EBSD in the same manner as the punched hole under the T6 condition. The results are shown in Fig. 39 along with a KAM map of the punched specimen under the T6 condition, which is intended to compare the KAM map for the punched specimen of the two tempers. The KAM map of W-SPH also shows higher distortion due to deformation near the hole edge, but the distortion level is lower than that of the punched specimen of the T6 temper. The grain sizes of both tempers of both conditions are similar between 25 and 31 μm, and the application of only 15 minutes of solution heat treatment has a negligible influence on the grain size.

The HER results of W-SPH and punched specimens under the -W, surface images of the edge part, and KAM maps measured in CLSM showed that the deformation accumulated by hole fabrication through the shearing process is partially relieved by SHT, and as a consequence, wire HER and punching HER show similar results under the -W temper.

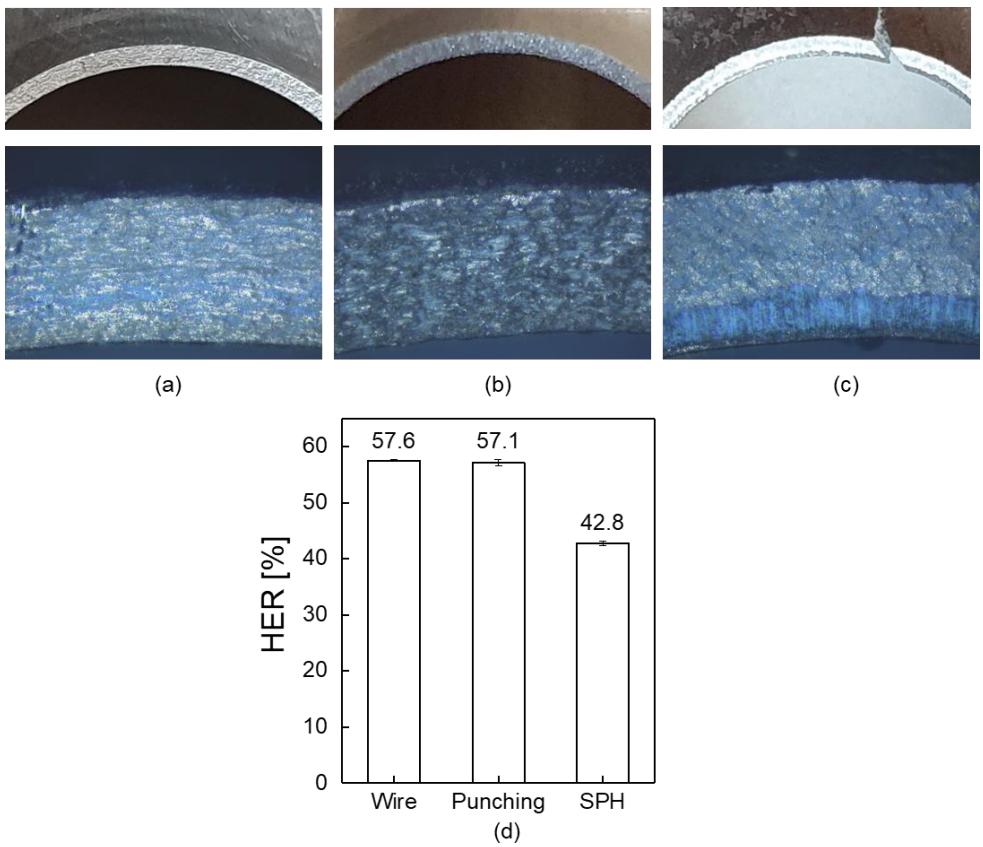

Figure 38. Comparison of results of conical HE experiments according to initial hole fabrication methods of W temper: CLSM micrographs of (a) punched specimen, (b) wire-cut specimen, and (c) W-SPH specimen and (d) the measured HER values

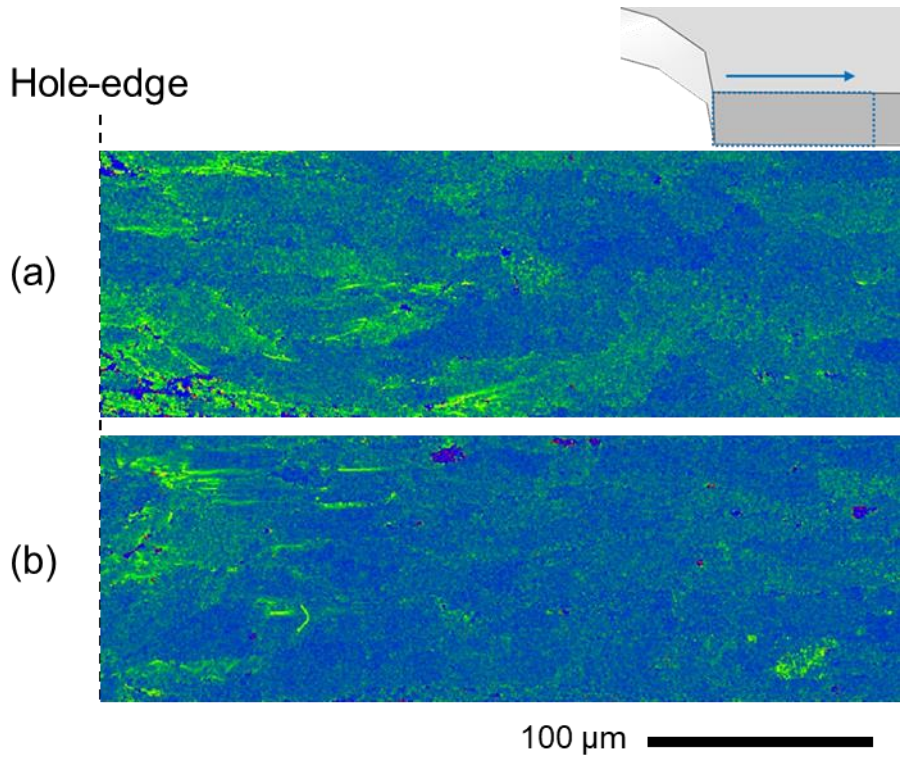

Figure 39. Comparison of the KAM maps: (a) punched specimen under T6 condition and (b) punched specimen followed by solid solution heat treatment

4.2.3.3 Comparison of the HER values of two tempers.

The overall HER results of -W are higher than those of T6 in both hole preparation methods. In the engineering stress-strain curve of the uniaxial tensile experiment and the punch force-displacement curve of the HE experiment, the -W temper shows longer elongation with lower stress; furthermore, the -W temper also represents improved formability, as mentioned in the previous chapter. However, the -W temper has a shorter post uniform elongation than the T6 temper. Since high strain sensitivity implies a delayed localized necking in the specimen [154–156], materials with high strain sensitivity generally exhibit long PUEL values. Since diffuse necking affects weakly and localized necking mainly governs failure in the HE experiment [125], higher strain rate sensitivity means higher uniform elongation and at the same time, a higher HER result value. T6 shows negligible strain sensitivity in the strain range from 10-2/s to 10-4/s at room temperature. The reason for the short post uniform elongation of -W is due to the PLC effect that causes early fracture [118] and exhibits negative strain sensitivity, as mentioned in several previous chapters. The sheet in the HE experiment suffers from a more complex deformation history than in the uniaxial tensile experiment because the hole edges are stretched circumferentially and simultaneously bent out of plane. Therefore, it is insufficient to use only the mechanical properties measured in the uniaxial tensile test as an indicator of the overall mechanical properties.

Since PUEL and delayed local necking are related to the ductility of the material, the microstructure is analyzed to understand the reason for the higher HER results of -W temper, instead of just using mechanical parameters. As shown in Fig. 40(a), the specimen of T6 temper showed that the fractured surface of the uniaxial tensile test is

almost perpendicular to the longitudinal direction of the specimen, while -W exhibits a fractured surface diagonally tilted in the longitudinal direction, indicating localized necking after diffusion necking. Figs. 40(b)-(d) show the fracture surfaces of the uniaxial tensile test specimens measured with SEM (SU-70) at various magnifications such as 120, 1000, and 3000, and these SEM micrographs clearly show a larger number of larger dimples in the -W property, which means that -W is more ductile than T6 [157].

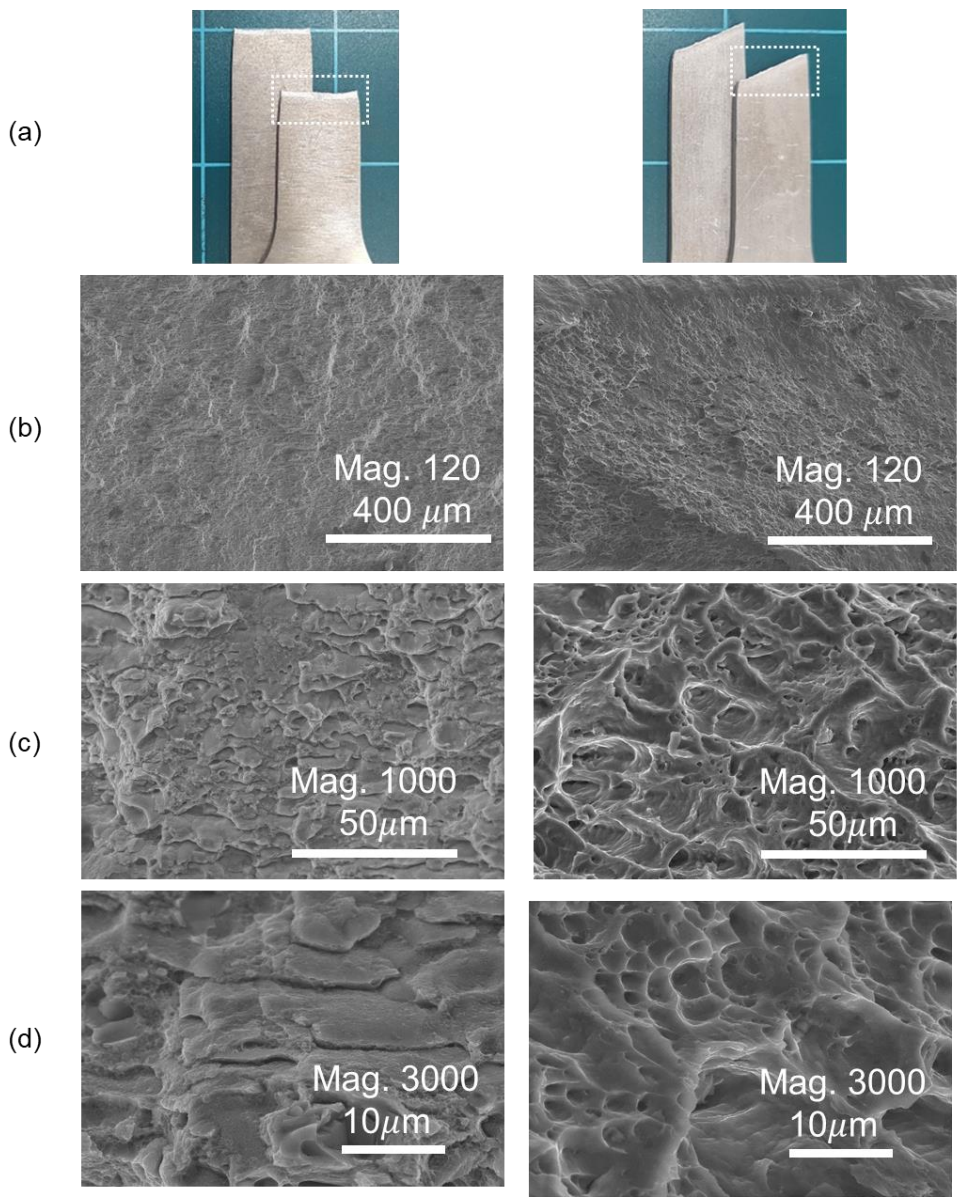

Figure 40. Fractured surface after completion of uniaxial tensile test: (a) whole specimen, SEM micrographs using various magnifications of (b)120, (c) 1000 and (d) 3000

The captured surfaces of the hole edge in the punched specimen of two tempers by CLSM, as shown in Fig. 41, are consistent with previous results. Because the purpose is to compare ductility through the width of the sheared zone generated during the shearing process, two punched specimens are compared: the W-SPH specimen, in which the hole is punched under the W temper, and the punched specimen of T6, in which the hole is punched under the T6 temper. The sheared zone ratios within the thickness of T6 and W-SPH are around 10% and 30%, respectively, which indicate that -W is more ductile than T6 [158].

Based on the cross-section shape and SEM images of fractured specimens from the uniaxial tensile experiment and HE experiment, it is determined that -W is more ductile than T6 despite the shorter post uniform elongation. Therefore, it is confirmed that PUEL is extremely short when the PLC effect is exhibited. Nevertheless, a high HER value is shown when the material exhibits ductility properties. Therefore, in the case of materials exhibiting the PLC effect, further study on the correlation between mechanical properties and HER results could show more reliable results considering the sudden fracture from the PLC effect due to negative strain sensitivity.

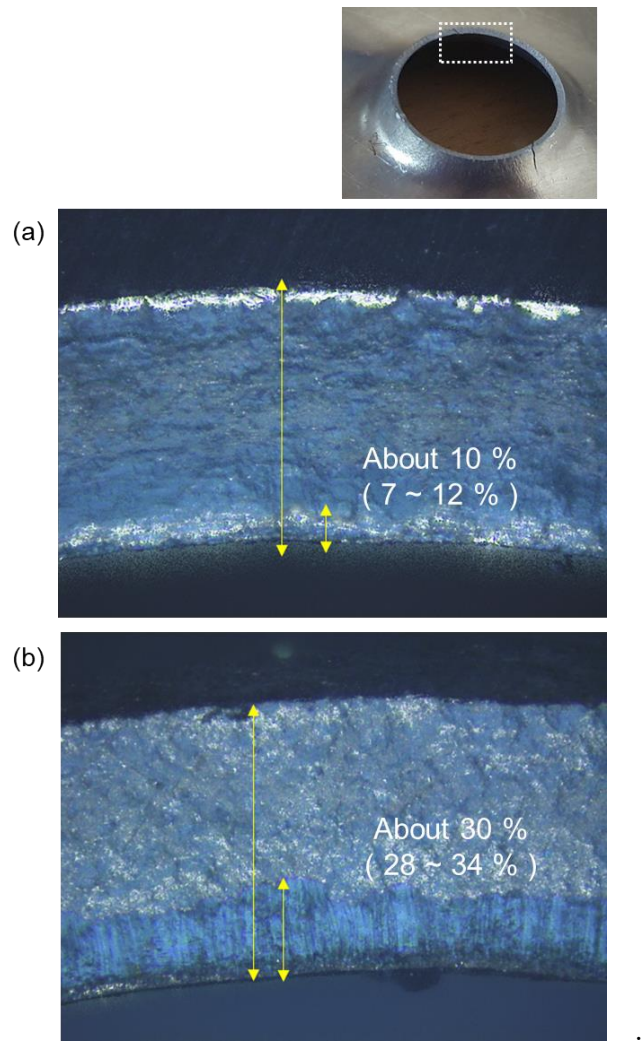

Figure 41. CLSM macrographs of the fractured surface after completing the uniaxial tensile experiment: (a) punched specimen perforated when the sheet is in the T6 state and (b) the W-SPH specimen, perforated when the sheet is under W temper

4.3 Hole-expansion using flat-headed punch

4.3.1 Introduction

As an evaluation method of edge-formability, hole-expansion (HE) (ISO 16630, 2009) using a conical punch has been widely used to understand the edge crack behavior. The HER values are evaluated again with using flat-headed punch since many research reported the HER values is changed based on punch geometry due to the different strain paths [134,160]. The conical punch shows uniaxial tensilte stress state, while the flat-headed punch shows plane strain paths. The different strain path and deformation path are main reason for different HER, which is calculated through finite element simulation and also measured by DIC [134,160]. The expansion of a circular hole in a thin sheet by a flat-headed punch, termed flat-headed hole-expansion (HE), displays various stress states from uniaxial tension at the hole edge to plane-strain tension and equibiaxial tension in the area away from the hole edge co-exist [160,161]. Aditionally, the most of the previous studies about PLC effects are mainly studied are done on the standard uniaxial tensile experiment [162,163], due to its simplicity; thus the findings may not be enough to understand the PLC effect comprehensively under complex deformation conditions, such as forming processes employing multi-axial stress states [164] . More recently, Coër et al. (2013) reported on the kinetics of PLC bands in simple shear from the DIC strain fields, which are found to be qualitatively similar to uniaxial tension. Mansouri et al. (2019) examined the hemispherical punch stretching, so called Erichsen formability experiment (ISO 20482:2013. Metallic materials—Sheet and Strip—Erichsen Cupping Test., 2013) [165], and observed two types of PLC bands, i.e.,

a full-circular one near the punch contract area and a linear one with a meridional, or radial propagation. In this chapter, the flat headed HE experiment is used to create a spatially inhomogeneous, multi-axial stress state in the deformation region [125,134,160], and to investigate the PLC effect under these conditions. The existence of PLC bands is observed with the aid of DIC, and their behavior and kinetics are characterized.

Beyond the formability evaluation, the HE experiment can be a great method to validate the material modeling, including plastic anisotropy. Since 1) larger deformation can be achieved than a standard uniaxial tension due to compatibility with the surrounding material and 2) the material is deformed under various stress states between uniaxial tension, plane-strain tension, and equibiaxial tension, from the hole edge and radially inland. Parmar & Mellor (1978) suggested an analytical model to calculate the stress and strain variation around the hole. Ha et al. (2020 and Korkolis et al. (2016) validated material models, in particular, anisotropic non-quadratic yield functions. Ha et al. (2020) applied uniaxial straining prior to the HE experiment to investigate anisotropic strain hardening effect. Cohen et al, (2009) and Kuwabara et al. (2011) investigate the role of orthotropic or more general yield function.

Hence, the formability of the -W temper is investigated and compared with -T6 temper through the HE experiment using flat-headed or flat-bottom punch, and the Portevin-Le Chatelier (PLC) effect displayed in flat headed hole-expansion experiment is additionally investigated in this section. Beyond HE, the experiments include the plastic anisotropy characterization of each temper, to calibrate constitutive models involving a non-quadratic anisotropic yield function (Yld2000-2d) and an isotropic hardening model (combined Swift-Voce). In parallel, finite element (FE) simulations

are performed and the results are compared with the experiments regarding global (force-displacement curve) and local (thickness strain variation around the hole) metrics. For -W temper, the result is analyzed with an extended discussion to the PLC effect and the PLC effect on a spatially-inhomogeneous stress field like HE experiment and analyze regarding formability aspect is also investigated.

4.3.2 Experimental procedure and results

The HE experiments are performed using a fully-instrumented, double-action hydraulic press as [170]. The machine has five hydraulic cylinders, i.e., four for the blankholder with a max. force of 112 kN each and one for the punch with 260 kN. Two types of sensors, i.e., a set of four piezocrystal load cells and a linear resistive transducer embedded in the punch cylinder, measure the punch force and displacement, respectively. The strain fields are obtained by 3D-DIC using two 2.0 MPixel digital cameras (GRAS-20S4M-C) and the VIC-Snap software from Correlated Solutions. The post-processing DIC parameters in VIC-3D for a subset, step, and filter sizes are 29 pixels, 1 pixels, and 5 to keep the strain resolution high and to avoid averaging out the strain variation in the hole expansion and 21 pixels, 5 pixels, and 15 for the uniaxial tension experiment. The bulge experiment is post-processed by ARAMIS using 19 pixels, 15 pixels, and 3 for facet, step, and filter sizes, respectively.

The actual machine with the equipment described above is shown in Fig. 42(a) and the specific dimensions of the tooling with a flat-headed, rounded punch are found in Fig. 42(b). It should be noted that a flat-headed, round punch is not a standard shape referred in (ISO 16630, 2009). This is because the objective of this study is not to investigate flangeability of a sheared hole, but to examine formability related to the plastic anisotropy under “in-plane stretch”. The punch face has a recess to avoid any contact with the deforming hole and eliminate frictional effects. Lock-bead is not used to restrain flow from the flange into the die cavity and because forming with the lock-bead is not successful for this material. Instead, an excessively high blankholding force is applied. The hole-expansion specimens are prepared by end-milling a hole of 35 mm

dia. An alignment jig is used to ensure that the hole is concentric with the punch before each experiment.

The punch face interfacing with the blank is lubricated using Drawsol diluted in water (water:oil=3:1) to reduce friction. Dry friction prevails between the blank and the rest of the tooling. The hole-expansion experiments are conducted at least three times to confirm the result. Both -T6 and -W tempers show good repeatability, as seen in Fig. 43(a) for the force-displacement. -W temper reach 1.3 times greater punch displacement than for -T6 temper, i.e., δ_{max}^{W}=17.7 mm and δ_{max}^{T6}=14 mm, but require 0.63 times lower forming force. This agrees well with the uniaxial tensile behavior of each temper (Fig. 2 and Fig. 9), as well. The increased cup height in -W vs. -T6 temper is also visible in the side view of Fig. 43(b).

The hole-expansion formability evaluated by hole-expansion ratio (λ) is calculated using equation (10). The d_i is measured before the experiment by a digital caliper, which is constantly 17.5 mm in this section, and d_f is determined by an average value of expanded hole diameters at the onset of fracture in three experiments using the coordinate information post-processed by VIC-3D instead of using digital caliper. The measured values for d_f show good repeatability with small standard deviation, i.e., St.d=0.4 and 1.3 mm, for -T6 and -W, respectively. The calculated λ for each tempers are respectively λ^{T6}=0.166 and λ^{W}=0.283, which indicates that the material in -W temper has 1.5 times greater hole-expansion formability than that in -T6 temper. This value almost coincides with the simple comparison based on the punch displacement up to rupture described above. Images of the expanded holes and the associated diameters are shown in Fig. 43(c).

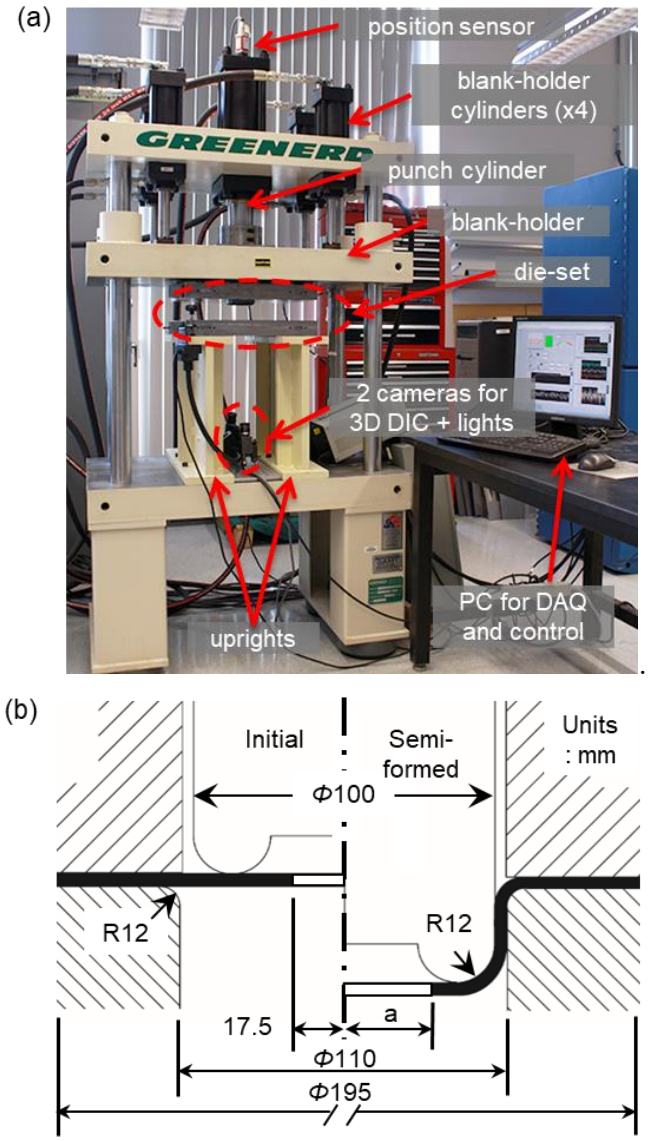

Figure 42. Experimental set-up for hole-expansion: (a) fully-instrumented, double-action hydraulic press with 3D-DIC and (b) specific dimension of tooling with a flat-headed punch [170]

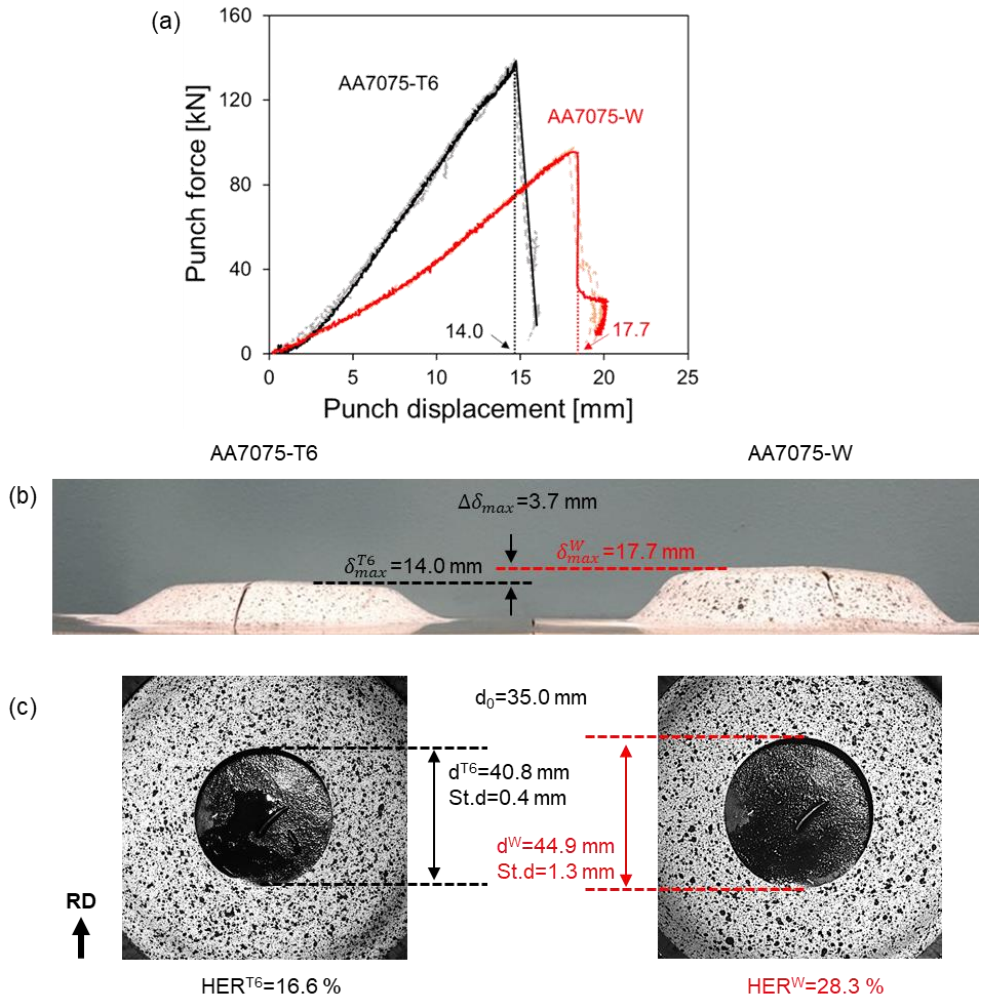

Figure 43. Comparison of hole-expansion experiment for T6 and AA7075-W: (a) punch force-displacement curves, (b) cup height, and (c) average expanded hole diameters in the RD of deformed specimens at the onset of fracture with standard deviations of three experiments. It should be noted that (b) is a side view of the fractured specimen unloaded from the machine as soon as the first rupture occurs and (c) is a front view from DIC at one frame before the fracture.

In addition to the comparison of structural responses, the thickness strain distribution around the hole is examined at the onset of rupture, as seen in Fig. 44. The average strain in absolute value is greater in -W temper than -T6 temper, which also represents superior formability. However, despite of the different achievable strain level, the local strain variation has a similar pattern for both tempers: the greatest thinning is observed along the RD (vertical direction) and the lowest along the ±45o from the RD. As a result, the first rupture is prone to occur in the RD for both tempers (marked by solid arrows in Fig. 44). It should be noted that rupture is observed in the TD in one out of four experiments in -T6 temper (marked by dashed arrows in Fig. 44). All -W temper specimens failed in the RD.

The same observation with Fig. 44 is made in Fig. 45 for the thickness strain variation around the circumference, along a hoop of 20 mm initial radius which is 2.5 mm inland from the hole to avoid possible loss of DIC correlation at the edge. The thickness strain evolution is presented at five different relative punch displacements (δ) up to rupture (δ_{max}), i.e., 0.5, 0.65, 0.8, 0.9, and 1 δ/δ_{max}. One experiment from each temper is plotted; however, at the onset of rupture, i.e., $\delta/\delta_{max} = 1$, all experiments are included, to compare the test-to-test variation. These results agree reasonably well to each other, confirming the repeatability of the experiments (see also Fig. 43(a)). The average thickness strains at the onset of rupture are respectively -0.099 and -0.144 for -T6 and -W tempers. Both are greater than the max. thickness strain at the onset of rupture during uniaxial tension, i.e., -0.084 and -0.111. This confirms that the hole-expansion experiment enables larger plastic deformation than uniaxial tension using a standard specimen, even though the material near the hole edge is also subjected to almost uniaxial tension along the hole circumference, as reported earlier from Ha et al. (2020)

and Kuwabara et al. (2011).

Like in Fig. 44, the max. thinning in Fig. 45 is mostly observed in the RD, i.e., 180o, (except one experiment for -T6 temper with the max. thinning in the TD). As a result, the RD is the most favored direction for the first rupture in both tempers. In contrast, 45o direction always exhibits the least thinning regardless of temper. This indicates that the anisotropy, as measured by the uniaxial tension experiment, i.e., r-value, is not significantly altered by this specific heat-treatment, i.e., SHT and water-quenching. (This will be addressed further in the next Section.) One noticeable difference between the two tempers is the smaller difference of min. and max. thickness strains in the RD and TD. This difference is identified by a light-orange band in Fig. 45. It is possibly related to PLC activity observed in -W temper but not in -T6 temper samples. This will be further discussed later in detail.

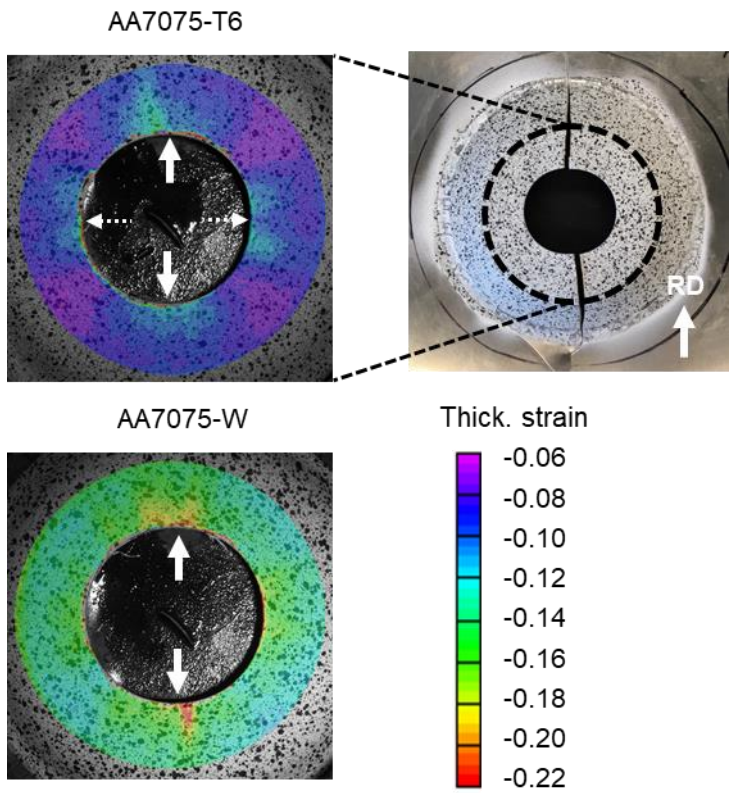

Figure 44. Thickness strain variation onset of fracture of T6 and AA7075-W

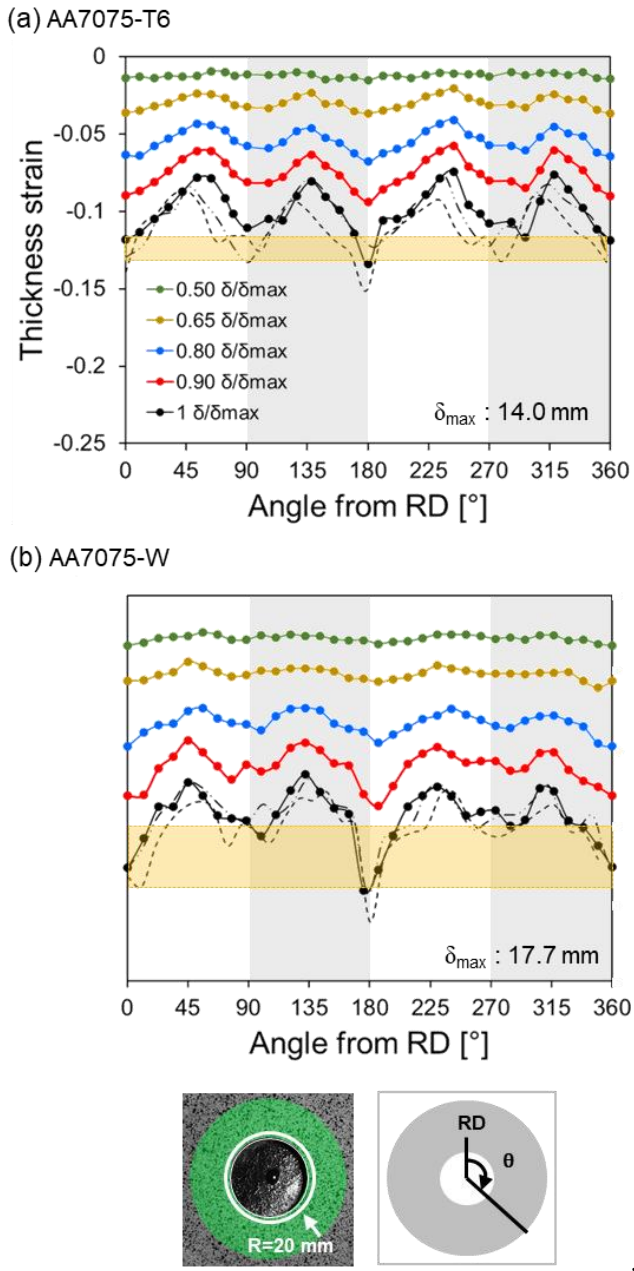

Figure 45. Evolution of thickness strain variation around the hole for (a) T6 and (b) AA7075-W

4.3.3 Material modeling and Numerical simulation

4.3.3.1 Material modeling

The material behavior in both tempers, i.e., T6 and AA7075-W, is modeled based on the experiments presented in chapter 3. The true stress and true plastic strain relationships for both tempers are obtained from the uniaxial tension experiments and used to extrapolate the strain hardening behavior beyond the limit of uniform deformation in uniaxial tension. In order to capture different hardening features in both tempers, such as saturation-type hardening in T6 and large ratio between yield and ultimate tensile stresses in AA7075-W, using the same type of model, a combined Swift-Voce hardening is used as suggested by Eller et al. (2016) and Roth & Mohr (2014) as shown below in Eq. (12):

$$\bar{\sigma} = \omega_a \cdot \mathrm{K}(\bar{\varepsilon} + \varepsilon_0)^{\mathrm{n}} + (1 - \omega_a) \cdot \left\{\sigma_{\mathrm{s}} - \left(\sigma_{\mathrm{s}} - \sigma_{\mathrm{y}}\right)\exp(-\bar{\varepsilon}/\mathrm{c})\right\} \quad (12)$$

Plastic flow is described similarly to the previous chapters 3 by a non-quadratic anisotropic yield function (Yld2000-2d) incorporating a rate-independent, associated flow rule. 8 experimental data from uniaxial and equibiaxial tension (summarized in Table 10) are utilized for the parameter calibration of Yld2000-2d (α_(i,i=1~8)). In the HE experiment, considering the deformation range of measured thickness within an area of interest, normalized stress and the biaxial ratio between RD/TD are calculated again for capturing the material behavior more in detail. Newton-Raphson optimization method is adopted due to its robustness. The resulting parameters are presented in Table 11 for each temper.

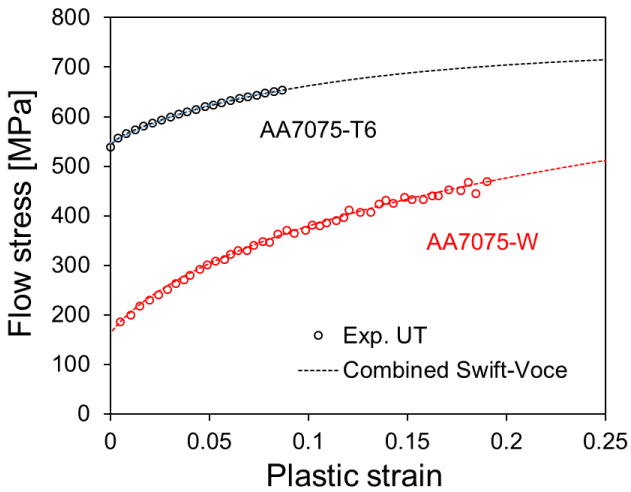

Figure 46. Extrapolation of flow stress-strain curves using combined Swift-Voce model for AA7076-T6 and AA7075-W

Table 10. Summary of the experiments used for Yld2000-2d parameter calibration

	Normalized stress				r-value			
Direction	UT (RD)	UT (DD)	UT (TD)	BB	UT (RD)	UT (DD)	UT (TD)	BB
T6	1	0.978	1.006	1.045	0.53	1.12	0.69	0.99
AA7075-W	1	0.973	1.004	1.045	0.54	1.02	0.67	0.99

Table 11 Anisotropy parameters for Yld2000-2d (m=8)

	α_1	α_2	α_3	α_4	α_5	α_6	α_7	α_8
T6	0.886	1.002	0.903	0.990	1.001	0.857	1.021	1.090
AA7075-W	0.896	0.993	0.897	0.992	1.000	0.860	0.018	1.117

Figure 47(a) represents the normalized stresses and r-values of the uniaxial tension experiments and the predictions of Yld2000-2d. It shows that for both tempers the anisotropy is very similar and, as typical for aluminum alloys, the r-values exhibit stronger anisotropy than the flow stresses. The plane-stress yield loci for both tempers are shown in Fig. 47(b), along with the in-plane experimental data, i.e., RD and TD uniaxial tension, and equibiaxial tension. The yield loci of Yld2000-2d for both tempers show very similar shapes due to the similar anisotropy properties. This indicates that, while the SHT changes the flow stress and ductility of AA7075, it does not markedly affect its plastic anisotropy as reported by Leacock et al. (2013).

Cullen and Korkolis (2013) observed deformation-induced heating and strain-rate effects are neglected, as is typical for aluminum alloys under such conditions and it is also verified by Knysh and Korkolis (2015).

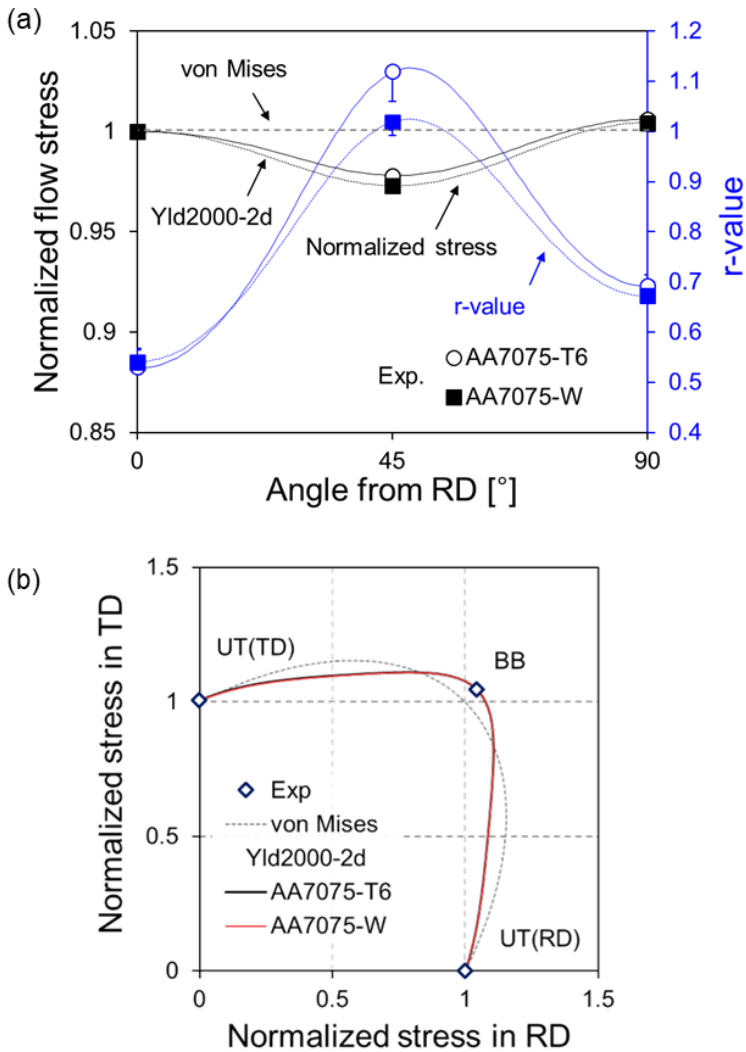

Figure 47. (a) Anisotropy in yield stress and r-value in uniaxial tension at RD, DD, and TD and prediction of Yld2000-2d and (b) yield loci of T6, AA7075-W, and von Mises

4.3.3.2 Numerical model

The HE simulation is conducted using the commercial FE software Abaqus/Standard version 6.12 (implicit solver) [171] with a user-defined material subroutine (UMAT) for the constitutive models, i.e., Yld2000-2d yield function and combined Swift-Voce hardening model. The FE model for HE is built as a quarter of the problem, considering two-fold symmetry, as shown in Fig. 48(a).

All components of the tooling, i.e., punch, blankholder and die, are created by non-deformable, analytical rigid body elements. The blank is constructed as a deformable body using 4-node shell elements with reduced integration (S4R) and hourglass control. Based on the sensitivity test performed, 9 integration points are assigned in the through-thickness direction referring as Lee et al. (2019) implemented. The mesh of the blank is given in Fig. 48(b) and is designed to reduce the computational time. In consideration of the amount of deformation subjected to the blank, it is divided into three sections from the hole outwards: I) hole periphery, where the deformation mainly occurs, II) the region between the contact with the punch and the section clamped by the blankholder, and III) the clamped section. The mesh sizes are determined in an increasing order as 1.0, 2.0, and 2.5 mm, respectively, through a mesh sensitivity study. The locations of first contact of the blank with the punch (red solid line) and the die (yellow solid line) are marked in Fig. 48(b) at 38 mm and 67 mm from the center (i.e., at diameters of 76 mm and 134 mm, also see Fig. 42(b)), respectively, to help with visual understanding. Along the circumferential direction, 60 elements are assigned to the quarter geometry, i.e., each of them is occupying a 1.5° arc.

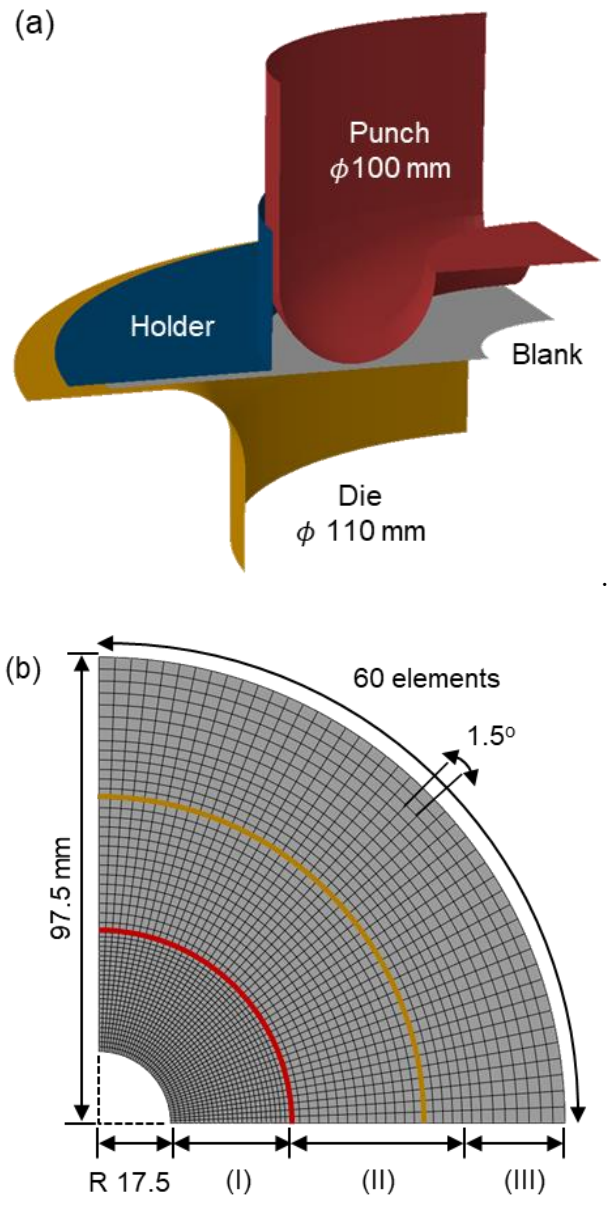

Figure 48. (a) Isometric view of finite element model in quarter size for hole-expansion and (b) planar view of blank mesh. The red line indicates the contact with the punch and the orange line the contact with die radius. Regions of different mesh densities are identified with I, II and III.

Surface-to-surface contact is assumed between the blank and other interfaces of the tools. Taking the different lubrication conditions of the interfaces into account, a Coulomb friction coefficient of μ=0.2 is applied between blank and punch and μ=0.65 between blank, die and blankholder, to ensure that no flow occurs there. A 80 kN constant blankholding force is applied to the interface of blank and blankholder in the quarter model. In contrast to standard deep-drawing practice, the total blankholding force (320 kN) is 2.5-4 times higher than the maximum punch force (shown in Fig. 43(a)), to ensure that no material is drawn-in from the flange to the die cavity during HE. However, where a usual blank would tear during drawing under such conditions, the result of this constraint here is to instead force the bottom of the cup to stretch, expanding the hole that is located there. No other, displacement-based constraints are applied to the blank.

4.3.3.3 Comparison of the experiments and predictions

The punch force-displacement curves (Fig. 49(a)) and thickness strain variation along the circumferential direction (Figs. 49(b)-(c)) from the HE experiments of both tempers presented before are now compared with the results of FE simulations. The force-displacement curve, which represents the structural behavior of the material, is well predicted by the constitutive and numerical models used for the simulation.

The predicted thickness strain variation along the circumference is extracted at the same punch displacements as the experiment. The results show reasonable agreement in terms of average strain level and variation pattern. On the other hand, the prediction generally underestimates the max. thinning and as a result of that, the difference between the max. and min. thinning at either RD or TD and DD, respectively, is smaller than the experiment. This is possibly caused by insufficient information to calibrate the hardening model using the uniaxial tension stress-strain curve, since the strain in HE can reac9h to a higher level than in the standard uniaxial tension. In an earlier work (Ha et al. (2020), the authors have identified the hardening model using the post-necking work-balance in uniaxial tension. As an alternative, experiments such as simple shear can be used to obtain the stress-strain curve for large deformations (Coër et al. (2013) and Rahmaan et al. (2020)). Abedini et al. (2020) extended the approach using shear strain and obtained hardening responses for general anisotropic materials. Any of these could be a great option to consider as future work, to improve the predictions.

Regarding the max. thinning, which results in the first rupture, the prediction for -T6 temper shows similar thickness strain levels in RD and TD, which correlates well with the experimental observation, i.e., first rupture in either of these locations.

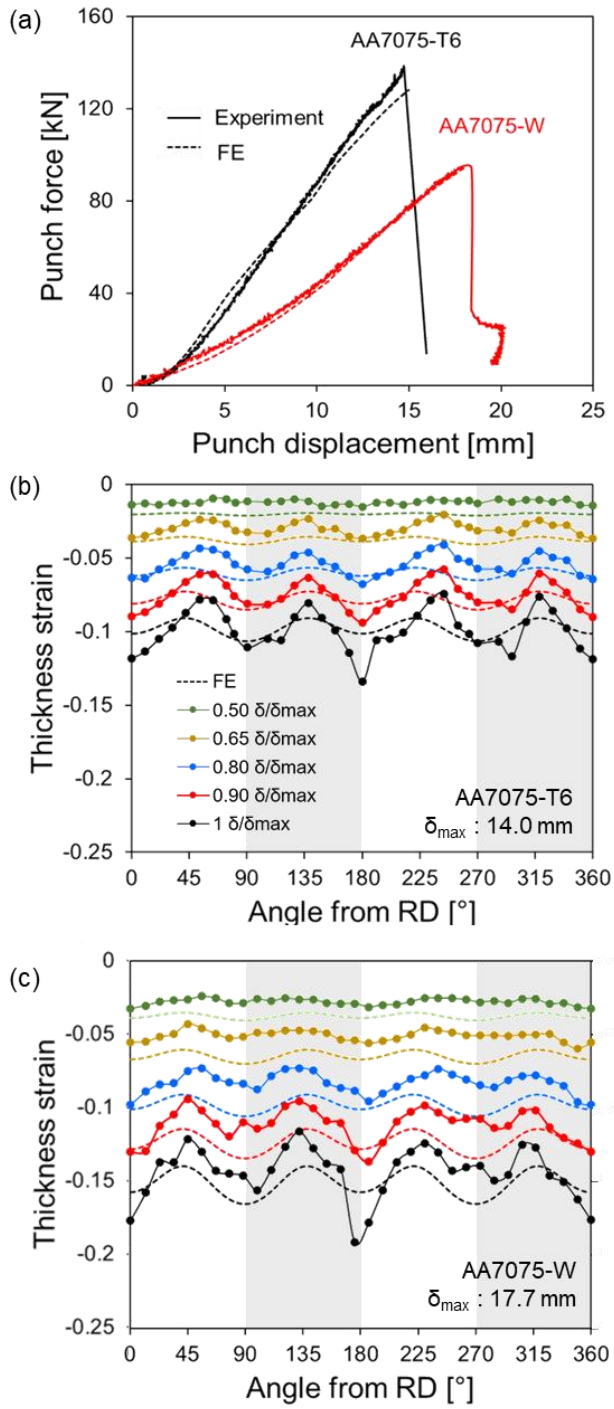

Figure 49. Comparison of experiment and simulation for hole-expansion: (a) punch force-displacement curves and evolution of thickness strain variation along the hole periphery of (b) T6 and (c) W

However, for -W temper, although the overall prediction is good, the features related to the max. thinning, e.g., location and strain level, are not correctly predicted. This discrepancy may be caused by neglecting the PLC effect in the material modeling for -W temper, due to which the FE simulation cannot capture any influences of the PLC bands on the strain distribution. This will be further discussed in the next section.

4.3.4 Discussion

The fact that the experiments and the FE prediction for -T6 and -W tempers are generally in good agreement (see Fig. 49) indicates that the constitutive models implemented in the simulation work reasonably well. The overall structural response (see Fig. 49(a)) is captured very well, which is somewhat expected as it is typically not very sensitive to the plastic anisotropy. This is also demonstrated earlier in a variety of other problems from Korkolis and Kyriakides (2011b), Giagmouris et al. (2010) and Ha et al. (2018). Furthermore, the plastic anisotropy for -T6 and -W tempers is described in a similar way, which produces similar predictions for the thickness strain variations. However, the PLC effect, which only appears in the -W temper samples, is not considered in the material modeling. As a result of that, the thinning profile in -W temper is not as well predicted as in -T6. In this section, a detailed analysis about the PLC banding and its effect on the strain redistribution during the HE experiment is presented.

The first observation is made on the circumferential strain distributions measured in the experiments, as shown in Fig. 50. Higher circumferential strain is observed along the RD in both -T6 and -W tempers, but the difference between the RD and TD is much more significant in -W temper. While the PLC effect on the strain variation is not clearly shown in Fig. 45b, a close-up of the thickness strain variation, marked as a red arc of ± 4 mm (± 10 º) and spanning the first rupture in RD, shows that the strain evolution in the -W is distinctly different from the one in the -T6 temper (Fig. 50).

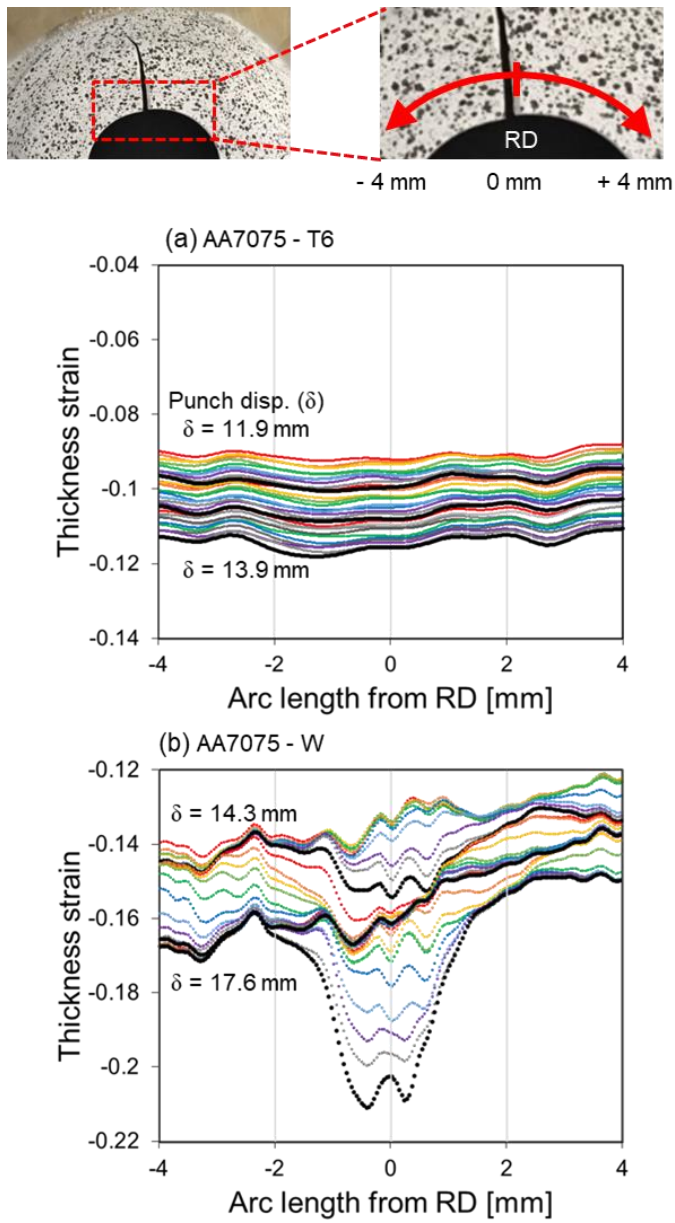

Figure 50. Evolution of thickness strain variation within ± 4 mm arc from the RD during the last 30 steps before fracture of (a) T6 and (b) AA7075-W

The data is plotted for the last 30 steps preceding the onset of rupture. The punch displacement range during these 30 steps is included in each figure, while every 10 steps are represented with the same color set from red to black. In Fig. 50(a), the thickness strain evolution of -T6 temper is displayed, in which the strain evolution is fairly proportional between each step. It can be noticed that the neighborhood of RD shows higher thinning rates than its surroundings, which is eventually leading to the max. thinning appearing there. In contrast, in Fig. 50(b), the local strains in -W temper evolve irregularly, with the max. thinning locations shifting until failure occurs.

This non-uniform strain evolution in -W temper is clearly observed in a wider range of view, i.e., an arc of ± 90° from the RD (Fig. 51). That plot includes 10 steps of thickness strain evolution at nearly 90% of max. punch displacement (from 15.5 mm to 16.3 mm, when max. is 17.7 mm). This non-uniform, inhomogeneous strain evolution pattern is a definite evidence of the PLC effect by previous researches such as Neuhäuser et al. (2004) and Reyne et al. (2019), indicating that such PLC activity is affecting the strain distribution together with the plastic anisotropy during the HE experiment. In this regard, the thickness strain variation is considered to be governed by different mechanisms in each temper: for -T6 temper, it is mainly attributed to the plastic anisotropy of the material, while for -W it is due to a combination of plastic anisotropy and PLC effect. This explains the observation of the greater strain difference between the RD and TD in -W temper (Figs. 49(c) and 50) compared to -T6 temper.

Other researches investigated this strain pattern as one of the experimental observation about PLC effect with DSA mechanism [22,180,181]. The propagation of the PLC bands during hole-expansion is seen in Fig. 52. The circumferential strain and strain-rate near θ=180° (in the counter-clockwise direction, assuming the origin to be

along the rolling direction (RD)) are closely monitored during punch displacements δ from 13.1 mm to 13.4 mm (or δ/δ_{max} from 0.74 to 0.76), for five frames named as I to V.

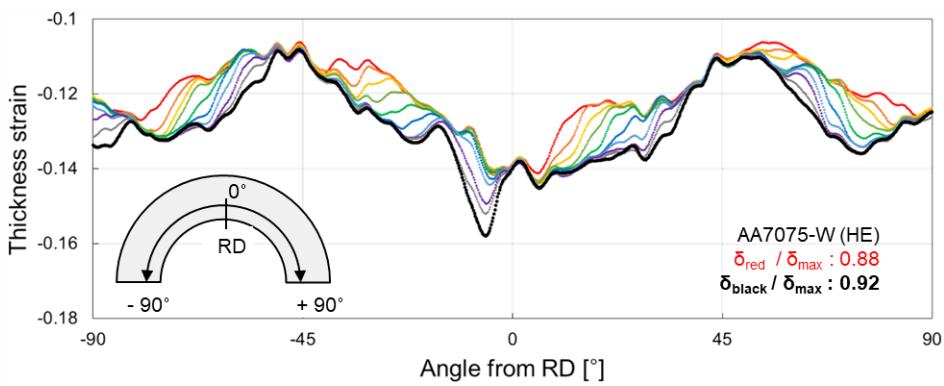

Figure 51. Evolution of thickness strain variation within ± 90° from the RD (wider view of Fig. 50(b)) of AA7075-W

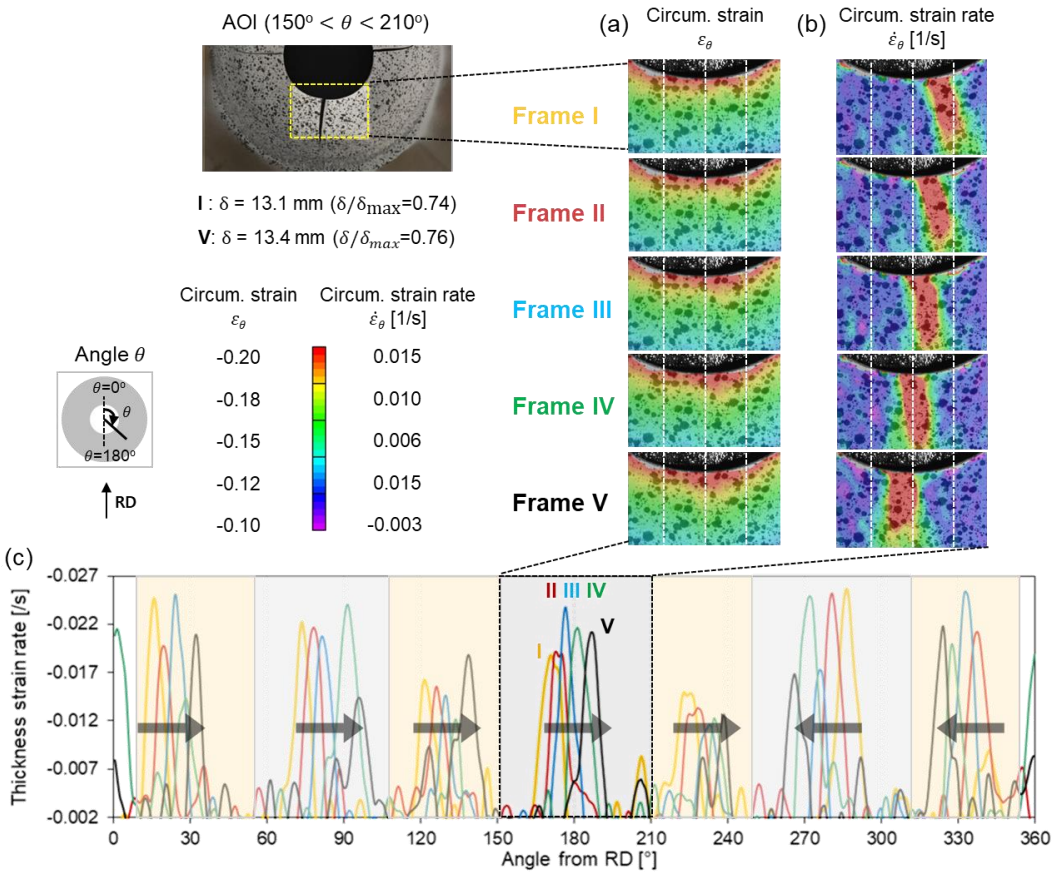

Figure 52. Propagation of PLC bands: close-up of (a) circumferential strain and (b) circumferential strain-rate fields, and (c) thickness strain-rate along the hole for 360° during δ = 13.1 (Frame I) to 13.4 (Frame V) mm

In Fig. 52(b), one particular PLC band, moving along the circumferential direction, is traced during δ from 13.1 (Frame I) to 13.4 (Frame V) mm, equivalent to δ/δ_{max} from 0.74 to 0.76. But multiple PLC bands have appeared simultaneously in different locations of the hole periphery, as in Fig. 52(c) which is the thickness strain-rate for 360° along the hole, measured at 2.5 mm inland from the hole edge to avoid the lost DIC correlation there. (The black box in Fig. 52(c) presents the location corresponding to Figs. 52(a) and 52(b)) Each time frame is presented in the same color, from yellow (Frame I) to black (Frame V) solid lines. Counting peaks with strain-rate higher than a threshold ($|\dot{\varepsilon}| > 10^{-2}$ /s), total seven active, coexisting PLC bands are identified in the hole periphery during this range of punch displacements. The direction of their propagation is characterized based on the translation of the peaks (see black arrows in Fig. 52(c)). Although the figure shows the activity of PLC bands during the specified range (δ/δ_{max}=0.74 to 0.76), the same motion of the PLC bands (i.e., translation along the circumferential direction) is consistently observed during the entire plastic deformation process. It should be noted that no consistent tendency of the propagation direction (e.g., clockwise vs. counter-clockwise) is observed. Furthermore, in contrast to uniaxial tension, the appearance of single PLC band is over various stress states (uniaxial to plane-strain and equibiaxial tension) in the radial direction. This is a distinct observation of the PLC bands under multiaxial stress states, produced in the hole-expansion, compared to the hydraulic bulge test [27].

The PLC activity, identified by the strain-rate as seen in Figs. 52(b) and 52(c), is examined for each step during the entire deformation up to the fracture. This is to understand further behavior of PLC band during the hole-expansion experiment, such as appearance of a new PLC band (nucleation) and disappearance of existing one

(dissipation), as well as the relationship to plastic anisotropy.

While the PLC bands in the uniaxial tension experiment can move out and disappear from the gauge region, in hole-expansion they are confined along the circumferential direction. This means that the life of a particular PLC band can be tracked from its nucleation to dissipation, see Fig. 53(a). A particular PLC band is monitored using a few frames before the nucleation and after the dissipation, while δ=11.19 to 15.61 mm (or δ/δ_{max} from 0.63 to 0.88).

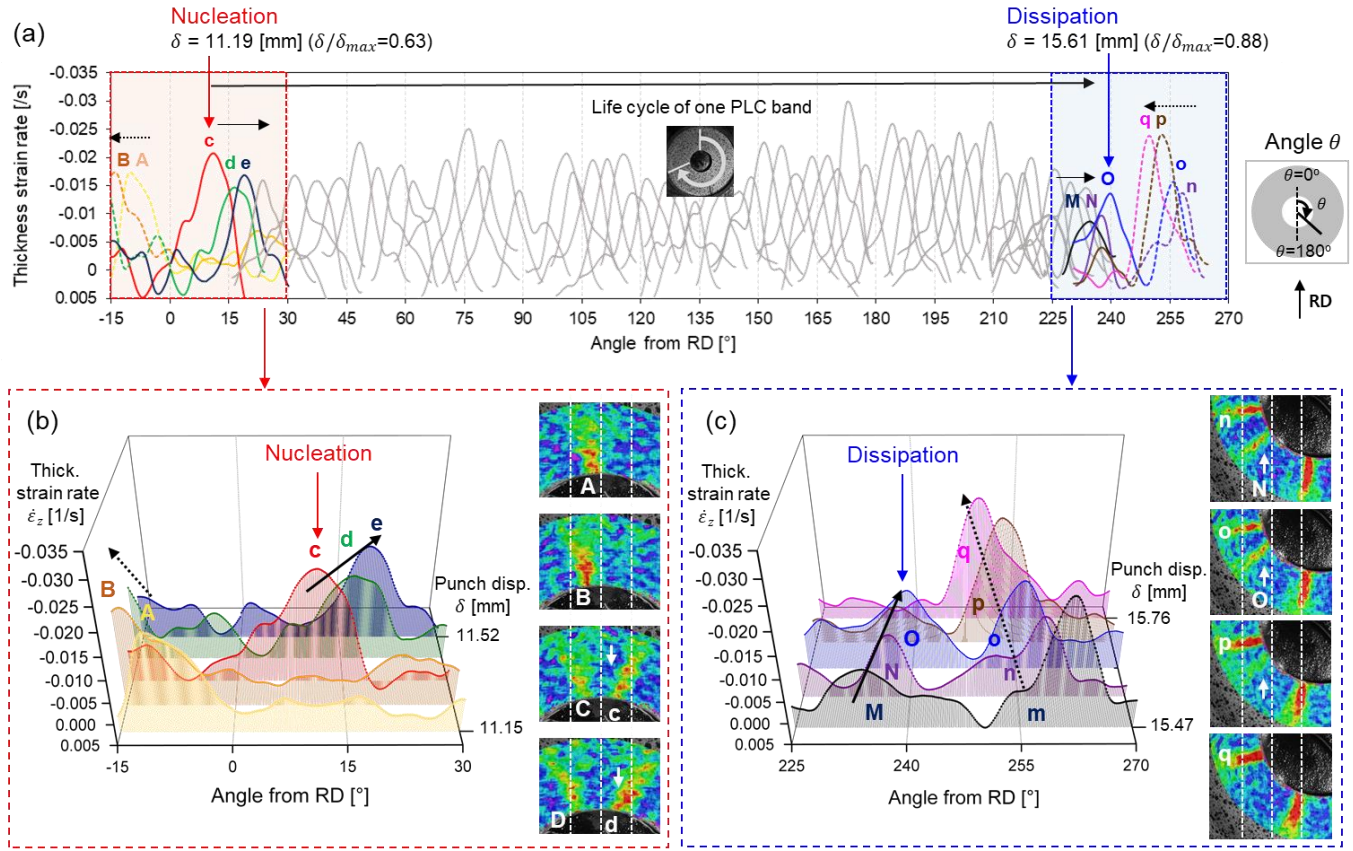

Figure 53. PLC bands from nucleation to dissipation: (a) life span of one particular band from δ=11.19 to 15.61 mm and (b) close-up of nucleation and (c) dissipation in 3D view observed in the thickness strain-rate fields

First, the nucleation of a PLC band near $\theta \approx 10^{o}$ is described in Fig. 53(b), i.e., a peak without interactions with neighboring PLC bands. Looking at the thickness strain-rate field (Figs. 53(a) and 53(b)), one PLC band suddenly appears in Frame c and starts displacing clockwise independently of the other bands. In Fig. 53(a), tracking of this PLC band is shown from its nucleation (red solid line) and translation (grey solid lines) till dissipation (blue solid line). The nucleation is shown Fig. 53(b) in more detail as a 3D view with respect to the progress of δ: the thickness strain-rate increases locally as a peak at Frame c (red solid line) and translates progressively from Frame c to e. The band travels almost $\Delta\theta$ =230^{o} from the initial location, but eventually disappears when it encounters another PLC band moving in the opposite direction at Frame O (Figs. 53(a) and 53(c)). It can be concluded that except the case when a PLC band disappears naturally, it will keep moving until it collides with another PLC band traveling in the opposite direction.

Based on the same method to observe new band as described before, the total number of new PLC bands until fracture is counted from the whole area divided into 8 sections based on the orientation; i.e., two in the vertical (rolling direction, RD), two in the horizontal (transverse direction, TD), and four in the diagonal (DD) directions (Fig. 54(a)). Since the sections in the DD occupy double the area compared to the other directions, the counted number of nucleation sites is normalized by the number of occupying sections, when examining the orientation effect on the PLC nucleation. The results of three repeated experiments are summarized in Table 12. Figure 54(b) represents the strain distribution when the punch displacement δ is 16.71 mm (δ/δ_{max} = 0.94) and Fig. 54(c) shows the evolution of deformation on RD region during the deformation about the thickness strain variation along the hole [90]. Although each

experiment performed exhibits some variation of the count, the sections along the RD are consistently the most favored region for the nucleation of new PLC bands, and DD are the least. At the same time, the RD region shows large deformation in thickness strain as shown in Figs. 54(b) and 54(c). This strain variation in the hole periphery is caused by plastic anisotropy. The figure shows that the maximum thinning is observed along the RD; the least thinning is along the DD. These results correspond to the findings for the PLC nucleation sites in Table 12. This correlation indicates a positive relationship between the nucleation of PLC bands and the equivalent plastic strain [90,181], which varies along the circumference due to the plastic anisotropy. In particular, the strain difference in the RD and TD caused by the plastic anisotropy is amplified due to the PLC bands, see Figs. 3 and 55. Figure 55(a) shows that the stress-drop observed in the uniaxial tension experiments is proportional to the plastic strain. Thus, the rupture in HE may occur in RD, where the strain is higher, due to the larger associated stress-drop than TD. In this regard, in the HE experiment (Fig. 55(b)), the greater strain increment in the RD step-like strain evolution implies that the material in the RD will experience sudden stress drops more often than the other locations, which makes the RD location dominantly prone to failure. For comparison, included in Fig. 55(b) are also the results of the -T6 temper, which show a smooth increase of the strain values, in contrast to the step-like increase seen for the -W temper.

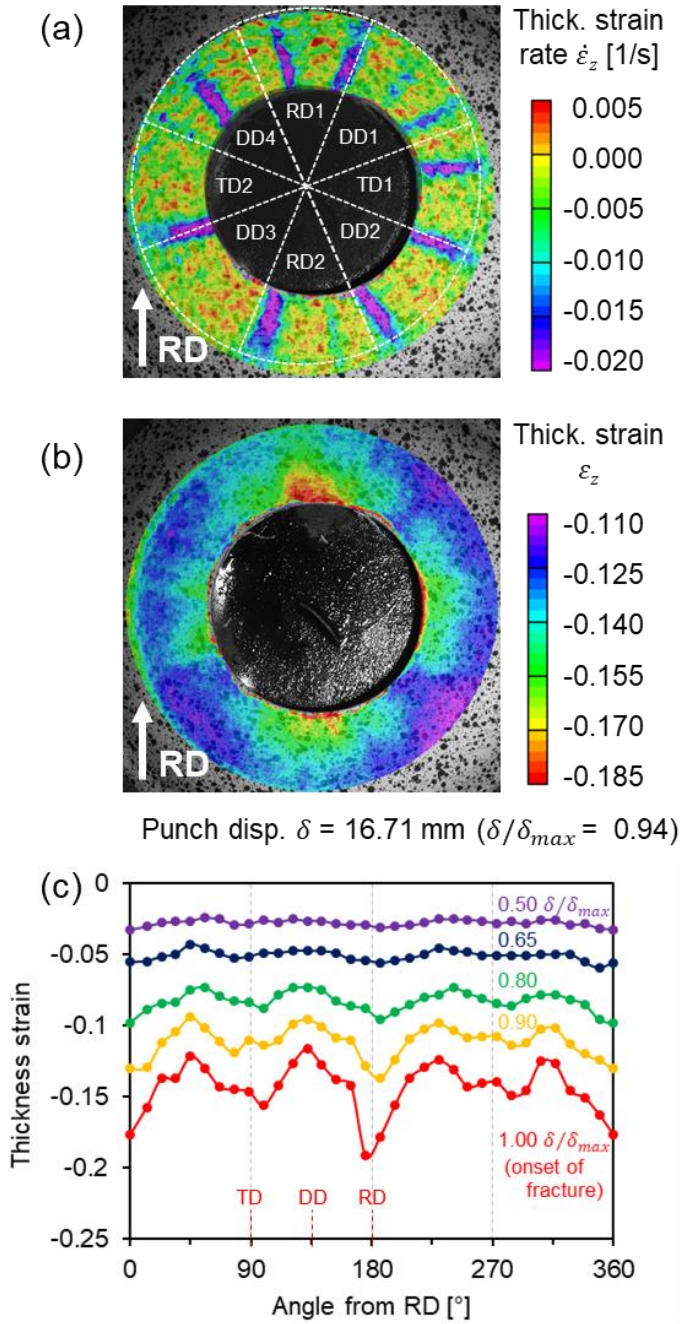

Figure 54. Effect of plastic anisotropy on the nucleation site for PLC band: (a) area division along the material orientation and PLC bands observed in the thickness strain-rate field, (b) thickness strain variation caused by plastic anisotropy at δ = 16.71 mm, and (c) thickness strain evolution along the hole [90]

Table 12. Count of nucleation sites with respect to the material orientation

Experiment	RD	DD	TD
Test 1	9	2	6
Test 2	15	2	3
Test 3	13	2.5	3

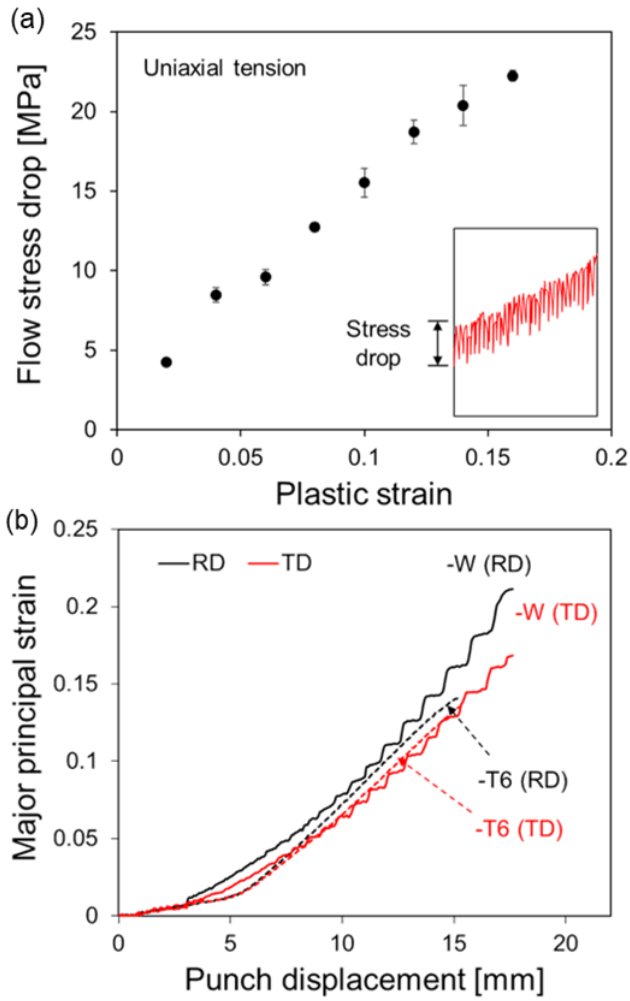

Figure 55. (a) Amplitude in stress serration (flow stress drop) measured from uniaxial tension and (b) evolution of major principal strain during hole-expansion measured at RD and TD

4.4 Remarks

This study investigated the effects of -W tempering on the formability of an AA7075 sheet in hole expansion. The HE experiments are conducted using a conical punch and flat-headed punch to evaluate the HER values based on the diameter between before and after the experiment.

In the conical HE experimental results, OM, SEM, EBSD, and CLSM micrographs are used to investigate the surface of the hole edge or properties of thickness near the hole. Based on the conical HE experimental results, the following conclusions can be drawn:

- To investigate the edge crack behavior or stretch-flangeability through the HE experiment using the conical punch, two hole edge conditions are compared, punching (shearing) and wire EDM.
- In T6 temper, the specimen with a hole fabricated by the shearing process shows lower HER values than the specimen with a hole fabricated by wire EDM because of deformation during the hole preparation process. The OM and SEM micrographs show clear differences in the cross-section of the hole edge. Furthermore, the KAM maps within thickness near the hole in both edge conditions show the accumulated deformation applied by the shearing process.
- In W temper, the HER results are almost similar between the two edge conditions because the SHT alleviates the deformation made by punching. Even though the punching process is conducted after SHT, the HER value of W is higher than that of T6 with the same edge condition.
- Overall, the W temper shows higher HER values than that of T6 in both edge

conditions. The W temper has longer elongation and is more ductile than T6, even though the W temper has shorter post uniform elongation from negative strain rate sensitivity.

For HE experiment using flat-headed punch, the strain evolution on the specimen surface is measured using the 3D-DIC technique. A combined Swift-Voce hardening law and non-quadratic anisotropic yield function Yld2000-2d are implemented in the FE simulation. The major findings of this HE study using flat-headed punch are:

- In the HE experiments, the average strains at the onset of the first rupture are higher than in the uniaxial tension test, even though uniaxial tension prevails at the hole edge. Similar to the uniaxial tension case, the material in -W temper reaches a higher punch displacement with a lower punch force than the -T6. As a result, the overall thickness strain (average and max.-min.) is greater in -W temper and the hole is expanded by 70% more than in -T6. This indicates that -W temper is beneficial from a formability point of view.
- Comparing the experiments to the FE predictions, the force-displacement and average thickness strain evolution throughout the HE experiments show good agreement for both tempers. This is despite the fact that the constitutive modeling of AA7075-W does not contain the PLC effect.
- Appearance of the PLC band in the hole-expansion experiment is along the radial direction from the hole center. As a result of that, the individual PLC band spans diverse stress states as the radial distance increases. The PLC activity is clearly observed in the thickness strain-rate field. The instantaneous strain-rate of an active

PLC band is almost an order of magnitude higher than neighboring regions outside of the PLC.

- The PLC bands propagate along the circumferential direction, which is almost perpendicular to the band alignment, instead of spreading out in a spiral shape. The bands can propagate either clockwise or counter-clockwise. The life of an individual PLC band, from nucleation to dissipation, is traced by the DIC analysis during the hole-expansion. A nucleated PLC band continues to propagate until it dissipates by an interaction with another band, traveling in the opposite direction. In such a case, two individual bands approaching from the opposite directions collide; one PLC band disappears and the other keeps moving in its original direction.
- The plastic anisotropy plays a major role in determining the thickness strain variation in -T6 temper. However, despite both -T6 and -W tempers showing similar anisotropy, the -W temper presents different thickness strain variation from -T6, due to the PLC effect. The greater strain that develops in the RD due to the plastic anisotropy can cause a larger number of PLC band nucleation sites near the RD, compared to other material orientations such as DD and TD. This indicates that the strain variation around the hole periphery that is caused by plastic anisotropy affects the nucleation of PLC bands.

Based on these findings, it can be concluded that The W temper shows longer HER values than T6 temper in both hole preparation edge conditions. The W temper has more ductile material properties, even though it has shorter post uniform elongation than T6 because of negative strain rate sensitivity. Also, the W temper could obtain larger HER values when SHT alleviates the partial deformation applied by punching.

The constitutive and numerical framework used in the study using a flat-headed punch can be used for a preliminary, virtual design of a forming process in a computationally efficient way. The major purpose of that preliminary step is to evaluate anisotropic deformation and formability due to localization of Al alloy sheets under different tempers. Once this is completed and the process design space is narrowed down, a more detailed study to include the PLC effect and associated inhomogeneous deformation characteristics is warranted, either experimentally or with more advanced constitutive models.

5. Conclusion

This thesis presents the results of experimental and numerical studies on the effect of heat treatment on the mechanical properties and edge cracking behavior of high-strength 7075 aluminum alloy sheets. The experimental results of W-temper, super-saturated by solution heat treatment followed by water quenching, are compared to those of peak-aged 7075 (T6) temper by evaluating forming feasibility using various experiments. The experiments are numerically simulated based on the identified mechanical properties, and they are then comparatively analyzed with the 7075-T6 sheet.

In chapter 2, the mechanical properties of both tempers are scrutinized in various tests. The process parameters of -W temper are determined as 15 minutes solid solution heat treatment followed by water quenching, and the holding time between quenching and forming is less than 30 minutes. Both tempers show similar anisotropy including minor anisotropy in strength and higher anisotropy in plastic deformation. The reduction of elastic modulus is measured by a loading-unloading test, showing approximately 10% degradation. The investigated 7075-WT and T6 sheets showed considerable anisotropic hardening under loading path changes evaluated by a compression-tension test.

In chapter 3, based on a forming limit diagram obtained to verify formability, -W has a higher forming limit curve than T6, meaning enhanced formability. Prediction using the Marciniak-Kuczynski (M-K) model with the non-quadratic anisotropic yield function Yield2000-2d and the Swift hardening law shows considerable discrepancy from the measured FLDs. The larger exponent value in Yld2000-2d could better predict the formability of the 7075-T6 sheet. For the 7075-WT sheet, the overestimation of

ductility or the strain hardening exponent by the best fitted Swift hardening model might be attributed to the serrated flow behavior; therefore, the re-calibrated Swift hardening law that considered the measured uniform elongation (or strain hardening exponent) as an additional constraint for fitting provided better agreement with the experiment results of formability.

Also, a U-draw bending experiment is used for measuring springback, and W temper exhibits smaller springback than T6. The springback profiles are well predicted by the distortion-based HAH model and the chord modulus approach for both sheets. The predicted punch force-displacement curve is also well predicted in T6 temper; however, the predicted curve of -W displays underestimated punch force. The underestimated punch force for the 7075-WT sheet could be explained by the roughened surface quality by marks left by the Portevin-Le-Chatelier (PLC) effect, which virtually increases the friction coefficient.

In chapter 4, edge crack behavior or stretch-flangeability are investigated through hole-expansion (HE) experiments with conical and flat-headed punches. In the case of conical hole expansion, the hole expansion ratio results of two hole edge conditions, punching (shearing) and wire EDM, are compared. In T6 temper, the accumulated deformation through the hole fabrication process by shearing deteriorates the hole expansion ratio (HER) values more than the hole expansion ratio values using wire EDM for hole fabrication. However, the W temper displays almost similar hole expansion ratio values for the two hole fabrication methods because SHT alleviates the accumulated deformation made from the hole fabrication process. Overall, the W temper shows higher hole expansion ratio values than that of T6 in both edge conditions. The W temper has longer elongation and is more ductile than T6, even though the W

temper has shorter post uniform elongation from negative strain rate sensitivity.

For the flat-headed HE experiment, the strain evolution on the specimen surface is measured using the 3D-DIC technique, and a combined Swift-Voce hardening law with non-quadratic anisotropic yield function Yld2000-2d are implemented in the FE simulation. Hole expansion ratio values and overall thickness strain are greater in -W temper. Comparing the experiments to the FE predictions, the force displacement and average thickness strain evolution show good agreement for both tempers. The appearance of the PLC band in the hole expansion experiment is along the radial direction from the hole center and propagates along the circumferential direction. The life of an individual PLC band, from nucleation to dissipation, is traced by DIC analysis during hole expansion. Plastic anisotropy plays a major role in determining the thickness strain variation in -T6 temper. Even though both -T6 and -W tempers show similar anisotropy, the -W temper presents a different thickness strain variation from -T6 due to the PLC effect. The greater strain that develops in the RD due to plastic anisotropy can cause a larger number of PLC band nucleation sites near the RD, which indicates that the strain variation around the hole periphery is caused by plastic anisotropy and affects the nucleation of PLC bands.

In this thesis, the -W temper shows enhanced elongation, lower flow stress, larger forming limit diagram, smaller springback, and even greater stretch-flangeability than T6 temper. Therefore, the W process can potentially be used to manufacture high strength aluminum sheets at room temperature.

The following PLC effect influences on each experiment are investigated:

1) Overestimation of the strain hardening coefficient in hardening curve, 2) high roughness in the surface condition, 3) short post uniform elongation caused in the

ductile material, and 4) appearance of PLC bands in the hole expansion experiment showing interactions with plastic anisotropy.

Based on these results, more detailed research to include non-homogeneous strain properties associated with PLC effects can be developed experimentally or in the future with more advanced constitutive models.

Appendix

Appendix A. References of journal publications related to this thesis.

1. Yumi Choi, Jinwoo Lee, Sudhy S Panicker, Hong-kyo Jin, Myoung-Gyu Lee, Mechanical properties, springback, and formability of W-temper and peak aged 7075 aluminum alloy sheets : Experiments and modeling, **International Journal of Mechanical Science**, 2020, 170: 105344

2. Yumi Choi, Jinjin Ha, Myoung-Gyu Lee and Yannis P. Korkolis, Effect of plastic anisotropy and Portevin-Le Chatelier bands on hole-expansion in AA7075 sheets in -T6 and -W tempers, **Journal of Materials Processing Tech**, 2021, 117211

3. Yumi Choi, Jinjin Ha, Myoung-Gyu Lee and Yannis P. Korkolis, Observation of portevin-Le chatelier effect in aluminum alloy 7075-W under a heterogeneous stress field, **Scripta materilia**, 2021, 114178

4. Yumi Choi, Jin-woo Lee, Hyuk-jong Bong, Myoung-Gyu Lee, The effect heat treatment on edge cracking behavior of Aluminum 7075 (in preparation)

Appendix B. Comparison of material properties of AA7075-T6 sheets

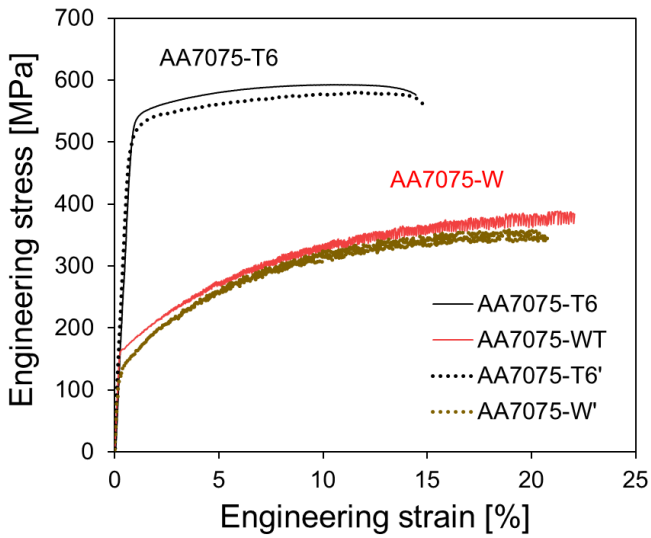

The comparison of engineering stress-strain curve of AA7075-T6 1.5t and AA7075-T6' 1.0t used in this thesis. The 7075-T6' is used for conical HE experiment.

Chemical compositios of the aluminum alloy T6' sheet (in wt.%)

Zn	Mg	Cu	Fe	Si	Mn	Ti	Cr	Al
5.7	2.8	1.5	0.18	0.07	0.03	0.08	0.18	Bal.

Mechanical properties for the 7075-T6' and 7075-W'

Materials	Orientation	Yield stress [MPa]	UTS [MPa]	UEL* [%]	TEL** [%]	R-value
7075-T6'	RD	513	580	12.7	14.7	0.57
7075-W'	RD	133	359	19.1	21.7	0.59

Reference

[1] A. Smeyers, B. Schepers, W. Braunschweig, A. Burger, K. Vieregge, S. Khosla, A. Wise, Alum. Int. Today 23 (2011) 37–39.

[2] T. Dursun, C. Soutis, Mater. Des. 56 (2014) 862–871.

[3] E.A. Starke, J.T. Staley, Prog. Aerosp. Sci. 32 (1996) 131–172.

[4] N. Lutsey, (2010) 24–42.

[5] J. Hirsch, Mater. Trans. 52 (2011) 818–824.

[6] H. Wang, Y.B. Luo, P. Friedman, M.H. Chen, L. Gao, Trans. Nonferrous Met. Soc. China (English Ed. 22 (2012) 1–7.

[7] M. Kumar, C. Poletti, H.P. Degischer, Mater. Sci. Eng. A 561 (2013) 362–370.

[8] H. Laurent, J. Coër, P.Y. Manach, M.C. Oliveira, L.F. Menezes, Int. J. Mech. Sci. 93 (2015) 59–72.

[9] K. Zheng, Y. Dong, D. Zheng, J. Lin, T.A. Dean, J. Mater. Process. Technol. 268 (2019) 87–96.

[10] N. Wang, A. Ilinich, M. Chen, G. Luckey, G. D'Amours, Int. J. Mech. Sci. 151 (2019) 444–460.

[11] L. Ying, T. Gao, M. Dai, P. Hu, Appl. Therm. Eng. 118 (2017) 266–282.

[12] M. Merklein, M. Lechner, A. Kuppert, Prod. Eng. 6 (2012) 541–549.

[13] J. Lin, T. Dean, R. Garrett, A. Foster, Pat. WO2008059242 A 2 (2008).

[14] Q. Liu, S. Chen, R. Gu, W. Wang, X. Wei, J. Mater. Eng. Perform. 27 (2018) 4423–4436.

[15] K. Zheng, D.J. Politis, L. Wang, J. Lin, Int. J. Light. Mater. Manuf. 1 (2018)

55–80.

[16] E. Romhanji, M. Popović, D. Glišić, M. Stefanović, M. Milovanović, Metalurgija 10 (2004) 205–216.

[17] O.N. Senkov, M.R. Shagiev, S. V. Senkova, D.B. Miracle, Acta Mater. 56 (2008) 3723–3738.

[18] M. Kumar, N.G. Ross, J. Mater. Process. Technol. 231 (2016) 189–198.

[19] United States Department of Defense, Aluminum and Aluminum Alloys, U.S. Department of Defense, 1966.

[20] R.A. Mueller, (1967).

[21] A.H. Cottrell, London, Edinburgh, Dublin Philos. Mag. J. Sci. 44 (1953) 829–832.

[22] H. Jiang, Q. Zhang, X. Chen, Z. Chen, Z. Jiang, X. Wu, J. Fan, Acta Mater. 55 (2007) 2219–2228.

[23] R.C. Picu, G. Vincze, F. Ozturk, J.J. Gracio, F. Barlat, A.M. Maniatty, Mater. Sci. Eng. A 390 (2005) 334–343.

[24] H. Ait-Amokhtar, C. Fressengeas, S. Boudrahem, Mater. Sci. Eng. A 488 (2008) 540–546.

[25] J.M. Robinson, M.P. Shaw, Mater. Sci. Eng. A 159 (1992) 159–165.

[26] R. Smerd, S. Winkler, C. Salisbury, M. Worswick, D. Lloyd, M. Finn, Int. J. Impact Eng. 32 (2005) 541–560.

[27] L.Z. Mansouri, J. Coër, S. Thuillier, H. Laurent, P.Y. Manach, Int. J. Mater. Form. (2019).

[28] J. Coër, P.Y. Manach, H. Laurent, M.C. Oliveira, L.F. Menezes, Mech. Res. Commun. 48 (2013) 1–7.

[29] P.Y. Manach, S. Thuillier, J.W. Yoon, J. Coër, H. Laurent, Int. J. Plast. 58 (2014) 66–83.

[30] S.C. Ren, T.F. Morgeneyer, M. Mazière, S. Forest, G. Rousselier, Int. J. Plast. 136 (2021).

[31] J. Mola, G. Luan, Q. Huang, C. Ullrich, O. Volkova, Y. Estrin, Acta Mater. 212 (2021) 116888.

[32] H. Louche, K. Bouabdallah, P. Vacher, T. Coudert, P. Balland, Exp. Mech. 48 (2008) 741–751.

[33] B.J. Brindley, P.J. Worthington, Acta Metall. 17 (1969) 1357–1361.

[34] A. Yilmaz, Sci. Technol. Adv. Mater. 12 (2011).

[35] A.H. Cottrell, B.A. Bilby, Proc. Phys. Soc. Sect. A 62 (1949) 49–62.

[36] Y. Estrin, L.P. Kubin, Mater. Sci. Eng. A 137 (1991) 125–134.

[37] K. Chihab, Y. Estrin, L.P. Kubin, J. Vergnol, Scr. Metall. 21 (1987) 203–208.

[38] L.P. Kubin, Y. Estrin, Rev. Phys. Appliquée 23 (1988) 573–583.

[39] S. Zhang, P.G. McCormick, Y. Estrin, Acta Mater. 49 (2001) 1087–1094.

[40] P.-Y. Manach, S. Thuillier, J.W. Yoon, J. Coër, H. Laurent, Int. J. Plast. 58 (2014) 66–83.

[41] H. Zhong, P.A. Rometsch, Q. Zhu, L. Cao, Y. Estrin, Mater. Sci. Eng. A 687 (2017) 323–331.

[42] B. Klusemann, G. Fischer, T. Böhlke, B. Svendsen, Int. J. Plast. 67 (2015) 192–216.

[43] E. Pink, W.M. Webernig, Acta Metall. 35 (1987) 127–132.

[44] T. Aoba, M. Kobayashi, H. Miura, Mater. Sci. Eng. A 700 (2017) 220–225.

[45] J.T. Staley, Met. Trans 5 (1974) 929–932.

[46] Y. Choi, C. Moon, M.G. Lee, IOP Conf. Ser. Mater. Sci. Eng. 651 (2019).

[47] D.I. Richard, P.N. Adler, Metall. Trans. A 8 (1977) 1177–1183.

[48] P. Zhou, Y. Song, L. Hua, J. Lu, J. Zhang, F. Wang, Mater. Sci. Eng. A 759 (2019) 498–505.

[49] J.Z. Liu, J.H. Chen, X.B. Yang, S. Ren, C.L. Wu, H.Y. Xu, J. Zou, Scr. Mater. 63 (2010) 1061–1064.

[50] L.K. Berg, J. Gjønnes, V. Hansen, X.Z. Li, M. Knutson-Wedel, G. Waterloo, D. Schryvers, L.R. Wallenberg, Acta Mater. 49 (2001) 3443–3451.

[51] H. Loffler, I. Kov/T, Cs, J. Lendvai, Review Decomposition Processes in AI-Zn-Mg Alloys, 1983.

[52] A.G. Leacock, C. Howe, D. Brown, O.G. Lademo, A. Deering, Mater. Des. 49 (2013) 160–167.

[53] A. Deschamps, F. Bley, F. Livet, D. Fabregue, L. David, (2010).

[54] G. Sha, A. Cerezo, Acta Mater. 52 (2004) 4503–4516.

[55] R. Arabi Jeshvaghani, H. Zohdi, H.R. Shahverdi, M. Bozorg, S.M.M. Hadavi, Mater. Charact. 73 (2012) 8–15.

[56] S.F. Fang, M.P. Wang, M. Song, Mater. Des. 30 (2009) 2460–2467.

[57] F. Savart, Ann. Chim. Phys, 65 (1837) 337–402.

[58] A.P. Masson, Ann. Chim. Phys. (Troisième Série) 3 (1841) 451–462.

[59] A. Le Chatelier, Rev. Métallurgie 6 (1909) 914–917.

[60] A. Portevin, F. Le Chatelier, Comptes Rendus Hebd. Des Séances l 'Académie Des Sci. 176 (1923) 507–510.

[61] A. Mogucheva, D. Yuzbekova, R. Kaibyshev, T. Lebedkina, M. Lebyodkin, Metall. Mater. Trans. A Phys. Metall. Mater. Sci. 47 (2016) 2093–2106.

[62] M. Lebyodkin, L. Dunin-Barkowskii, Y. Bréchet, Y. Estrin, L.P. Kubin, Acta Mater. 48 (2000) 2529–2541.

[63] A. Ziegenbein, P. Hähner, H. Neuhäuser, Mater. Sci. Eng. A 309–310 (2001) 336–339.

[64] G. Ananthakrishna, Phys. Rep. 440 (2007) 113–259.

[65] P.G. McCormick, Acta Metall. 21 (1973) 873–878.

[66] S.H. van den Brink, A. van Den Beukel, P.G. McCormick, Phys. Status Solidi 30 (1975) 469–477.

[67] P.G. McCormick, Acta Metall. 22 (1974) 489–493.

[68] L.P. Kubin, Y. Estrin, Acta Metall. Mater. 38 (1990) 697–708.

[69] R. Král, P. Lukáč, Mater. Sci. Eng. A 234–236 (1997) 786–789.

[70] J. Schlipf, Scr. Metall. Mater. 31 (1994) 909–914.

[71] R.C. Picu, D. Zhang, Acta Mater. 52 (2004) 161–171.

[72] T.J.B. Marc Legros, Gerhard Dehm, Eduard Arzt, Science (80-.). 319 (2008) 1646–1649.

[73] P. Hähner, Mater. Sci. Eng. A 207 (1996) 216–223.

[74] W.A. Curtin, D.L. Olmsted, L.G. Hector, Nat. Mater. 5 (2006) 875–880.

[75] R.A. Mulford, U.F. Kocks, Acta Metall. 27 (1979) 1125–1134.

[76] L.H. De Almeida, I. Le May, P.R.O. Emygdio, Mater. Charact. 41 (1998) 137–150.

[77] W. Lüders, Dingler's Polytech. J. (1860) 18–22.

[78] A. Ziegenbein, P. Hähner, H. Neuhäuser, Comput. Mater. Sci. 19 (2000) 27–34.

[79] F. Barlat, J.C. Brem, J.W. Yoon, K. Chung, R.E. Dick, D.J. Lege, F.

Pourboghrat, S.-H. Choi, E. Chu, Int. J. Plast. 19 (2003) 1297–1319.

[80] K. Hariharan, O. Majidi, C. Kim, M.G. Lee, F. Barlat, Mater. Des. 52 (2013) 284–288.

[81] S.L. Zang, C. Guo, S. Thuillier, M.G. Lee, Int. J. Mech. Sci. 53 (2011) 425–435.

[82] J.-W.W. Lee, M.-G.G. Lee, F. Barlat, Int. J. Plast. 29 (2012) 13–41.

[83] J. Lee, D. Kim, Y.-S.S. Lee, H.J. Bong, F. Barlat, M.-G.G. Lee, Comput. Methods Appl. Mech. Eng. 286 (2015) 63–86.

[84] Z. Marciniak, K. Kuczyński, Int. J. Mech. Sci. 9 (1967) 609–620.

[85] K. Bandyopadhyay, S. Basak, K.S. Prasad, M.-G. Lee, S.K. Panda, J. Lee, Int. J. Solids Struct. 156–157 (2019) 263–280.

[86] J. Lee, H.J. Bong, D. Kim, Y.-S. Lee, Y. Choi, M.-G. Lee, JOM (2019).

[87] P.A. Schuster, J.A. Ö sterreicher, G. Kirov, C. Sommitsch, O. Kessler, E. Mukeli, Metals (Basel). 9 (2019) 1–15.

[88] M. Kumar, G. Kirov, F. Grabner, E. Mukeli, Mater. Sci. Forum 879 (2017) 1036–1042.

[89] Y. Choi, J. Lee, S.S. Panicker, H.K. Jin, S.K. Panda, M.G. Lee, Int. J. Mech. Sci. 170 (2020).

[90] Y. Choi, J. Ha, M.-G. Lee, Y.P. Korkolis, J. Mater. Process. Technol. (2021) 117211.

[91] C. Yumi, H. Jinjin, L. Myoung-Gyu, K. Yannis P., Scr. Mater. 114178 (2021).

[92] L. Chen, S. Fang, K. Zhao, R. Xiao, H. Zhai, Int. J. Solids Struct. 202 (2020) 475–485.

[93] K. Omer, A. Abolhasani, S. Kim, T. Nikdejad, C. Butcher, M. Wells, S.

Esmaeili, M. Worswick, J. Mater. Process. Technol. 257 (2018) 170–179.

[94] D.A. Tanner, J.S. Robinson, J. Mater. Process. Technol. 153–154 (2004) 998–1004.

[95] W. Huo, L. Hou, Y. Zhang, J. Zhang, Mater. Sci. Eng. A 675 (2016) 44–54.

[96] J.Y. Lee, L. Xu, F. Barlat, R.H. Wagoner, M.G. Lee, Exp. Mech. 53 (2013) 1681–1692.

[97] R.K. Boger, R.H. Wagoner, F. Barlat, M.G. Lee, K. Chung, Int. J. Plast. 21 (2005) 2319–2343.

[98] F. Yoshida, T. Uemori, Int. J. Mech. Sci. 45 (2003) 1687–1702.

[99] V. Balakrishnan, Measurement of In-Plane Bauschinger Effect in Metal Sheets, The Ohio State University, 1999.

[100] J. Lee, J.-Y. Lee, F. Barlat, R.H. Wagoner, K. Chung, M.-G. Lee, Int. J. Plast. 45 (2013) 140–159.

[101] H. Kim, C. Kim, F. Barlat, E. Pavlina, M.G. Lee, Mater. Sci. Eng. A 562 (2013) 161–171.

[102] J. Mendiguren, E.S. De Argandona, L. Galdos, IOP Conf. Ser. Mater. Sci. Eng. 159 (2016).

[103] E. Ceretti, C. Contri, C. Giardini, J. Mater. Process. Technol. 177 (2006) 672–675.

[104] J. Lee, H.J. Bong, D. Kim, Y.-S. Lee, Y. Choi, M.-G. Lee, Met. Mater. Int. (2019).

[105] H.J. Bong, F. Barlat, D.C. Ahn, H.-Y. Kim, M.-G. Lee, Int. J. Mech. Sci. 75 (2013) 94–109.

[106] R. Shabadi, S. Suwas, S. Kumar, H.J. Roven, E.S. Dwarkadasa, Mater. Sci.

Eng. A 558 (2012) 439–445.

[107] J. Li, S.J. Hu, J.E. Carsley, T.M. Lee, L.G. Hector Jr., S. Mishra, (2011) 475–485.

[108] N.R. Harrison, S.G. Luckey, SAE Int. J. Mater. Manf. 7 (2014) 567–573.

[109] J. Choi, J. Lee, H.J. Bong, M.-G. Lee, F. Barlat, Int. J. Solids Struct. 151 (2018) 152–164.

[110] J.H. Kim, M.-G. Lee, F. Barlat, R.H. Wagoner, K. Chung, Int. J. Plast. 24 (2008) 2298–2334.

[111] F. Barlat, J.J. Gracio, M.G. Lee, E.F. Rauch, G. Vincze, Int. J. Plast. 27 (2011) 1309–1327.

[112] J. Lee, H.J. Bong, J. Ha, J. Choi, F. Barlat, M.-G. Lee, JOM 70 (2018) 1560–1566.

[113] J. Lee, S. Kim, Y. Lee, J. Lee, D. Kim, M. Lee, Int. J. Plast. 94 (2017) 74–97.

[114] S.S. Panicker, S.K. Panda, J. Mater. Eng. Perform. 28 (2019) 2967–2982.

[115] L.E. Murr, K.P. Staudhammer, S.S. Hecker, Metall. Trans. A 13 (1982) 627–635.

[116] N. Hedayati, R. Hashemi, J. Test. Eval. 48 (2020) 20180227.

[117] F. Mousavi, R. Hashemi, R. Madoliat, Int. J. Adv. Manuf. Technol. (2018).

[118] H. Halim, D.S. Wilkinson, M. Niewczas, Acta Mater. 55 (2007) 4151–4160.

[119] J. Kang, D.S. Wilkinson, M. Jain, J.D. Embury, A.J. Beaudoin, S. Kim, R. Mishira, A.K. Sachdev, Acta Mater. 54 (2006) 209–218.

[120] ABAQUS, User's Manual (2018), Hibbit,Karlsson & Sorensen Inc,.USA., 2018.

[121] J.-Y.J.Y. Lee, F. Barlat, M.-G.G. Lee, Int. J. Plast. 71 (2015) 113–135.

[122] Y. Zhou, H. Zhu, W. Zhang, X. Zuo, Y. Li, J. Yang, Adv. Mech. Eng. 7 (2015) 1–9.

[123] A.J.D. Westeneng, J.D. Westeneng, (2003).

[124] G.I. Taylor, Q. J. Mech. Appl. Math. 1 (1948) 103–124.

[125] S.K. Paul, Materialia 9 (2020) 100566.

[126] Y. Yamada, M. Koide, Int. J. Mech. Sci. 10 (1968) 1–14.

[127] N. Pathak, C. Butcher, M. Worswick, J. Mater. Eng. Perform. 25 (2016) 4919–4932.

[128] S. Sadagopan, D. Urban, C. Wong, M. Huang, B. Yan, 22 (2003) 171.

[129] P. Larour, J. Freudenthaler, A. Grünsteidl, K. Wang, (2014) 188–193.

[130] S.K. Paul, M. Mukherjee, S. Kundu, S. Chandra, Comput. Mater. Sci. 89 (2014) 189–197.

[131] S.K. Paul, J. Mater. Eng. Perform. 23 (2014) 3610–3619.

[132] D. Casellas, A. Lara, D. Frómeta, D. Gutiérrez, S. Molas, L. Pérez, J. Rehrl, C. Suppan, Metall. Mater. Trans. A Phys. Metall. Mater. Sci. 48 (2017) 86–94.

[133] J.I. Yoon, J. Jung, J.G. Kim, S.S. Sohn, S. Lee, H.S. Kim, J. Mater. Sci. 52 (2017) 7808–7823.

[134] S.K. Paul, Proc. Inst. Mech. Eng. Part B J. Eng. Manuf. 234 (2020) 671–676.

[135] A. Ishiwatari, M. Urabe, T. Inazumi, JFE Tech. Rep. 18 (2013) 96–102.

[136] M.J. Worswick, M.J. Finn, Int. J. Plast. 16 (2000) 701–720.

[137] T. Gläsner, M. Schneider, M. Troitzsch, S. Westhäuser, in: IOP Conf. Ser. Mater. Sci. Eng., 2016.

[138] X. Chen, H. Jiang, Z. Cui, C. Lian, C. Lu, in: Procedia Eng., Elsevier Ltd, 2014, pp. 718–723.

[139] N.M. Wang, M.L. Wenner, Int. J. Mech. Sci. 16 (1974).

[140] L. Chen, J.K. Kim, S.K. Kim, G.S. Kim, K.G. Chin, B.C. De Cooman, Steel Res. Int. 81 (2010) 552–568.

[141] J.H. Kim, E.J. Seo, M.H. Kwon, S. Kang, B.C. De Cooman, Mater. Sci. Eng. A 729 (2018) 276–284.

[142] P. Larour, J. Freudenthaler, M. Kerschbaum, D. Dolzer, IOP Conf. Ser. Mater. Sci. Eng. (2020).

[143] J.I. Yoon, J. Jung, H.H. Lee, G.S. Kim, H.S. Kim, Met. Mater. Int. 22 (2016) 1009–1014.

[144] J. Lee, S.J. Lee, B.C. De Cooman, Mater. Sci. Eng. A 536 (2012) 231–238.

[145] A. Karelova, C. Krempaszky, E. Werner, P. Tsipouridis, T. Hebesberger, A. Pichler, Steel Res. Int. 80 (2009) 71–77.

[146] Y.K. Ko, J.S. Lee, H. Huh, H.K. Kim, S.H. Park, J. Mater. Process. Technol. 187–188 (2007) 358–362.

[147] A. Konieczny, T. Henderson, SAE Tech. Pap. 116 (2007) 20–29.

[148] K. Wang, L. Greve, T. Wierzbicki, Int. J. Solids Struct. 71 (2015) 206–218.

[149] A. Kaijalainen, V. Kesti, R. Vierelä, M. Ylitolva, D. Porter, J. Kömi, in: J. Phys. Conf. Ser., Institute of Physics Publishing, 2017.

[150] K. ichiro Mori, Y. Abe, Y. Suzui, J. Mater. Process. Technol. 210 (2010) 653–659.

[151] O.R.. Terrazas, Corrlation of Microstructure, Tensile Properties and Hole Expansion Ratio in Cold Rolled Advanced High Strength Steels, Trustees of the Colorado School of Mines, 2016.

[152] M. Madrid, C.J. Van Tyne, S. Sadagopan, E.J. Pavlina, J. Hu, K.D. Clarke,

JOM 70 (2018) 918–923.

[153] V. Kumar Barnwal, S.-Y. Lee, S.-Y. Yoon, J.-H. Kim, F. Barlat, V.K. Barnwal, S. Lee, S. Yoon, J. Kim, F. Barlat, Int. J. Fract. 224 (2020) 217–233.

[154] J.W. Hutchinson, K.W. Neale, Acta Metall. 25 (1977) 839–846.

[155] A.K. Ghosh, Met. Trans 5 (1974) 1607–1616.

[156] T.K. Eller, L. Greve, M. Andres, M. Medricky, V.T. Meinders, A.H. Van Den Boogaard, J. Mater. Process. Technol. 228 (2016) 43–58.

[157] K. Ishikawa, J. Mater. Sci. Lett. 9 (1990) 400–402.

[158] V. Boljanovic, Sheet Metal Forming Processes and Die Design, Industrial Press Inc., 2004.

[159] I.S.O. 16630, (2009).

[160] J. Ha, S. Coppieters, Y.P. Korkolis, Int. J. Mech. Sci. (2020) 105706.

[161] J. Ha, Y.P. Korkolis, J. Manuf. Mater. Process. 5 (2021) 28.

[162] J. Kang, D.S. Wilkinson, J.D. Embury, M. Jain, A.J. Beaudoin, Scr. Mater. 53 (2005) 499–503.

[163] J. Mizera, K.J. Kurzydlowski, Scr. Mater. 45 (2001) 801–806.

[164] P.Y. Manach, J. Coër, H. Laurent, C. Bernard, S. Thuillier, in: Influ. Prestrain Occur. PLC Eff. an Al-Mg Alloy, American institute of physics, 2013, pp. 428–432.

[165] ISO 20482:2013. Metallic Materials—Sheet and Strip—Erichsen Cupping Test., 2013.

[166] A. Parmar, P.B. Mellor, Int. J. Mech. Sci. 20 (1978) 707–720.

[167] Y.P.Y.P. Korkolis, B. Brownell, S. Coppieters, H. Tian, J. Phys. Conf. Ser. 734 (2016).

[168] T. Cohen, R. Masri, D. Durban, Int. J. Solids Struct. 46 (2009) 3643–3650.

[169] T. Kuwabara, K. Hashimoto, E. Iizuka, J.W. Yoon, J. Mater. Process. Technol. 211 (2011) 475–481.

[170] H. Tian, B. Brownell, M. Baral, Y.P. Korkolis, Int. J. Mater. Form. 10 (2017) 329–343.

[171] Abaqus user manual, (2020).

[172] J.-Y.Y. Lee, K.-J.J. Lee, M.-G.G. Lee, T. Kuwabara, F. Barlat, Int. J. Solids Struct. 156–157 (2019) 107–118.

[173] T. Rahmaan, J. Noder, A. Abedini, P. Zhou, C. Butcher, M.J. Worswick, Int. J. Impact Eng. 135 (2020) 103390.

[174] A. Abedini, J. Noder, C.P. Kohar, C. Butcher, Mech. Mater. 148 (2020) 103419.

[175] Y.P. Korkolis, S. Kyriakides, Int. J. Mech. Sci. 53 (2011).

[176] T. Giagmouris, S. Kyriakides, Y.P. Korkolis, L.-H. Lee, Int. J. Solids Struct. 47 (2010).

[177] J. Ha, M. Baral, Y.P. Korkolis, Int. J. Solids Struct. 155 (2018) 123–139.

[178] H. Neuhäuser, F.B. Klose, F. Hagemann, J. Weidenmüller, H. Dierke, P. Hähner, J. Alloys Compd. 378 (2004) 13–18.

[179] B. Reyne, P.Y. Manach, N. Moës, Mater. Sci. Eng. A 746 (2019) 187–196.

[180] A. Benallal, T. Berstad, T. Børvik, O.S. Hopperstad, I. Koutiri, R. Nogueira De Codes, Int. J. Plast. 24 (2008) 1916–1945.

[181] B. Reyne, N. Moes, P.Y. Manach, Int. J. Plast. 131 (2020) 102713.

요약문 (Abstract in Korean)

차량 경량화가 대두됨에 따라, 경량 금속인 알루미늄 7천계를 차량 부품으로 활용하기 위하여 다양한 공정이 연구되고 있다. 본 연구에서는 강한 강도를 나타내는 T6 상태의 원소재를 용체화와 수냉 과정을 이용한 W 상태에 대해서 연구를 진행하였다.

W 상태는 T6 상태에 비해서 용체화에 이은 퀜칭 직후에는 낮은 강도와 긴 연신율을 가질 뿐 더러 퀜칭 이후 자연시효로 인해서 원 소재의 80% 이상까지 강도를 회복하는 장점이 있다. 현재 이런 W 상태에 관련하여 다양한 실험 결과나 소성 변형 거동, 특히 수치해석학적인 연구 결과가 아직 많지 않기 때문에 관련 연구가 필요하다. 본 학위 논문은 W 상태의 성형 가능성에 대해서 여러 실험 방법을 통해서 조사하였다. 이를 위하여 T6 와 W 상태의 소재를 대상으로 성형 한계 곡선을 이용한 성형성 연구, U자형 드로우/벤딩 실험을 통한 스프링백 연구, 원추형 및 납작형 펀치를 이용하여 홀확장성 실험을 통해 엣지 크랙 거동 연구 등의 주제에 대해 각각 진행하였다. 그 결과 전체적으로 W 상태의 소재가 T6 소재에 비해 더 넓은 성형 한계 곡선 영역, 더 적은 스프링백, 더 높은 홀 확장성 등을 나타내었다.

특히 W 템퍼의 경우에는 공칭 응력 곡선 내에서 Portevin-Le-Chatelier (PLC) 효과라고 불리는 톱니형 응력 곡선이 나타나기 때문에 이러한 측정 결과들은 PLC효과가 각 실험에 끼치는 영향성을 고려하여 분석하였다. T6를 이용한 실험 결과 및 유한요소해석 검증을 토대로, W 템퍼 결과에 대해서 동일하게 진행했으며 PLC효과를 제외한 물성을 반영한

유한요소해석 결과와 실제 실험 결과를 비교하는 과정을 통해 역으로 PLC 효과가 각 실험에 끼치는 영향성에 대해 분석하였다. 그 결과를 토대로 PLC 효과로 인한 특징을 기존 유한요소해석에 반영할 수 있는 방법 혹은 결과 분석시에 고려해야 하는 점 등에 대해 연구하였다. 그 결과 PLC 효과는 강화 곡선의 변수 과도한 값 설정, 표면 거칠기 향상, 더 연질한 성질을 가진 재료의 짧은 post-uniform elongation 특징, 소성 이방성과 상호작용하여 특정 파단 위치에 집중된 응력 등으로 나타났다.

핵심어 : 고강도 알루미늄 성형, 알루미늄 W 성형, PLC 효과, 성형성, 홀 확장성

학번 : 2018-37839

감사의 말

교수님이 부임하신 후 첫 수업에서 부터 2015년의 학부연구생을 시작으로 MAMEL의 초기 멤버였기 때문에 공유할 수 있었던 공별&미융팀 그리고 교수님과의 유대감을 함께 공유할 수 있게 된 것은 제게 20대의 가장 큰 행운이라 단언합니다. 제가 미국에 있을 때도 편지로 전했지만 정말 여러 방면에서 좋은 멘토라고 느낄 수 있는 분이 제 지도교수님이라는 점이 참 축복입니다.

첫 과제였던 POSCO springback, 첫 해외학회 APSTP, IDDRG 2018, 홈페이지, 넷이 갔던 제주도학회, MS오토텍 과제, IDDRG 2019, OSU visiting scholar, 마지막 학위 논문까지. 여러 이벤트와 함께 했던 짧다면 짧고, 제게 길다면 길었던 그 시간 동안 저의 대학원 생활을 직접적으로, 또 간접적으로 도와주신 많은 분들께 모두 깊이 감사드립니다. 사람들로 인해 힘든 게 가장 어렵다는데, 제가 정말 운이 좋다며 웃을 수 있는 것이 대학원 사람들이 너무 좋아서였습니다.

논문과 과제들 진행에 바쁜시간을 할애해서 많은 도움을 주셨던 이진우 박사님, 마지막 HER 관련 함께 해주신 봉혁종 박사님, 알루미늄 과제를 함께 진행하며 토의를 같이 해주신 KITECH 송정한 박사님과 배기현 박사님께도 감사드립니다.

연구실의 최전선으로 랩을 꾸리는데 고생했던 6년간의 랩장 우진오빠, 툴툴대면서도 연구에 관심 가져주고 도와주느라 이런 저런 고생을 많이 해서 항상 고마웠던 또 연구 자체를 좋아한다는 게 느껴지는 찬양오빠, 공학별관의 초창기멤버를 함께 했던 재민오빠와 함께 이백 양조장에서

이야기하던 때가 생각납니다. 미래융합관에서 크고 작은 일로 함께했던 유기홍부터, 역시 저를 도와주느라 고생했고 고마웠던 홍진오빠와 같이 시작하고 HE 초반에 도와주느라 고생했던 기정오빠, 제게 항상 용기를 주신 정연언니. 그 때 종종 조교도 도와주었던 정환오빠와 수현이, 가벽 안에서 같이 알루미늄 실험을 진행했던 석규님. 함께 IDDRG 2018때 FLD로 함께 고생했던 한국을 좋아하는 Kaushik Bandyopadhyay. 2 막의 시작 같은 서울대 시절부터 많이 친해진 센스쟁이 경문이와 준호오빠, 고온 실험으로 고생했던 찬미, 진흥이, 재승이 그 외에도 같이 어떤 걸 진행하진 않았지만 소소히 도와주었던 서준이와 정윤이. 다양한 종류의 실험을 하러 찾아갈 때 웃으며 반겨주었던 KITECH의 인제오빠와 선호오빠. 같이 숙대에서 추억을 쌓았던 서연언니와 혜진언니. 예약과 장비사용을 도와주셨던 예정원 연구원님, 미세조직 측정관련하여 함께 연구를 위해 의논해주셨던 한흥남 교수님의 정혜진, 박시욱, 조우진, 최호욱 연구원님, 측정 대상에 대해 함께 고민해서 진행해주셨던 김종범 연구원님까지 모든 분의 크고 작은 도움에 대해 감사의 마음을 다시 한 번 전합니다.

대학원 진학을 응원해주고 기간 내내 지지와 헌신으로 도와주신 가족분들께 항상 그 마음을 전하고 있지만 그 이상으로 마음 속 깊이 생각하고 있고, 모든 기간을 하나하나 공유했던 수형이와 이 과정 기간 동안에 저를 정서적으로 응원해주었던 친한 친구들에게도 고마움을 전하고 싶습니다.

I visited The Ohio State University at the US for 8 months during my Ph.D. study and I truly thank Prof. Yannis P. Korkolis for providing such a good experience. It was a pleasure for me to do a project with Prof. Yannis P. Korkolis and Prof. Jinjin Ha. I

thank Minki Kim and Clare for their help and friendliness, too.

I thank the active cooperation from all mentioned colleagues and I wish them all the best for the future.